Design and Manufacturing of a Demonstrator for the Flared Folding Wingtip Concept

J.P.Q. Hoyng

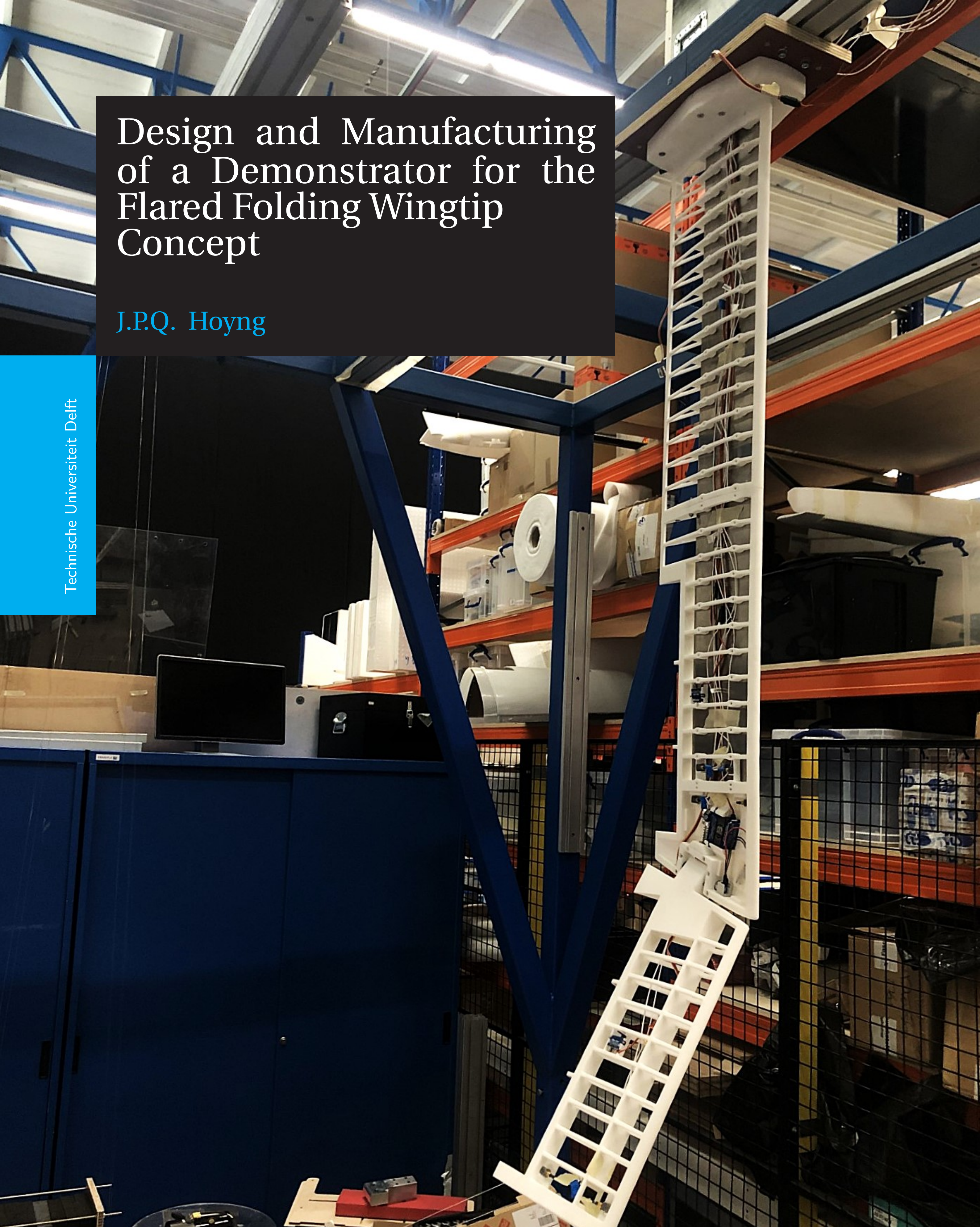

Technische Universiteit Delft

Delft University of Technology

Challenge the future

Design and Manufacturing of a Demonstrator for the Flared Folding Wingtip Concept

by

J.P.Q. Hoyng

in partial fulfillment of the requirements for the degree of

Master of Science
in Aerospace Engineering

at the Delft University of Technology,
to be defended publicly on Thursday February 27, 2025 at 13:00.

Supervisor:	Dr. J. Sodja	TU Delft
	Ir. X. Carrillo Córcoles	TU Delft
Thesis committee:	Dr. C. Varriale	TU Delft
	Dr. X. Wang	TU Delft

TU Delft Delft University of Technology

Preface

For as long as I can remember, I have been fascinated by everything that could fly. As a child, my parents gave me simple books about how airplanes worked and often took me to nearby airfields to watch planes take off and land. The moment I turned fourteen, I jumped into the cockpit of a glider. And from that point on, I knew I didn't want to do anything else. This was when I first encountered the many subjects I would need to master to earn my pilot's license. In a way, you could say my thesis journey truly began eleven years ago. Though officially, I was only allowed to spend seven months on it.
My passion for the theory behind flight led me to Delft to pursue a degree in aerospace engineering. And now, roughly 7.5 years later, here we are.

As I progressed in my studies, I realized I was most drawn to the practical side of what we learned. During my master's internship, I got my first real taste of designing something that would actually be built. The responsibility and creativity involved in that process were incredibly motivating.
My thesis has given me the opportunity to combine everything I love about aerospace engineering. I was able to apply theory to a field that truly excites me while also designing and manufacturing the project myself.

However, I could not have succeeded without the invaluable support of my supervisors. Throughout my thesis, Dr. J. Sodja gave me plenty of freedom while providing enough guidance to keep me on track.
Additionally, I want to express my gratitude to Xavi, who taught me a tremendous amount and was always available to help or discuss new ideas.

Besides the guidance from my supervisors, there are a few more people I would like to thank. First and foremost, I am grateful to my parents, Carel and Monique, for their unconditional support, both in my personal and academic life. I also want to thank my girlfriend Tessa for always reminding me that, as long as nobody dies, everything will be alright.
Finally, I cannot leave out my fellow thesis students, Casper and Guillaume, who deserve a special mention in this preface. From dart competitions on the 13th floor to endless debates about who brought the best lunch, there was always a way for our thesis to distract us from these important matters.

My academic journey in Delft has culminated in this report. I hope the reader enjoys it and that, perhaps, it may even inspire a lucky few.

J.P.Q. Hoyng
Delft, February 2025

Contents

List of Figures

List of Tables

Nomenclature

Abbreviations

AR Aspect Ratio
AVL Athena Vortex Lattice
BLI Boundary Layer Ingestion
BWB Blended Wing Body
CAD Computer Aided Design
CFD Computational Fluid Dynamics
DLM Doublet-Lattice Method
$EASA$ European Union Aviation Safety Agency
FEM Finite Element Method
$FFWT$ Flared Folding Wingtip
FRF Frequency Response Function
FSW Forward Swept Wing
GHG Greenhouse Gasses
GLA Gust Load Alleviation
GVT Ground Vibration Test
ITB Inter-stage Turbine Burners
LCO Limit Cycle Oscillation
MAC Modal Assurance Criterion
OJF Open Jet Facility
$PGAD$ Passive Gust Alleviation Device
PSD Power Spectral Density
$PTWT$ Passive Twist Wingtip
RBM Root Bending Moment

Greek Symbols

α_j^p Change in Local Angle of Attack at j^{th} Section
α_i Induced Angle of Attack
α_j Local Angle of Attack at j^{th} Section
$\alpha_{n=1}$ Anlge of Attack for $n = 1$
$\alpha_{n=2.5}$ Anlge of Attack for $n = 2.5$
α_{wt} Change in Local Angle of Attack of Wingtip
Δy Width of Strip
Δy_{cp} Change in Moment Arm due to Location of Center of Pressure
δ_{max} Maximum Aileron Deflection
$\dot{\omega}_{aileron}$ Aileron Angular Acceleration
η Angle of Rotation Eccentric Circle / Ellipse
Γ Circulation
Λ Flare angle
ν Kinematic Viscosity
$\omega_{aileron}^{req}$ Required Angular Velocity Aileron
ω_s Aileron Servo Actuator Required Rotational Speed
$\omega_{aileron}$ Aileron Angular Velocity
ρ Air Density
θ Rotation of Wingtip
ζ Hole Angle Hinge Mechanism

Latin Symbols

$\frac{L}{D}$ Lift-to-Drag Ratio
b Semi-span
b_{in}^{end} End of Spanwise Location of Inboard Aileron
b_{out}^{end} End of Spanwise Location of Outboard Aileron
b_{in}^{start} Start of Spanwise Location of Inboard Aileron
b_{out}^{start} Start of Spanwise Location of Outboard Aileron
b_1 Span of *Main section 1*
b_2 Span of *Main section 2*
b_{hinge} Spanwise Wingtip Hinge Location
b_{in} Span of Inboard Aileron
b_{out} Span of Outboard Aileron
b_{tip} Span of wingtip
C Chord Length
C Chord length
C_a Aileron chord length
C_l Local Lift Coefficient
C_m Aileron Hinge Moment Coefficient
c_x Horizontal Distance Point of Contact Eccentric Circle / Ellipse
c_y Vertical Distance Point of Eccentric Circle / Ellipse

$C_{L_{corr}}$ Corrected Lift Coefficient

$C_{l_{theory}}$ Theoretical Lift Coefficient

C_{ref} Reference Chord Length

d_x Horizontal Distance Point of Contact Locking Pin

d_y Vertical Distance Point of Contact Locking Pin

d_{cp} Distance Center of Pressure to Hinge line

f_1 First Bending Frequency

f_2 Second Bending Frequency

F_x Pin Horizontal Force

F_y Pin Vertical Force

$f_{2D/3D}$ 2D Lift Correction Factor

f_{3D} 3D Lift Distribution Scaling Factor

$F_{\delta_{down}}$ Distributed Lift Force Due to Downward Aileron Deflection

$F_{\delta_{up}}$ Distributed Lift Force Due to Upward Aileron Deflection

f_{FEM} Predicted Eigenfrequency by FEM

f_{GVT} Measured Eigenfrequency in GVT

F_{react} Reaction Force in Hinge Locking Mechanism

F_{roll} Distributed Lift Force Due to Roll

H Gust Gradient

I_a Aileron Moment of Inertia

L' Lift Per Unit Span

L_j Lift Force at Section

M_{servo}^{kgcm} Required Aileron Servo Actuator Torque [kgcm]

M_{servo}^{Nm} Required Aileron Servo Actuator Torque [Nm]

M_{Aero} Aerodynamic Moment Acting on Aileron

$M_{F_{\delta_{down}}}$ Rolling Moment Due to $F_{\delta_{down}}$

$M_{F_{\delta_{up}}}$ Rolling Moment Due to $F_{\delta_{up}}$

$M_{F_{roll}}$ Rolling Moment Due to F_{roll}

M_{roll} Rolling Moment

M_{servo} Servo Actuator Moment Acting on Aileron

M_{strip} Strip Moment Contribution Around Hinge line

p Roll Rate

r_1 Radius 1 Eccentric Circle / Ellipse

r_2 Radius 2 Eccentric Circle / Ellipse

r_a Aileron Connection Arm

r_s Servo Actuator Connection Arm

Re_{min} Minimum Reynolds Number

s Distance Penetrated into Gust

S_{ref} Reference Surface Area

t Time

T_s Aileron Servo Actuator Required Torque

U Gust Velocity

U_{ds} Design Gust Velocity

V Freestream Velocity

V_e Effective Velocity

V_{max} Maximum Testing Velocity

V_{min} Minimum Testing Velocity

W_f Final Weight

w_j Width of Section

x_{cp} Distance from Center of Pressure to Center Line

y_j Section Location

y_{strip} Spanwise Distance From Strip to Hinge

c Specific Fuel Consumption

R Range

W_i Initial Weight

1 Introduction

Earth is threatened by rising sea levels and extreme weather events, followed by disruption of ecosystems, desertification, limited water resources, and many more effects. All as a consequence of global warming. To prevent global warming from reaching an irreversible tipping point, the Paris agreement [1] formulated the goal of a maximum temperature rise of 2 ° Celsius above pre-industrial levels.

The major cause of global warming lies in the emission of greenhouse gasses (GHG) . Aviation contributed to 3.8% of the total CO_2 emissions in the EU in 2017 [2]. Reducing the emission of GHG by aviation would contribute to reaching the goal as described in the Paris agreement. After taking a look at Equation (1.1), The Bréguet Range Equation, it is clear that a reduction in required fuel weight (a reduced initial weight W_i) for a constant range (R) can be achieved by reducing the specific fuel consumption (c) , by improving the aircraft's aerodynamic performance ($\frac{L}{D}$) or by reducing the structural weight of the aircraft (W_f) .

$$R = \frac{1}{c} V \frac{L}{D} \ln \frac{W_i}{W_f} \tag{1.1}$$

Two examples of methods to improve traditional combustion systems and thus the specific fuel consumption are [3]: Increasing the engines bypass ratio and implementing Inter-stage Turbine Burners (ITB) . Although increasing the bypass ratio poses a trade-off for an increase in mechanical weight, modern turbofan engines have moved towards ultra-high bypass ratios. On the other hand, ITBs could improve the engine's efficiency by adding burners between turbine stages. Adding ITBs could decrease the specific fuel consumption by as much as 4% in cruise [4]. Assuming an equal payload weight, a structural weight reduction will decrease the energy required to move the aircraft, and thus fuel consumption. One way of improving the aerodynamic performance of the aircraft is reducing the lift induced drag of the wings. Since the induced drag is inversely proportional to the wings aspect ratio, an increase in the wings aspect ratio would lead to a drag reduction. However, increasing the wings aspect ratio is easier said then done; most airport do not have the gate capacity for aircraft with an increased wingspan and an increase in wingspan increases the moment arm of the load generated by the wing. It will also make the aircraft more susceptible to gusts and decreases the maneuverability of the aircraft. To withstand the increase in structural loads, the wing has to be strengthened and will become heavier, which can lead to an overall increase of fuel consumption. To solve the issue regarding the gate capacity, Boeing introduced the 777x with folding wingtips [5]. Section 1.1 will go into more detail about the effects of increasing the aspect ratio.

Recently, much research has been put into finding out if folding wingtips can be used to improve the maneuverability of the aircraft and can alleviate the gust and maneuver loads. Carrillo et al. [6] investigated the effect of the wing stiffness, aeroelastic tailoring and hinge release threshold of a folding wingtip on the gust load alleviation. A wind tunnel experiment showed that the peak root bending moment during gust decreased significantly. However, sustained oscillations of the wing occurred after the gust had passed. These oscillations can have many negative consequences, such as increased material fatigue and decreased passenger and crew comfort. Before diving into the state of the art of folding wingtips and what this thesis aims to contribute, Section 1.2 will briefly discuss the field of aeroelasticity, in which this topic can be categorized, after which Section 1.3 will explain the concept of load alleviation.

In Chapter 2, the state of the art numerical models, wind tunnel experiments and scaled flight test of the folding wingtips will be discussed. Exploring the state of the art leads to the objective of this thesis: to design and manufacture a demonstrator of a highly flexible wing featuring a flared, folding wingtip with ailerons on both the fixed and folding segments. This new design is an iteration of the design of Carrillo et al. [6] and could, hypothetically, reduce the sustained oscillations of the previous design. The outline of this thesis is presented in Section 2.3.

1.1. Drag reduction by an increase in aspect ratio

Abbas et al. [7] reviewed technologies that have the potential to improve the aerodynamic performance of aircraft. Three main categories in which these technological improvements are divided are: aircraft configuration technologies, drag reduction technologies and separation control technologies. The latter two focuses mainly on the delay of turbulent boundary layer and the control of flow separation, respectively. The aircraft configuration technology focuses mainly on changing the aircraft configuration significantly with respect to conventional aircraft. Four configuration technologies discussed are: Blended wing body (BWB) and Boundary layer ingestion (BLI) , High aspect ratio, Engine concept, and Forward swept wings (FSW) . A high aspect ratio wing is the technology on which this thesis builds. For a typical transport aircraft, as much as 40% [8] of the total drag of an aircraft consists of induced drag. Equation (1.2) shows that the induced drag coefficient is inversely proportional to the aspect ratio (AR) of the wing. This shows that an increase in wingspan, which increases the aspect ratio of a wing, would be beneficial for the reduction of induced drag.

$$C_{D_i} \propto \frac{1}{AR} \tag{1.2}$$

However, constantly increasing the aspect ratio of conventional aircraft will not infinitely increase the aircraft's efficiency. This is due to the increase in structural weight that is paired with an increase in aspect ratio. An increase in aspect ratio will increase the root bending moment (RBM) of the wing due to lift and will increase the RBM due to maneuvers and gust loads. To allow for the increase in RBM, a stronger and thus heavier wing must be designed. A second problem that comes to play with an increased aspect ratio, are the gate limitations of most airports. Code E airport spans are limited to 65 meter. To solve this second problem, the Boeing designed the 777X with folding wingtips, which have an extended wingspan of 71 meter, but a folded wingspan of 64 meter. By folding the wingtips during ground operation and extending it during flight, the airport gate limitations do no longer limit the aspect ratio of the wing, and an increased efficiency can be obtained. Current research is done to find out if the folding wingtip principle can be used to alleviate the loads and stay within the airport gate limitations while increasing the aspect ratio. Many different aspects of this new configuration, the flared folding wingtip (FFWT) , are investigated. Before discussing the different aspects of the FFWT, the field in which most of this research can be categorized must first be laid out: Aeroelasticity.

1.2. Aeroelasticity

Two problems involving the increased loads on the wing due to an increase in aspect ratio were mentioned above: the increase of maneuver and gust loads. This perfectly falls within the field of aeroelasticity, which studies the interaction between a structure and the airflow to which it is subjected. In Figure 1.1, Collar's triangle [9] shows aeroelasticity is a relation between the elastic, inertial and aerodynamic forces. Collar's triangle is extended to include control forces. This field is called: aeroservoelasticity. This field covers the interaction of a flexible structure, steady and unsteady aerodynamic forces, the structure motion and the control forces. Combining aeroservoelasticity with gust forces allows for an analysis of the problems mentioned above, regarding the increase of loads due to an increase of aspect ratio to improve performance. To reduce maneuver and gust loads, load alleviation can be applied. Next section will introduce the topic of load alleviation and how the FFWT can be used as a load alleviating tool.

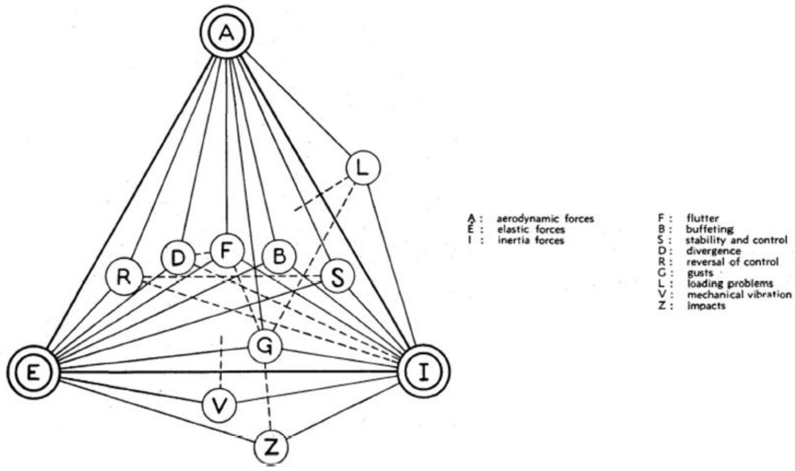

Figure 1.1: Collar's triangle , taken from and edited [9]

1.3. LOAD ALLEVIATION

The aim of load alleviation is to reduce the RBM and shear stress in a wing, which allows a lower structural wing mass. Load alleviation is applied to two different loading conditions: Gust loads and maneuver loads. Section 1.3.1 and Section 1.3.2 describe what gust and maneuver loads are, respectively. To alleviate gust and maneuver loads, two methods can be employed: passive and active load alleviation. Passive load alleviation does not require any active control, contrary to active load alleviation, which does require active control. Section 1.3.3 discusses several methods of passive load control, after which Section 1.3.4 goes into detail on active load control. Figure 1.2 is a schematic example of the effect of maneuver load alleviation on the lift distribution of a wing. Imagine that the dashed line is the lift distribution during an increase in load factor. By deflecting the outboard ailerons upwards, the lift on the outboard part of the wing is decreased. To achieve an equal load factor, the inboard lift must increase. Redistributing lift and moving the center of pressure inboard reduces the RBM while maintaining the total lift force.

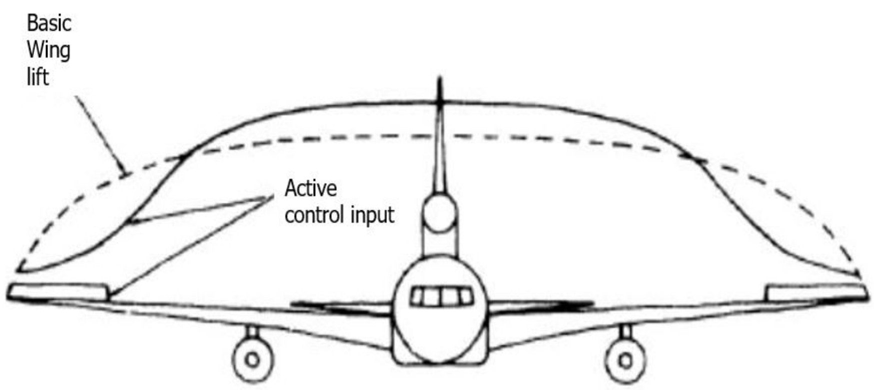

Figure 1.2: Illustration of lift distribution after maneuver load alleviation , taken from and edited [10]

1.3.1. GUSTS LOADS

An aircraft traveling through an unsteady airflow experiences a change of direction and velocity of incoming airflow and thus a change in lift distribution over the wing. This unsteady flow of air, from now on referred to as gust, is a complicated phenomena. Many different approaches exist to model gust loads, with varying directions and velocity profiles. Three directionalities exist: Vertical (a), Lateral (b) and Head-On (c) gusts [11], which are illustrated in Figure 1.3, where V is the forward flight speed, U is the gust velocity and V_e is the effective velocity.

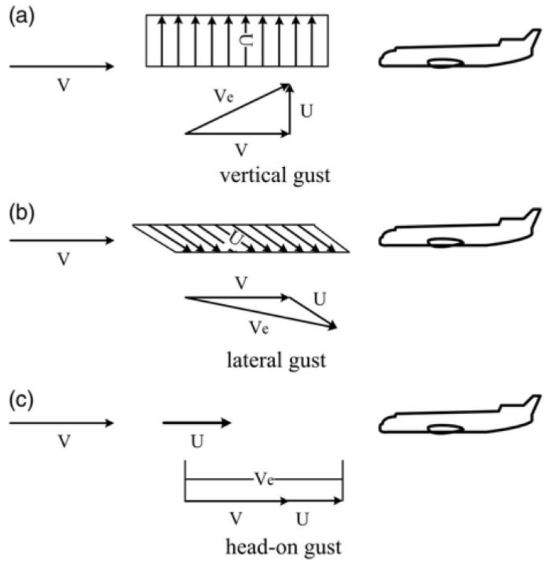

Figure 1.3: Gust directionalities, taken from [11]

In terms of velocity profiles, the European Union Aviation Safety Agency (EASA) CS-25 [12] regulations specify two different types of gusts for certification: The discrete gust and continuous gust. For discrete gusts, many different models exist. Three most commonly used gust models are: sharp-edge, linear-ramp and 1-cosine gusts [11]. CS-25 certification describe the 1-cosine shape for a discrete gust by:

$$U = \begin{cases} \frac{U_{ds}}{2}\left[1 - cos\left(\frac{\pi s}{H}\right)\right] & \text{for } 0 \leq s \leq 2H \\ 0 & \text{for } s > 2H \end{cases} \tag{1.3}$$

Where s is the distance penetrated into the gust, U_{ds} is the design gust velocity and H is the gust gradient, which is the distance parallel to the airplane's flight path for the gust to reach its peak velocity. This so-called 1-cosine gust is graphically illustrated in Figure 1.4. For the aforementioned continuous gust, EASA assumes a Gaussian distribution of gust velocity intensities and a Von Kármán power spectral density for the random atmospheric turbulence.

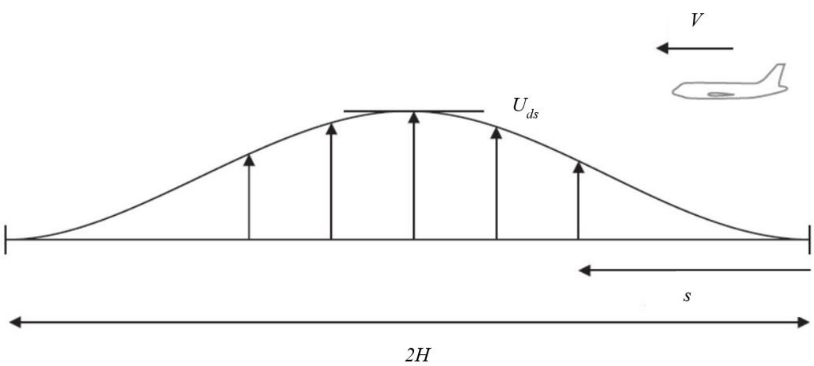

Figure 1.4: Schematic shape of 1-cosine gust, taken from and edited [13]

1.3.2. MANEUVER LOADS

Aircraft wings are structurally designed to withstand high maneuver loads, while their aerodynamic design aims to be optimal for cruise conditions. This aerodynamically optimal design will create large bending moment when the wing loading is increased for maneuvers. Ideally, the lift distribution would be increased mostly inboard of the wing, to reduce the bending moment and structural load [14], as previously illustrated in Figure 1.2. As further detailed in the CS-25 regulations, the maneuvering envelope (V-n diagram) shows what load factors must be designed for. The regulations state that the strength requirements must be met for all airspeed and load factor combinations on and within the boundaries of this diagram, Figure 1.5.

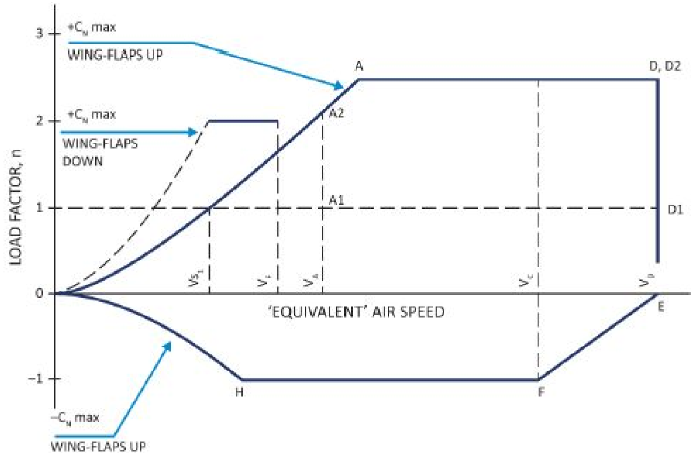

Figure 1.5: CS-25 Maneuvering Envelope, taken from [12]

1.3.3. PASSIVE LOAD ALLEVIATION

Passive load alleviation in aircraft design involves using structural and aerodynamic techniques to reduce the loads and stresses on the aircraft during flight without relying on active control systems. One key methods of passive load alleviation is the bending-torsion coupling. The bending-torsion coupling can be achieved by introducing rearward sweep in the wing planform design, by aeroelastic tailoring of the wing structural design, or by a combination of both. Rearward sweep introduces a bending-torsion coupling, often referred to as washout, which is a load alleviating mechanism that creates nose down twist for an upward bending wing [15]. By locating the shear center of the wing in front of the aerodynamic center, the wing will twist down while bending up. This effect can be enlarged by proper fibre orientation of composite layers in the wing's structure [16], which is called aeroelastic tailoring. A second example of passive load alleviation is the passive twist wingtip (PTWT) in a fixed wing aircraft [17] or a passive gust alleviation device (PGAD) on a blended wing body [18], as displayed in Figure 1.6a.

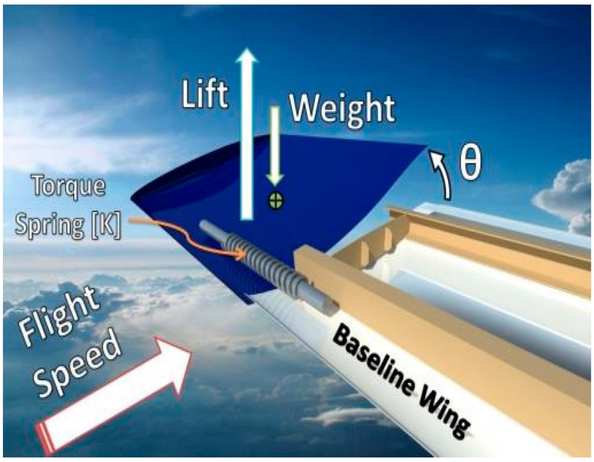

(a) Passive twist wingtip, taken from [17]

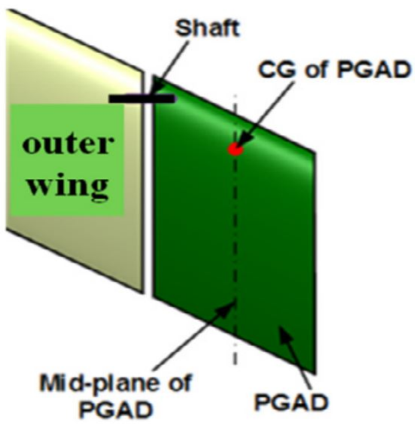

(b) Passive gust alleviation device, taken from [18]

Figure 1.6: Comparative images of passive twist wingtip and passive gust alleviation device

1.3.4. ACTIVE LOAD ALLEVIATION

Active load alleviation in aircraft design involves using active control techniques to reduce the loads and stresses on the aircraft during flight. Several methods exist to actively alleviate the loads of an aircraft. In the 1970s, the first methods of load alleviation were investigated by making use of flaps, spoilers and ailerons, and in the 1980s the Tristar L-1011 was the first commercial aircraft to successfully integrate gust load alleviation with its ailerons. A short list of existing load alleviation techniques is presented below [19]:

TRAILING-EDGE FLAPS

Trailing-Edge Flaps consider the control surfaces that are designed at the aft side of the wing, such as ailerons and elevators. A deflection of a Trailing-Edge flap changes the effective chamber of the airfoil and thus changes the lifting force.

SPOILERS

Spoilers serve multiple purposes, they are most often employed as speed brakes, but can also be used to alleviate gust loads. In the application of speed brakes, the spoiler movement can be quite slow. However, to alleviate gust loads, the spoiler movement must be much faster to counteract the high frequency unsteadiness. The modelling of spoilers for load alleviation poses some challenges, and much research effort is put in the understanding of the unsteady behaviour of spoilers. For example, Mabey et al. [20] demonstrated an initial lift increase after a spoiler deployment, called adverse lift. Experimental results of [21] confirmed the adverse lift during harmonic oscillations of the spoiler and showed that unsteady and nonlinear effects play an important role in the spoiler flow pattern.

FLUIDIC ACTUATORS

Besides flow control by control surfaces, aerodynamic flow control can also be applied for active load alleviation. By changing the boundary layer, fluidic actuator methods such as surface jet blowing and circulation control can be an effective measure to improve aerodynamic performance. A typical design of a surface jet is depicted in Figure 1.7

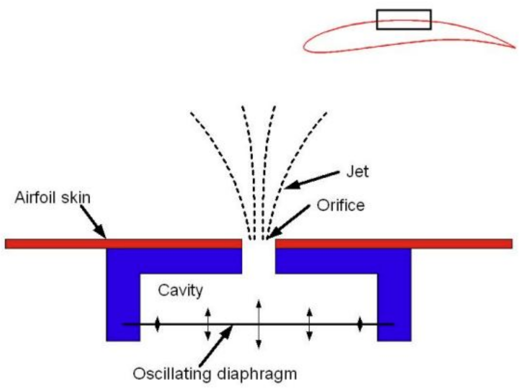

Figure 1.7: Schematic layout of a synthetic jet actuator, taken from [22]

FLARED FOLDING WINGTIP

The FFWT can be seen as a combination of active and passive load alleviation. The folding motion of the wingtip itself is passive, whilst the release is actively controlled. Since the FFWT is the focus of this thesis, Chapter 2 is dedicated to this method.

2

State of the Art

This chapter explores the state of the art regarding the Flared Folding Wingtip (FFWT). In Section 2.1, the FFWT concept is introduced alongside a review of existing research on the topic. By analyzing previous studies, a research gap is identified, leading to the formulation of the research objective and research questions in Section 2.2. Following this, the thesis outline is presented in Section 2.3.

2.1. The Flared Folding Wingtip (FFWT)

An increase in aspect ratio can play an important role in improving the aerodynamic performance of an aircraft. However, as mentioned in Section 1.1, increasing the aspect ratio, and thus the wingspan, leads to higher structural loads on the wing. To address this, the wing must be reinforced, which increases its structural weight and can eventually negate the efficiency gains from the increased aspect ratio. The structure of a large airplane must be able to withstand all load conditions described in CS-25 certification documents. A folding wingtip could be a solution to extending the wingspan for flight conditions whilst staying within the airport limitations on the ground. Extensive research is being conducted on how the FFWT can serve multiple functions, not only by extending the wing but also by acting as a gust load alleviation system.
Before diving into state of the art research on the FFWT, the concept will first be explained. In the work of Castrichini et al. [23], a preliminary investigation is made of the use of a FFWT for static and dynamic load alleviation. The concept implemented a hinged wingtip with a hinge line that has a relative angle Λ with respect to the incoming airflow. As illustrated in Figure 2.1, a positive relative angle causes the angle of attack of the wingtip to reduce when the wingtip is rotated upwards.

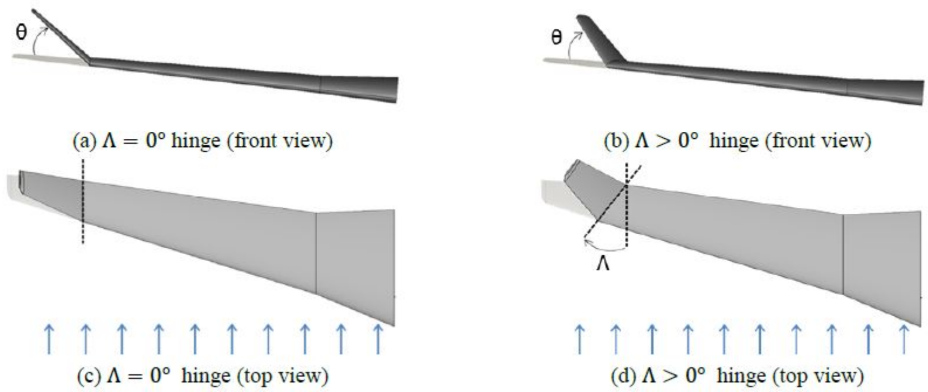

Figure 2.1: FFWT concept, taken from [23]

By assuming small angle deflections, Equation (2.1) gives the change in local angle of attack of the wingtip (α_{wt}) as a function of hinge orientation (Λ) and rotation of the wingtip (θ) :

$$\alpha_{wt} = -\tan^{-1}(\tan\theta \cdot \sin\Lambda) \tag{2.1}$$

Since a hinge that is aligned with the freestream could create an unstable folding motion of the wingtip, the principle described by Figure 2.1 and Equation (2.1) is used to increase the stability of the wingtip. By reducing the angle of attack for an increasing rotation angle, and vice versa, a positive value of Λ creates a self-stabilizing motion. Secondly, by having a freely rotating hinge, bending moments from the wingtip cannot be transferred to the main wing, which ultimately reduces the RBM of the wing. Combining the effects of a self-stabilizing wingtip with a reduction in RBM could offer an effective means to alleviate loads.
The FFWT has been studied extensively with both numerical and physical models. In the preliminary investigation [23], a wingtip was connected to the main wing of an aeroelastic model of a typical commercial jet, extending its wingspan by 25%. A stick model with lumped masses was used for the structural model, and a Doublet Lattice panel method [24] was used for the aerodynamic model. A visualisation of both models is presented in Figure 2.2.

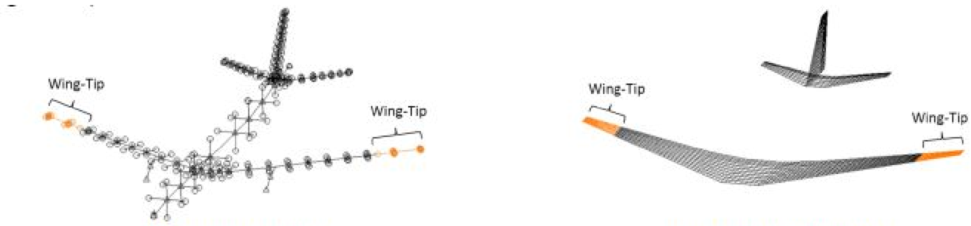

(a) Structural model (b) Aerodynamic model

Figure 2.2: Structural and Aerodynamic model, taken from [23]

These analysis showed that increasing the hinge angle and lowering the wingtip mass both increase the load alleviation. A significant reduction in flutter speed was observed for this configuration. By having a hinge angle, reduced wingtip weight and a low hinge spring stiffness, significant load alleviation was achieved for gust responses.
Castrichini et al. [25] built upon this work by implementing a passive nonlinear hinge spring that activates the folding wing only beyond a specific load threshold. It showed that the loading threshold strongly affects the load alleviation abilities of the folding wing. It is described that a limit in the FFWT approach is that, once the hinge is released and the gust has passed, the wingtip would remain deflected. By examining the effect of a high-static, low-dynamic aeroelastic stiffness mechanism, Castrichini et al. [26] propose a solution to this problem. This design would keep the wing in planar position during cruise, but would allow for rapid deflection in case of a vertical gust. Secondly, the springs negative stiffness facilitated larger and quicker wingtip movements, reducing the effects of gusts. Furthermore, the passive hinge design ensured that the folding mechanism could move back to its initial undeflected state after the gust had passed.
An additional challenge of increasing the wingspan is the associated increase in roll damping, which degrades the aircraft's handling qualities. Dussart et al. [27] investigated the effect of wingtip folding on the roll characteristics of flexible aircraft within a large range of flight conditions within the flight envelope of a civil aircraft. As expected, the roll rate decreased after extending the wing with the FFWT and keeping the hinge fixed. However, the numerical model suggested that releasing the FFWT can help in reducing the loss of roll performance of an aircraft.

Simulating the behaviour of the FFWT in a numerical model can be hard due to the complex and nonlinear behaviour. Therefore, researches have created wind tunnel models to further investigate and validate the FFWT behaviour. Cheun et al. [28] created the first wind tunnel model of the FFWT, seen on Figure 2.3a. With this physical model, the effect of the hinge angle on the load alleviation capabilities of the FFWT was investigated. Gust alleviation tests showed that the FFWT could provide significant load alleviation, and a maximum load reduction of 56% was reached in a free hinge condition. The experiment showed that the aeroelastic analysis with the NASTRAN finite element model and the Doublet-Lattice method (DLM) underpredicted the load alleviation capabilities of the FFWT, which shows that this method is incompatible with large deflections and rotations of lifting surfaces.

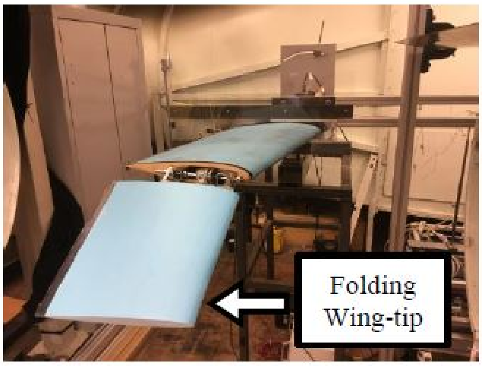

(a) FFWT wind tunnel model (2018), taken from [28]

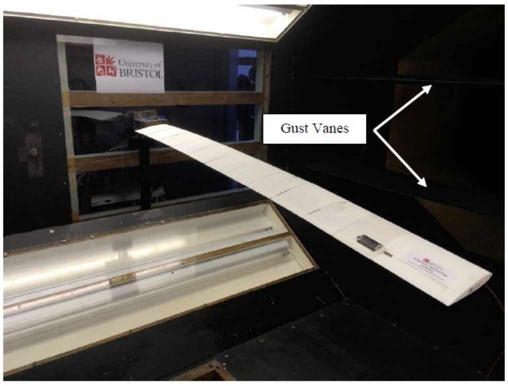

(b) FFWT wind tunnel model (2020), taken from [29]

Figure 2.3: Wind tunnel models from Cheung et al.

Cheung at al. [29] investigate the effect of the FFWT on the gust load alleviation of a flexible high aspect ratio wing. In addition, a trailing edge control surface was fitted to the wingtip to actively control the orientation of the wingtip and to further increase the load alleviating capabilities of the FFWT. The wind tunnel model is displayed in Figure 2.3b, in which the high aspect ratio is clearly visible. The experiment again showed the load alleviating capabilities of the FFWT. When properly timed, the actuation of the control surface can further reduce the gust loads on the wing, which show potential for gust load alleviation applications in future FFWT designs.

As mentioned earlier, increasing the wingspan typically leads to a decrease in roll performance. However, Healy et al. [30] investigated the effect of the FFWT on roll performance both numerically and experimentally in a wind tunnel. Figure 2.4 illustrates the experimental setup. To generate the rolling moment, a trailing edge control surface is positioned along the entire length of the fixed part of the model. By releasing the hinge during roll maneuvers, the experiment has proven that the FFWT can significantly improve the roll performance compared to a equal length fixed wing. By releasing the wingtip, the aerodynamic roll damping is decreased and the roll rate is increased. Both roll rate and angular acceleration has improved by the released wingtip. Further exploration with the numerical model has shown that, by introducing the FFWT, the wingspan of the original wing can be extended whilst having similar or even improved roll performance.

However, Sanghi et al. [31] numerically studied roll maneuvers of a highly flexible, high-aspect-ratio wing transport aircraft with free folding wingtips, incorporating ailerons both inboard and outboard of the hinge. The results show that the FFWT had no significant effect on the aircraft's roll performance, and in some cases, it even resulted in slower roll rates.

The conflicting conclusions between the work of Healy et al. and Sanghi et al. highlight the need for further research to better understand the effects of FFWT in combination with a flexible wing and control surfaces.

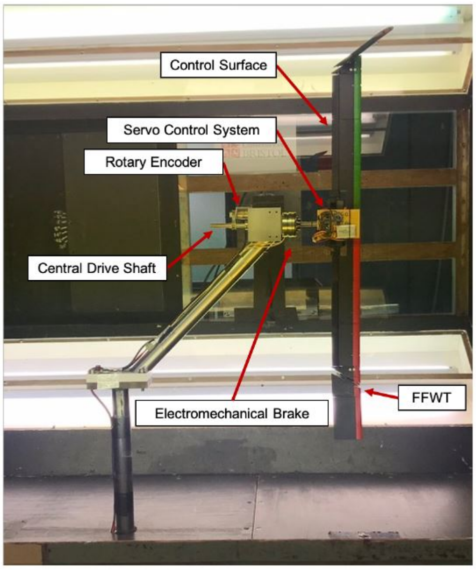

Figure 2.4: Wind tunnel model for roll performance, taken from [30]

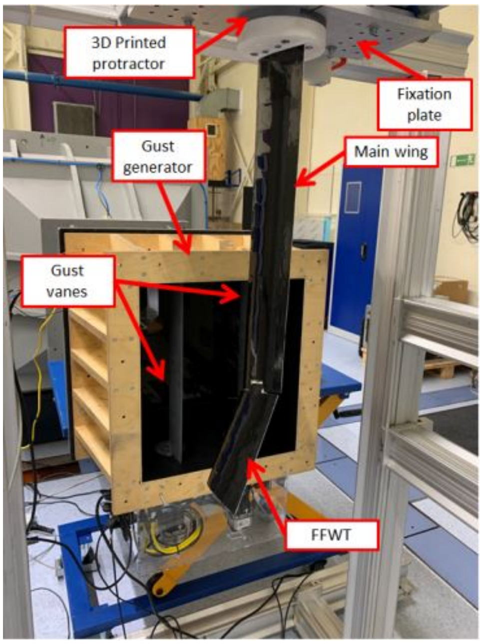

Figure 2.5: Wind tunnel test setup, taken from [6]

Carrillo et al. [6] studied the effects of wing stiffness, aeroelastic tailoring, and the release threshold of the hinge on the gust alleviation performance by means of a wind tunnel experiment, as can be seen in figure Figure 2.5. No clear correlation was found between structural stiffness and gust load alleviation. The timing of the hinge release proved to be crucial, with early release being effective, while release near the peak gust load could worsen wing loading. However, the wind tunnel experiment revealed discrepancies between the numerical model and the observed wing behavior, indicating that the model did not accurately capture the wing's response. To address this, two improvements have been performed in future work: first, Carrillo et al. [32] performed a Ground Vibration Test (GVT) to better correlate the numerical model with the physical wing; second, Carrillo et al. [33] presented a low-fidelity numerical model to better account for the nonlinearities due to large deflections.

Results showed that, although the FFWT reduced peak loading, the wing oscillates for a longer period after the gust has passed. These sustained oscillations could have a negative effect on for example material fatigue and passenger comfort.

Besides numerically modeling the effect of the FFWT and conducting wind tunnel experiments, efforts have been made to conduct scaled flight tests. The AlbatrossONE [34] is a scaled demonstrator used to take the next step in investigating the effects of the FFWT. The demonstrator can be seen in Figure 2.6. The flight tests confirmed the load alleviation effect of the FFWT by comparing stain gauge measurements from two flight tests.

Figure 2.6: The AlbatrossONE scaled flight test demonstrator, taken from [34]

In 2025, the eXtra Performance Wing project [35] aims to start flight testing their new wing design. In this project, a Cessna Citation VII business jet is equipped with new wings that can provide multiple configurations and test innovative designs. The aircraft will be provided with gust sensors in the front of the aircraft and will be equipped with folding wingtips. The final goal of the eXtra Performance Wing is to reach a wingspan of approximately 50 meters, so the Citation serves as a roughly 1:3 scaled demonstrator with its 16 meter span. Since this is a demonstrator project and the aircraft will not be put into production, the aircraft will be remotely operated, which will eliminate the certification efforts for human flight.

2.2. RESEARCH QUESTIONS

In Section 2.1, the FFWT is presented along with the state of the art research on the topic, which has a primary focus on the effect that the FFWT has on load alleviation and the maneuverability of aircraft. Cheung et al. [29] demonstrated that proper scheduling of a trailing edge control surface in the wingtip can further improve the load alleviation of the FFWT. Secondly, contradicting conclusions on the effect of the FFWT on the roll performance between the work of Healy et al. [30] and Sanghi et al. [31] demonstrates the need for more understanding of the effect of control surfaces in combination with a highly flexible wing with the FFWT. Additionally, work of Carrillo et all. [6] showed sustained oscillations after the release of the FFWT hinge, which could potentially be damped with trailing edge control surfaces.

A clear research gap presents an opportunity to develop a highly flexible wind tunnel demonstrator with ailerons on both the fixed wing and the FFWT for experimental studies, leading to the research objective of this thesis:

> *The objective of this thesis is to design and manufacture a demonstrator of a highly flexible wing featuring a flared, folding wingtip with ailerons on both the fixed and folding segment, capable of demonstrating its aeroelastic behavior in gust response and to conduct a ground vibration test to validate the structural model of the wing.*

From this research objective, the following research questions have been derived:

Research Question 1: What structural and aerodynamic model are required to design the demonstrator of a wing featuring a flared, folding wingtip with ailerons?

- (a) What structural effect must be captured for the sizing of the demonstrator components?
- (b) What aerodynamic effects must be captured for the sizing of the demonstrator components?
- (c) What modeling tool can be used to capture the aeroelastic behavior of the demonstrator?

Research Question 2: What demonstrator design is required to investigate the aeroelastic behavior in gust response of a highly flexible wing featuring a flared, folding wingtip with ailerons?

- (a) What demonstrator design is required to properly represent the results from the component sizing?
- (b) What hinge design is required to showcase the locked and free hinge conditions within all operating conditions?

2.3. THESIS OUTLINE

The methodology for the flared folding wingtip demonstrator is structured into four distinct work packages, each addressing a critical phase of the project: Preliminary Design (Chapter 3), Sizing (Chapter 4), Detailed Design (Chapter 5), and Testing (Chapter 6). While these work packages follow a general chronological order, they are inherently interdependent. Iterations between the packages are essential to refine the design and ensure a successful transition from the preliminary design phase to the final assembly and testing stage. Chapter 7 provides the final conclusion of this thesis, followed by recommendations and suggestions for future work.

Figure 2.7 illustrates the dependencies and interactions between these work packages, highlighting the iterative nature of the first three packages. The title of each work package corresponds to a chapter in this thesis. Throughout this chapter, readers can refer back to this figure to better understand their position within the overall process.

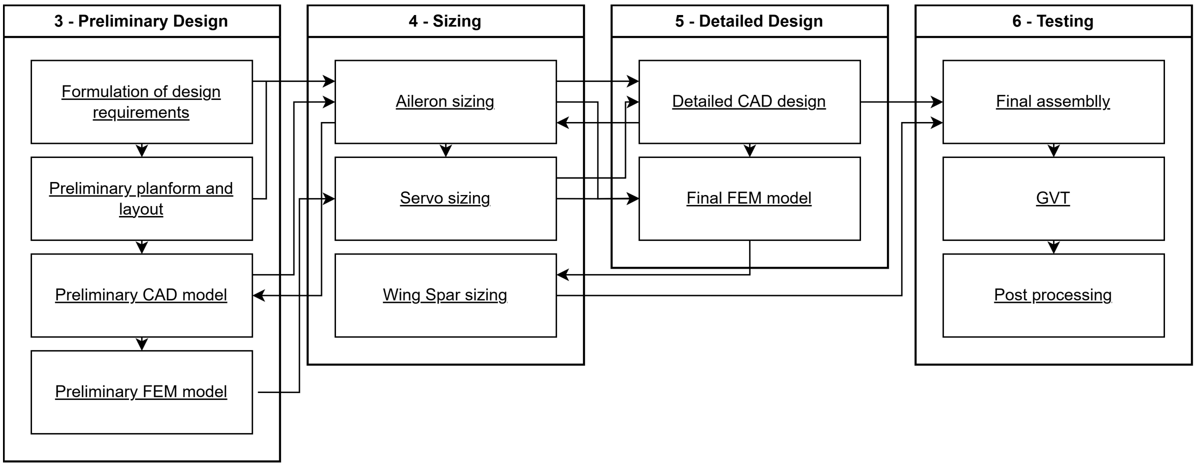

Figure 2.7: Graphical workflow representation

3

Preliminary Design

The aim of the preliminary design phase is to develop an initial estimate of the demonstrator's design specifications. This phase is not only essential for progressing to the sizing and detailed design stages but also facilitates quick iterations of design changes.

The preliminary design phase consists of three main tasks. First, the design requirements and testing conditions are specified in Section 3.1. The requirements address both performance objectives and practical limitations, such as the outer dimensions of the wind tunnel section, while the testing conditions lay out the basis for designing and sizing all components.
Secondly, a preliminary planform layout is developed and presented in Section 3.2. This layout establishes the initial wing sizing and provides a rough placement of movable components: an inboard aileron, an outboard aileron and the hinge. The initial planform serves as the foundation for the aerodynamic analysis used in aileron sizing. Once the planform is defined, a basic Computer Aided Design (CAD) model of the wing is created. This 3D representation allows for a thorough inspection of the design, enabling the detection of potential infeasibilities early in the design phase.
Finally, the CAD model is used to create an initial Finite Element Method (FEM) model of the demonstrator. With this FEM model, the structural modes of the wing are estimated, which are then used to select the appropriate aileron actuation servos based on their required angular speed. In Chapter 4, the preliminary FEM and the servo actuator sizing will be discussed in more detail.

3.1. Design Requirements and Testing Conditions

This section presents the design requirements and testing conditions for the demonstrator. The design requirements are categorized into performance requirements and design constraints, defining both the objectives and limitations of the design. Additionally, the testing conditions necessary for evaluating the demonstrator's performance are outlined, which will serve as the foundation for further analysis and design decisions.

3.1.1. Design Requirements

A distinction is made between performance requirements and design constraints. Whilst the performance requirements set an objective for the demonstrator design, the design constraints are limiting the design freedom. At the end of this section, the performance requirements (*Req*) and design constraints (*Con*) are summarized in Table 3.1 and Table 3.2, respectively.

From Research Questions 2.a and 2.b, the dominant design requirements can be derived. Research Question 2.a "*What aileron sizing is required to provide enough control effectiveness to the wing and wingtip?*" establishes a requirement for the control effectiveness of both ailerons. The goal of the inboard aileron is to replicate the realistic roll performance of an actual transport aircraft.
Based on the work of Pusch et al. [36], the required roll rate is set to 15 degrees per second. This roll rate is based on the CS-25 certification requirement that an aircraft must be able to demonstrate a roll maneuver from a steady 30 degrees bank angle to a 30 degrees opposite bank angle, within 7 seconds. This certification

requirement is transformed to the steady state roll rate requirement *Req-1* at a maximum aileron deflection of 20 degrees up or down.
For the outboard aileron, the goal is to return the wingtip back to neutral position, such that the hinge can be locked without external inputs. To achieve this, the outboard aileron must be able to create a zero or negative (wingtip down) moment around the hinge line at all flight conditions. This leads to the performance requirement *Req-2*.

Research Question 2.b "*What aeroelastic phenomena should the demonstrator be able to showcase within the wind tunnel velocity range?*" creates an additional set of performance requirements. At first, it is desired that the demonstrator design will experience flutter just below the maximum operating speed of the wind tunnel. The demonstrator is designed to be operated in the Open Jet Facility (OJF)[1]) of the TU Delft. The OJF currently has a maximum operating speed of 25 m/s. From previous work, it clear that the flutter speed of the unlocked hinge condition is lower than that of the locked hinge condition. The operating speed of the OJF and the flutter mechanism of the demonstrator can be combined in requirement *Req-3*. Additionally, since the design is intended to behave like a highly flexible wing, a performance requirement is established for tip deflection under the maximum wind tunnel operating speed and angle of attack. Under these conditions, the demonstrator is required to achieve an upward tip deflection of 15–20%, similar to that of the TU Delft Pazy wing [37], as specified in requirement *Req-4*. Having a large tip deflection would allow the demonstrator to properly showcase non-linear behavior, such as a Limit Cycle Oscillation (LCO).
Requirement *Req-5* addresses the third aeroelastic phenomenon, specifying that the wing must not experience divergence within the testing envelope, as this could result in the destruction of the demonstrator.
In future work, the ailerons will be utilized for active Gust Load Alleviation (GLA). To ensure the ailerons are appropriately designed, a requirement is placed on the maximum angular velocity of the aileron servo actuators. The bandwidth of the servo actuator must cover a frequency range up to the frequency of the second bending mode of the wing. This results in requirements *Req-6*. Requirement *Req-7* specifies that the demonstrator must be operable in both locked hinge and free hinge configurations across all testing conditions, which requires proper hinge design and sizing. Lastly, for the sizing of the aileron servo actuators, requirement *Req-8* states that the aileron servo actuators must be able to lock the aileron at both positive and negative maximum deflection.

[1]See "Open Jet Facility," TU Delft, `https://www.tudelft.nl/lr/organisatie/afdelingen/flow-physics-and-technology/facilities/low-speed-wind-tunnels/open-jet-facility`.

Table 3.1: Performance requirements Overview

ID	Requirement Description
Req-1	The inboard aileron shall enable the demonstrator design to achieve a steady-state roll rate of at least 15 degrees per second with a maximum aileron deflection of 20 degrees up or down, even under the least optimal flight conditions.
Req-2	The outboard aileron shall provide zero or negative moment (wingtip down) to the wingtip with a maximum deflection of 20 degrees up or down, even under the least optimal flight conditions.
Req-3	The flutter speed of the wing, in the unlocked hinge condition, shall be close to, but not exceed, 25 m/s.
Req-4	The demonstrator shall have an upward wingtip deflection of 15-20% of the semi-span at an angle of attack of 5 degrees and an airspeed of 25 m/s.
Req-5	The demonstrator shall not experience divergence under any circumstances in the wind tunnel.
Req-6	The bandwidth of the aileron actuation servo actuator must cover a frequency range up to the frequency of the second bending mode of the demonstrator.
Req-7	The demonstrator shall operate in both locked hinge and free hinge configurations under all testing conditions.
Req-8	The aileron servo actuator shall have enough torque to lock the aileron at its maximum deflected position.

The design constraints stem from the testing environment and production method. The open test section of the OJF at TU Delft measures 285 x 285 cm. To minimize boundary effects, the demonstrator is designed to fit well within the test section. To provide plenty of margin between the wingtip and the boundary of the test section, *Con-1* states that the minimum distance from the wingtip to the boundary is 100 cm. Secondly, the SLS manufacturing technique at the selected company does not allow for sections larger than 665 x 356 x 545 mm. Since it is desired to have a largely continuous structure, the main wing cannot exist of more then 2 sections, and the wingtip must be made out of one section. Combining this results in constraint *Con-2*.

Table 3.2: Design constraints Overview

ID	Requirement Description
Con-1	The demonstrator shall fit within the 285 × 285 cm OJF wind tunnel test section, maintaining a minimum clearance of 100 cm between the wingtip and the test section boundary to minimize boundary effects.
Con-2	The main wing shall consist of no more than two sections, with the wingtip constructed as a single section. All sections shall fit within the manufacturing limit volume of 665 x 356 x 545 mm.

3.1.2. TESTING CONDITIONS

During the preliminary design phase, the main testing conditions are defined, corresponding to the expected wind tunnel testing environment. These conditions will serve as the basis for designing and sizing all components. The demonstrator is designed for the OJF wind tunnel, which currently has a maximum operating speed of 25 m/s. This corresponds to the upper velocity for which the demonstrator will be designed. In order to evaluate the performance at a lower velocity too, a velocity of 15 m/s is set at the lower limit. During the analysis, the standard atmosphere at sea level is assumed, which results in an air density (ρ) of 1.225 kg/cm^3. The lower angle of attack for the analysis is set to 2°. With a load factor of $n = 1$ this will be used as a baseline angle of attack ($\alpha_{n=1}$) in the analysis. To mimic a load factor of $n = 2.5$, a second angle of attack ($\alpha_{n=2.5}$) is set at 5°, which will also be used to during in the simulations. To analyze the Reynolds number, a kinematic viscosity of $1.46 \cdot 10^{-5}$ m^2/s is used. In order to have predictable flow effects, the Reynolds number should not be below 200.000. Lastly, the sizing is performed using a maximum aileron deflection of ±20°.

Table 3.3: Test Parameters and Descriptions

Parameter	**Description**	**Value**
V_{min}	Minimum Testing Velocity	15 m/s
V_{max}	Maximum Testing Velocity	25 m/s
ρ	Air Density	1.225 kg/m^3
$\alpha_{n=1}$	Angle of Attack for $n = 1$	2°
$\alpha_{n=2.5}$	Angle of Attack for $n = 2.5$	5°
ν	Kinematic Viscosity	$1.46 \cdot 10^{-5}$ m^2/s
Re_{min}	Minimum Reynolds Number	200,000
δ_{max}	Maximum Aileron Deflection	±20°

3.2. WING PLANFORM

The preliminary wing planform design consists of two parts: First, a simple 2D planform is created as a baseline for the aerodynamic modeling of the wing. Second, a preliminary CAD model is developed to conduct initial design and feasibility assessments.

3.2.1. 2D PRELIMINARY DESIGN

In the preliminary design phase, a simplified 2D planform is created to aid the sizing of the outer dimensions. Figure 3.1 illustrates the high-level dimensions of the planform.
Inspired by the work of Carrillo et al. [6], this planform is a scaled version of the original, with most characteristics remaining constant. With a semi-span of 1540 mm and an aspect ratio of 14 (mimicking a high aspect ratio wing), a chord length of 220 mm is obtained. By adhering to requirement *Con-2* and being advised by the manufacturer to keep the maximum dimension of the parts within 580 mm to ensure proper production quality, the outer dimension of *Main section 2* is set at 570 mm. To simplify the dimensions, the wingtip hinge location is placed 1100 mm from the root, resulting in the dimensions shown in Figure 3.1. In the preliminary design, the distance from the trailing edge to the aileron hinge line is set to 25% of the total chord length. The wingtip hinge line is set at a 15-degree flare angle (Λ) with respect to the freestream velocity, and zero sweep and taper ratio are applied to the wing.
The geometric parameters used in Figure 3.1 and their description are summarized in Table 3.4.

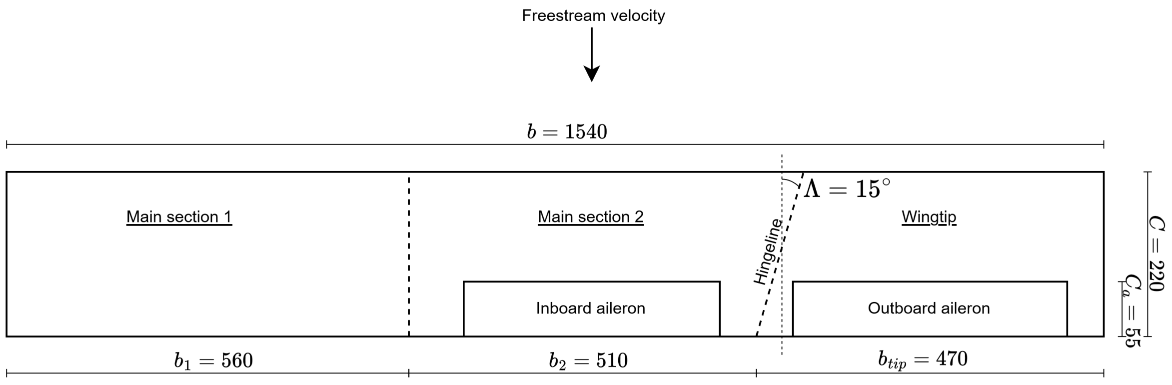

Figure 3.1: 2D preliminary planform design (not to scale)

Table 3.4: 2D planform parameters, descriptions, and values

Parameter	Description	Value
b	Semi-span	1540 mm
b_1	Span of *Main section 1*	560 mm
b_2	Span of *Main section 2*, measured at trailing edge	510 mm
b_{tip}	Span of wingtip, measured at trailing edge	470 mm
C	Chord length	220 mm
C_a	Aileron chord length	55 mm
AR	Aspect Ratio	14
Λ	Flare angle	15°

3.2.2. 3D PRELIMINARY DESIGN

After completing the main planform sizing, a preliminary 3D CAD model is created, which includes the essential geometry but lacks detailed features, as shown in Figure 3.2a and Figure 3.2b. This section outlines the high-level design choices reflected in the 3D model.

First, the wing is primarily hollow, with ribs and solid leading and trailing edge. Second, an aluminium plate (highlighted in orange) passes through the middle of the chord, extending from the root to the hinge. This design enables a lightweight 3D-printed structure combined with an aluminium plate that serves as the wing spar and largely determines the structural behavior of the wing.

The ribs are spaced 35 mm apart and have a thickness of 5 mm. However, the ribs at the root, the tip, and the connection between *Main section 1* and *Main section 2* are thicker to account for the higher stress concentrations that may occur at these locations. Cut-outs are made in the main wing and the wingtip at the expected aileron locations. At the locations of the cut-outs, the trailing edge spar is thickened to properly transfer the aileron loads into the structure.

In *Main section 2*, the wing is designed to be partially solid near the hinge, allowing space for the hinge mechanism during the detailed design phase. The entire wing will be covered with Oracover[2] to ensure a consistent surface finish. A symmetric NACA 0016 airfoil is selected to provide sufficient thickness for housing the internal components of the wing, resulting in a maximum thickness of 35.2 mm. During the detailed design phase, it will be assessed whether the maximum thickness provides sufficient internal space to accommodate all components.

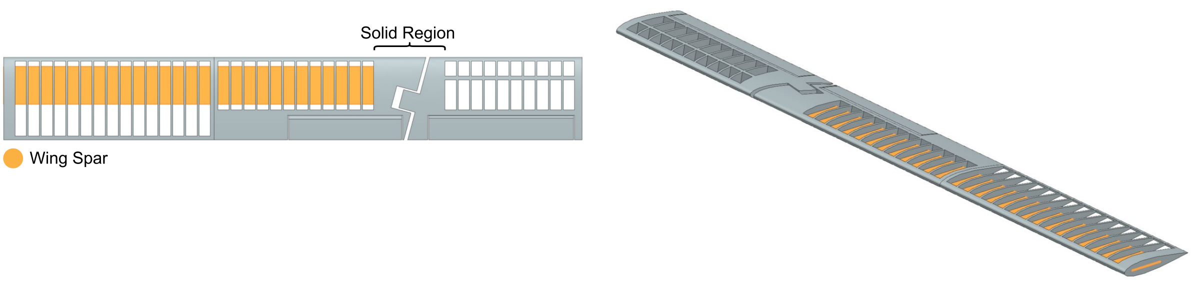

(a) Top view

(b) Isometric view

Figure 3.2: 3D preliminary CAD design - comparison of top and isometric views

[2]See "Oracover," Lanitz-Prena Folien Factory GmbH, https://www.oracover.de/katalog/artikelinfo/1062/oracover-iron-on-film---width_-60-cm---length_-2-m.

4

Sizing

This chapter outlines three distinct sizing processes. In Section 4.1, the inboard and outboard ailerons are sized to meet requirements *Req-1* and *Req-2*, respectively. in Section 4.2, the servo actuator sizing is performed for both the aileron servo actuators and the hinge mechanism servo actuator to fulfill requirements *Req-1* and *Req-6*, respectively. Thirdly, in Section 4.3 the wing spar is sized to satisfy requirements *Req-3*, *Req-4*, *Req-5* and *Req-5*.

4.1. Aileron Sizing

The process of determining appropriate aileron sizes involves two key aspects: creating an aerodynamic model of the wing and addressing the specific requirements for the inboard aileron and the outboard aileron.

4.1.1. Aerodynamic modeling

Aileron sizing takes place early in the design phase of the demonstrator and requires multiple iterations to refine the design. To support this process, an analysis method that can quickly calculate the aerodynamic forces and moments for different aileron configurations, is essential. Selecting the appropriate analysis tool involves balancing accuracy against complexity and computational time. While sophisticated Computational Fluid Dynamics (CFD) models can deliver highly accurate results, their setup, calculations and post-processing demand considerable time, making them unsuitable for rapid iterative design. Instead, the Athena Vortex Lattice (AVL) model is chosen as the aerodynamic analysis tool. Despite its notable drawbacks compared to CFD models, AVL's relatively quick analysis of wings, including control surfaces, makes it the preferred choice for aileron sizing, where rapid analysis of the design space is critical. AVL is well-suited for analyzing lifting surfaces and, due to its linear aerodynamic assumptions and steady-state approach, performs best at small angles and relatively slow pitch, roll, and yaw rates [38]. To analyze the wing in AVL, its planform must be structured to meet AVL's input requirements. The wing is divided into parallel sections, with each section defined by its chord properties. Specifically, the following parameters are specified for each section: the leading-edge position, the airfoil used, and the presence of an aileron. If an aileron is present at that section, the position of the hinge line is also specified. For aerodynamic analysis, the wing is further subdivided into panels. To determine the lift distribution, AVL calculates the lift at spanwise strips. The width and number of strips is a result of the discretization of the wing.

In order to process the aerodynamic forces on the strips, an important simplification is applied to how the planform is modeled. As can be seen in Figure 4.1, the hinge line is modeled in parallel with the freestream direction. Four practical geometric constraints must be considered when sizing the inboard aileron. One key constraint is the placement of the wingtip-side edge of the aileron. Positioning it directly at the hinge line would result in an excessively thin wing structure near the hinge, compromising structural integrity. To accommodate the hinge mechanism and ensure proper load transfer to the wing, the inboard aileron is set 40 mm inboard from the trailing edge of the main wing section. In Figure 4.2, the limit of the inboard aileron is indicated in at "Limit 1". Additionally, since the main section is divided into two parts for manufacturing, a design choice was made to set the maximum span of the inboard aileron to 90% of the span of *Main section 2*.

For the outboard aileron, two sizing limits are defined. At the tip, a 20 mm margin is maintained to provide sufficient space for the last rib of the wingtip. Additionally, a margin relative to the wingtip hinge line is imposed. The maximum allowable span of the outboard aileron is set at 90% of its maximum possible span. A 100% span would mean the hinge line of the aileron ends precisely at the start of the wingtip hinge gap. If the hinge line of the outboard aileron were shifted upward or downward, the maximum allowable span would decrease or increase accordingly. This limit is illustrated in Figure 4.2 and labeled as "Limit 2".

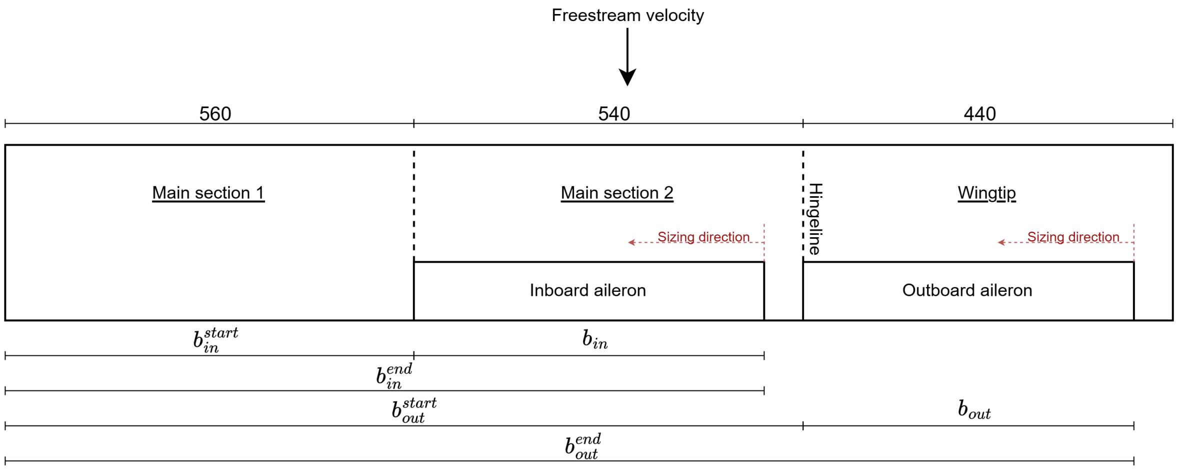

Figure 4.1: 2D preliminary planform design

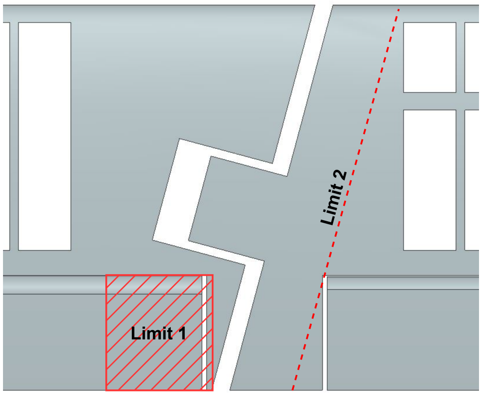

Figure 4.2: Aileron sizing limits

To conclude the wing's geometric modeling in AVL, an isometric view of the wing is shown in Figure 4.3. The following sections detail the sizing procedures for both the inboard and outboard ailerons.

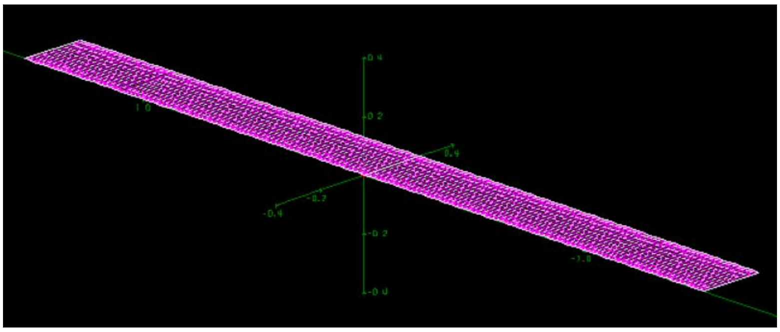

Figure 4.3: Isometric view of wing representation in AVL

At higher angles of attack, boundary layer effects and flow separation become increasingly significant. To account for these effects in 2D, XFOIL can be used. By modeling the boundary layer and separation, XFOIL provides more accurate lift predictions compared to purely linear methods.
In Section 4.1.2, a combination of 2D XFOIL analysis and 3D lift distribution is used to derive a more realistic roll rate. Within XFOIL, the airfoil geometry, flow conditions, aileron hinge location, and aileron deflection angle are specified. A sweep of angles of attack is then conducted, and the resulting $C_l - \alpha$ curve is retrieved. By sweeping the deflection angle from $-20°$ to $20°$ degrees, the lift curve as a function of the deflection angle($C_l - \alpha(\delta)$) is obtained. The representation of the airfoil with a $-20°$ aileron deflection in XFOIL is presented in Figure 4.4:

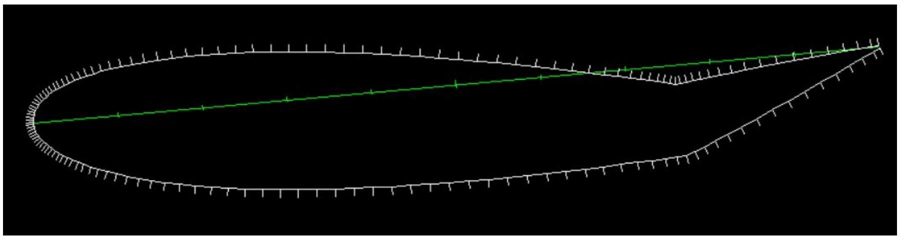

Figure 4.4: NACA 0016 airfoil with $-20°$ deflected aileron in XFOIL

4.1.2. INBOARD AILERON: SIZING PROCEDURE AND RESULTS

The inboard aileron is sized to satisfy requirement *Req-1*, i.e. achieving a steady-state roll rate of 15 degrees per second with a maximum deflection of 20 degrees up or down. This requirement is intended to ensure that the demonstrator's inboard aileron behaves similarly to the control surfaces of a CS-25 certified aircraft. To investigate this requirement, the roll rate is calculated as if the wing had a mirrored counterpart and was performing a steady-state roll in free flight.
When the right aileron is deflected downwards, an increase in lift is generated at that section of the wing. Simultaneously, the left aileron will deflect upwards, and a local decrease in lift is generated. This will generate a counterclockwise rolling moment around the center, leading to a rotational acceleration that increases the roll rate. In a rolling motion, at each position of the wing, there is a change in local angle of attack and thus in lift, opposite to the local velocity due to roll. This will create a moment in opposite direction to that of the roll rate, which will be equal to that of the moment due to the aileron deflection at a specific roll rate, which is called roll damping, and the damped roll rate (steady-state roll) is computed in the sizing procedure of the inboard aileron. In Figure 4.5, the distributed force due to the deflected ailerons is displayed as $F_{\delta_{up}}$ and $F_{\delta_{down}}$, the distributed change in local lift is indicated as F_{roll}, and the roll rate is indicated as p.

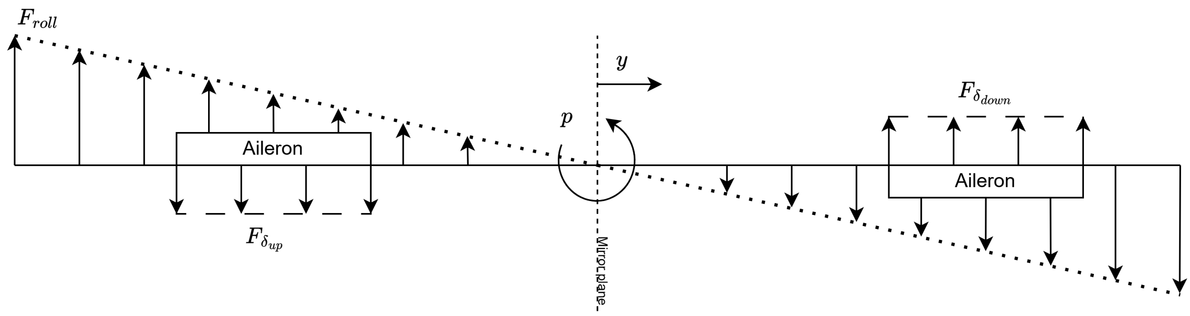

Figure 4.5: Distributed change in lift and aileron force in rolling motion

AVL has a build in function to compute the damped roll rate. However, by the linear relation between the angle of attack and the lift in AVL, the roll rate is found to be heavily over-predicted. As mentioned before, AVL is mostly suitable for small angles. However, due to the local change in angle of attack due to roll and the aileron deflection, angles are no longer small. Therefore, the AVL results become unreliable. And thus, another approach is used to compute the damped roll rate.

To achieve a damped roll rate, the sum of moments around the center must equal zero. In Equation (4.1), $M_{F_{roll}}$ represents the moment contribution due to the distribution change in local lift F_{roll}, while $M_{F_{\delta_{up}}}$ and $M_{F_{\delta_{down}}}$ are the moment contributions resulting from the distributed changes in local lift $F_{\delta_{up}}$ and $F_{\delta_{down}}$, respectively, caused by the aileron deflections.

$$\sum M_{roll} \rightarrow M_{F_{roll}} + M_{F_{\delta_{up}}} + M_{F_{\delta_{down}}} = 0 \tag{4.1}$$

To incorporate the 2D analysis described in Section 4.1.1, the span is divided in 300 equally spaced sections. To compute the rolling moment from Equation (4.1), the lift force of each section (L_j) is computed, and multiplied by the spanwise location (y_j). Summing the contribution of each section from tip to tip results in the total rolling moment, as stated by Equation (4.2)

$$M_{roll} = \sum_{j=1}^{300} L_j(y_j) \cdot y_j \tag{4.2}$$

To compute the local lift (L_j) of a section, the dynamic pressure ($\frac{1}{2}\rho V^2$) is multiplied chord length (C) and the width of the section (w_j), and the local lift coefficient $C_l(\alpha_j)$.

$$L_j = \frac{1}{2}\rho V^2 C w_j C_l(\alpha_j) \tag{4.3}$$

At each section, the change in local angle of attack α^p due to a roll rate (p) at distance y from the center can be computed by using Equation (4.4).

$$\alpha_j^p(y_j) = \tan^{-1}\left(\frac{-p \cdot y_j}{V}\right) \tag{4.4}$$

By adding the local change in angle of attack to the angle of attack α at which the wing is analyzed, the local angle (α_j) of attack at each spanwise location is be obtained:

$$\alpha_j(y_j) = \alpha + \alpha_j^p(y_j) \tag{4.5}$$

From the $C_l - \alpha(\delta)$ curves computed in XFOIL, and the local angle of attack as a function of spanwise position, the $C_l(\alpha_j)$ can be computed. Since the lift curves are computed for each deflection angle, the summation in Equation (4.2) must follow the condition of the statement Equation (4.6) below. Where b_{in}^{start} and b_{in}^{start} define the location of the inboard aileron, as shown in Figure 4.1. This will ensure that, if no aileron is present at the evaluated section, the lift curve of the undeflected airfoil is picked. If an aileron is present in the section, the lift curve of the corresponding deflection is selected.

$$\delta = \begin{cases} \delta, & \text{if } b_{in}^{start} \leq |y| \leq b_{in}^{end}, \\ 0, & \text{otherwise.} \end{cases} \tag{4.6}$$

Now, all ingredients are available to calculate the rolling moment for a given configuration. However, this method relies on the 2D lift coefficient of each section. A 3D lift distribution is required to have a more accurate roll rate prediction. In order to incorporate 3D effects in this method, the elliptical lift distribution is applied. The elliptical circulation distribution can be computed with Equation (4.7).

$$\Gamma(y) = \Gamma_0 \sqrt{1 - \left(\frac{2y}{b}\right)^2} \tag{4.7}$$

Where the lift L' per unit span as a function of circulation is given by:

$$L' = \rho V \Gamma \tag{4.8}$$

So, the spanwise circulation distribution can be converted to a spanwise lift distribution. This 3D elliptical lift distribution is used as a spanwise scaling factor to account for 3D effects in the 2D analysis, by creating the factor f_{3D} in Equation (4.9)

$$f_{3D} = \sqrt{1 - \left(\frac{2y}{b}\right)^2} \tag{4.9}$$

After applying f_{3D} as a scaling factor to the schematic lift distribution drawn in Figure 4.5, the shape of the lift distribution will change to:

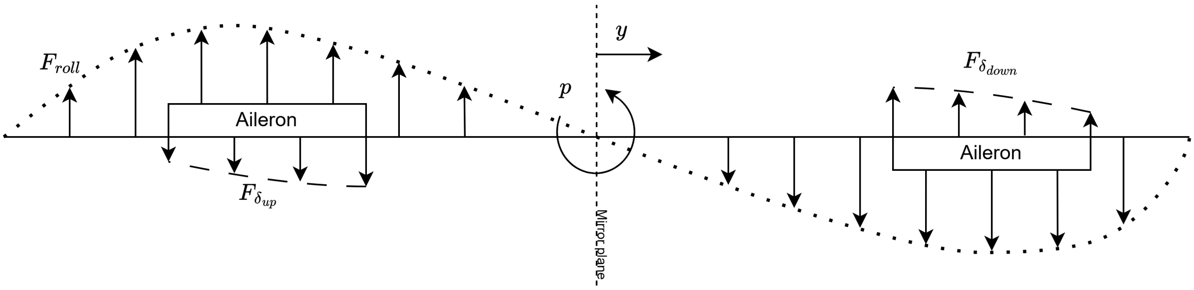

Figure 4.6: Distributed change in lift and aileron force in rolling motion with 3D correction factor f_{3D}

Combining Equation (4.3) and Equation (4.9) leads to the following equation for the lift of a section:

$$L_j = \frac{1}{2}\rho V^2 C w_j C_l(\alpha_j) f_{3D} \tag{4.10}$$

In Matlab, for each aileron deflection, the roll rate is computed. To find the damped roll rate, the rolling moment M_{roll} is computed with Equation (4.2) for the aileron deflection at zero roll rate ($p = 0$). Then, p is steadily increased and, at each step, M_{roll} is computed. The roll rate at which M_{roll} switches sign is considered as the damped roll rate.

The above set of roll rates and aileron deflections correspond to a certain combination of b_{in}^{start} and b_{in}^{end} As mentioned earlier, b_{in}^{end} is fixed at 1025 mm. The aim of this sizing procedure is to find an aileron size that satisfies requirement *Req-1*. Therefore, the span of the inboard aileron is varied from 40% of the span of *Main section 2*, to 90% of *Main section 2*. From the above analysis, the relation between the aileron deflection angle and damped roll rate is plotted for different aileron sizes, together with the area that corresponds to the requirement *Req-1*. This allows for easy visual identification of the correct size of the inboard aileron.

AVL RESULTS

First, the results of merely using the AVL to find the damped roll rate are presented. Later on, by implementing the procedures described above, the results a 2D correction and a 3D lift distribution correction factor are presented.

By simulating the demonstrator in AVL and sweeping the inboard aileron deflection angle from $-20°$ to $20°$ in steps of $2.5°$ and exporting the body-axis results, the most basic damped roll rate is analyzed. This analysis have been performed at $\alpha_{n=1} = 2°$ and $\alpha_{n=2.5} = 5°$ and the results are plotted in Figure 4.7 and Figure 4.8, respectively. The roll rate is plotted on the vertical axis, and the aileron deflection angle is plotted on the horizontal axis. In both graphs, the solid lines correspond to analysis that have been performed at $V_{min} = 15$ m/s, while the dashed lines correspond to the analysis at $V_{max} = 25$ m/s. Different colors correspond to different aileron sizes, which are indicated in the legend as a fraction of b_{in}, as defined in Figure 4.1. At a first glance, two main observations can be made: First, the increase in roll rate with an increase in aileron deflection is linear. Secondly, the plot is point symmetric through the origin, which means that an opposite aileron deflection will cause the same roll rate, but in opposite direction. Both are a result of the linear nature of AVL. It can also be observed that the roll rate decreases for a decreasing velocity. This is in line with the expectations. As can be observed in Equation (4.4), for a fixed roll rate, the change in local angle of attack is larger at a lower velocity. This will increase the damping of the wing, and thus decrease the roll rate at lower velocities. At last, the roll rate logically increases by increasing the span of the inboard aileron.

Lastly, by comparing Figure 4.7 and Figure 4.8, it can be observed that the angle of attack does not have any effect on the roll rate.

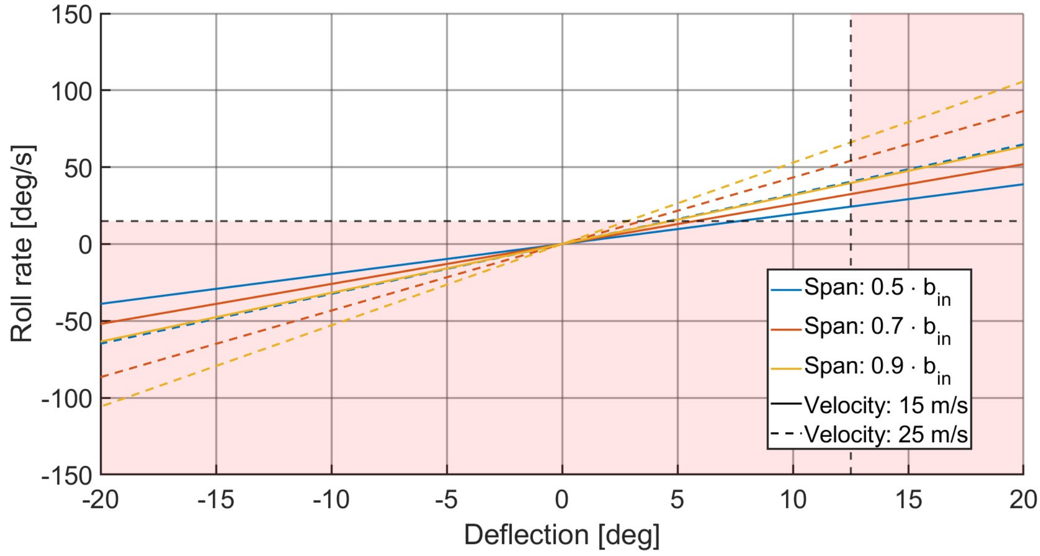

Figure 4.7: Roll rate vs. deflection angle of the inboard aileron - AVL analysis at $\alpha_{n=1}$

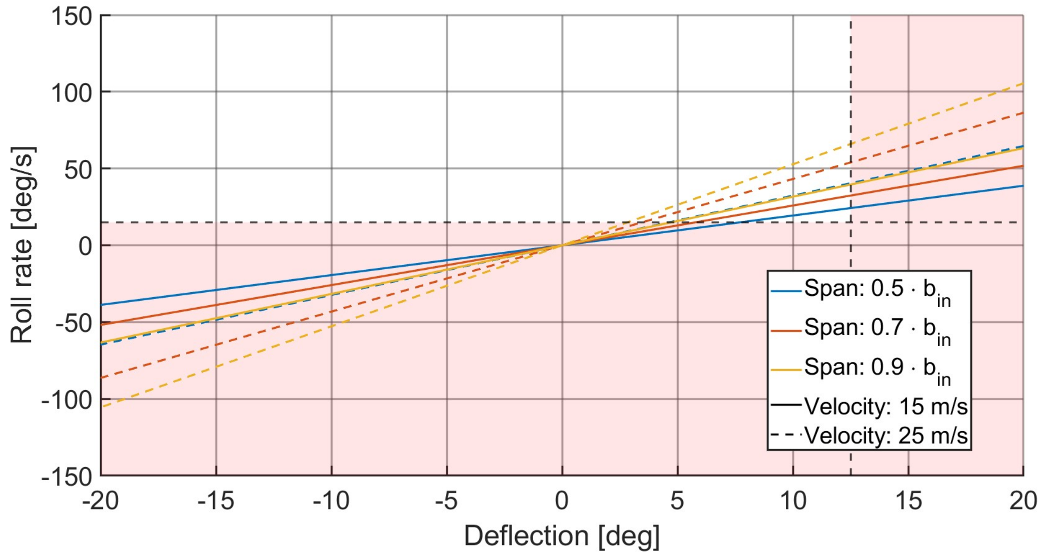

Figure 4.8: Roll rate vs. deflection angle of the inboard aileron - AVL analysis at $\alpha_{n=2.5}$

2D CORRECTION RESULTS

Now, a change from the AVL analysis to the 2D viscous analysis and a 3D lift distribution scaling factor is made. At first, a lift distribution without a 3D correction (Equation (4.9) is presented in as the blue line in Figure 4.9. This line is an example of the lift distribution with the viscous 2D analysis, but without the 3D scaling factor. This lift distribution is computed at $\alpha_{n=}$, which explains why the lift coefficient at the center is above zero. Due to the 3D scaling factor not being applied, the lift does not drop to zero at the tips. The lift distribution corresponds to an aileron deflection of 20° and the maximum aileron size. In the legend of the graph, the damped roll rate is presented: 28.1 deg/sec.

Now, the 3D correction is applied, resulting in the orange line in Figure 4.9. It can be seen that the lift coefficient at the tips on both sides drop to zero. Another interesting observation is the reduction at lift on both ailerons. The 3D scaling factor does not only decrease the peak lift force of the ailerons (or downforce), but it also makes the lift decrease faster following both ailerons towards the tip. The reduction of lift towards the tips would suggest that the damping would decrease, while the decrease in effectiveness of the ailerons would suggest a lower roll rate. It can be seen, that by implementing the 3D scaling factor, the damped roll rate increased to 39.0 deg/sec as indicated in the legend. This suggests that the reduction in damping is far more dominant than the reduction in effectiveness of the ailerons.

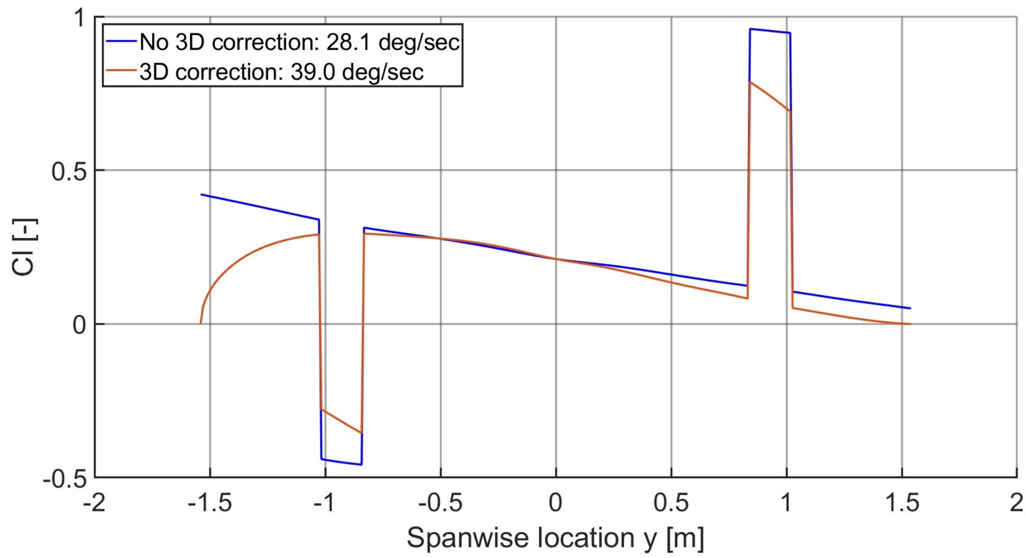

Figure 4.9: Lift distribution at damped rolling motion without and without 3D lift distribution correction

The results of the improved roll rate analysis are presented in Figure 4.10 and Figure 4.11. Like Figure 4.7 and Figure 4.8, the vertical axis displays the roll rate, and the horizontal axis displays the aileron deflection angle. The analysis have been performed at $\alpha_{n=1}$ and $\alpha_{n=2.5}$, and similar to Figure 4.7 and Figure 4.8, the solid and dashed lines correspond to V_{min} and V_{max}, respectively, while the different colors correspond to a difference in span of the inboard aileron as a fraction of b_{in}. It can directly be observed that the roll rate no longer behaves linear with respect to the aileron deflection. Secondly, by comparing the AVL analysis and the 2D corrected analysis, it can be observed that the viscous analysis predict a far lower roll rate for a given deflection angle. The first observation follows directly from the implementation of the 2D viscous analysis. At relatively low angles of attack, lift curves often behave close to linear. However, at higher angles of attack, the behavior becomes less linear as boundary layer effects become more dominant. The decrease in roll rate would suggest that the damping relative to the aileron effectiveness is increased. This might be explained due to the effect that an aileron deflection would cause the viscous effects to have a more dominant role, and that larger aileron deflections are not as effective as predicted by linear theory. Comparing Figure 4.7 with Figure 4.8 supports this theory, as the increase in angle of attack introduces a small reduction in roll rate.
A horizontal dashed line is drawn at a roll rate of 15 deg/sec, which is the required roll rate as specified by *Req-1*. Secondly, a vertical dashed line is drawn at an aileron deflection of 12.5°. Due to the increase in slope after this point, the results might not be completely reliable at higher deflections. Therefore, the sizing deflection is put at 12.5°, instead of the earlier specified 20°. This approach is likely to result in a conservative design, increasing confidence that the requirement will be met during testing. Therefore, the area above the horizontal dashed line and to the left of the vertical dashed line represents the feasible region. The area outside this region is highlighted in red, indicating infeasibility.

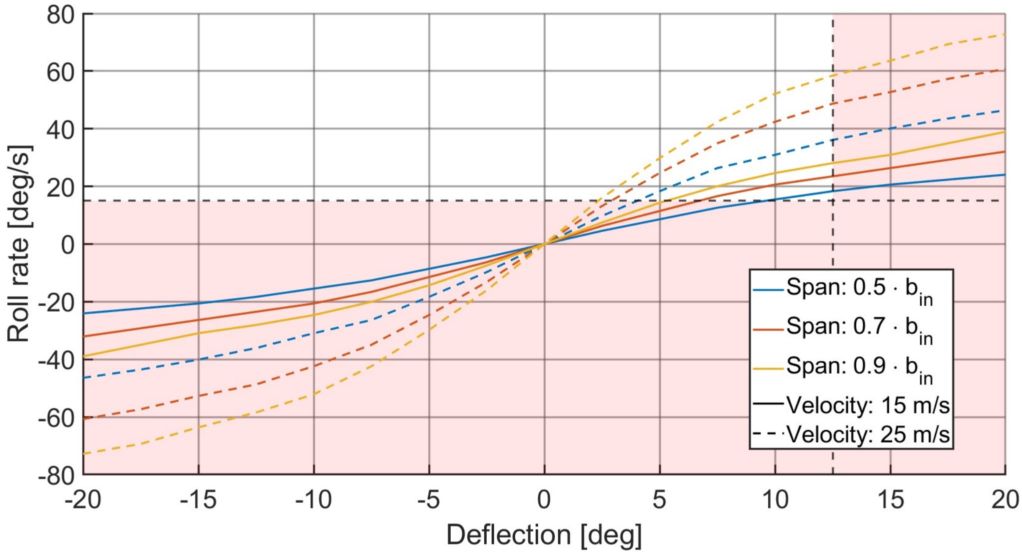

Figure 4.10: Roll rate vs. deflection angle of the inboard aileron - 2D viscous analysis at $\alpha = 2°$

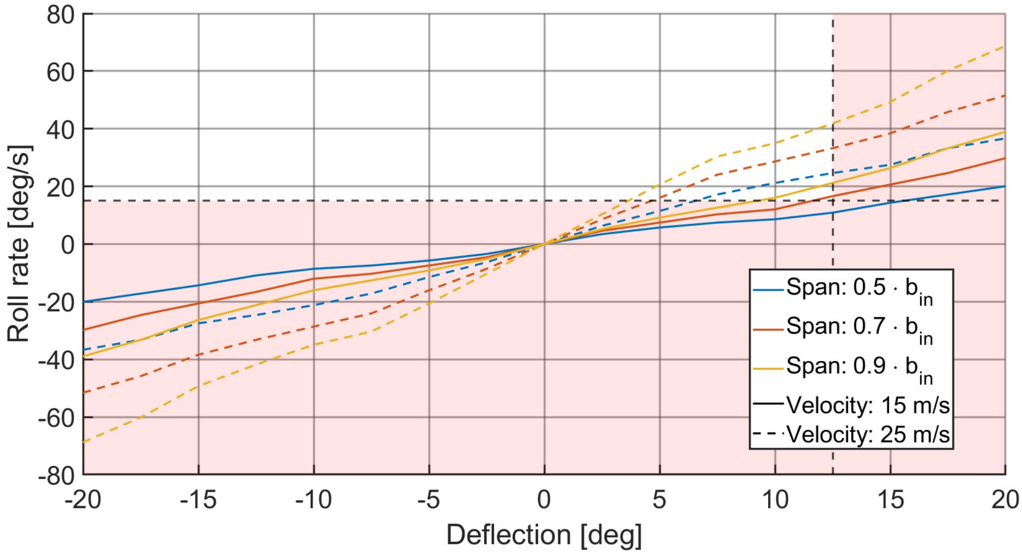

Figure 4.11: Roll rate vs. deflection angle of the inboard aileron - 2D viscous analysis at $\alpha = 5°$

The results of Figure 4.10 and Figure 4.11 give a proper insight in the change in roll rate with respect to the aileron deflection at different conditions. However, it is difficult to choose the correct aileron size with this graph. To make the sizing selection more clear, Figure 4.12 shows how the roll rate changes with the aileron span. In this graph, the aileron deflection is fixed at 12.5°. Again, the horizontal line at 15 deg/sec indicates the performance requirement. The intersection where the largest span value is required to reach the desired roll rate is marked with a circle, and the corresponding span size is shown in the legend. A span size of 0.65 corresponds to an aileron span of 65% of *Main section 2*, as described in Section 4.1. As a conservative measure, this result is rounded up, resulting in an aileron span of 70% of *Main section 2*.

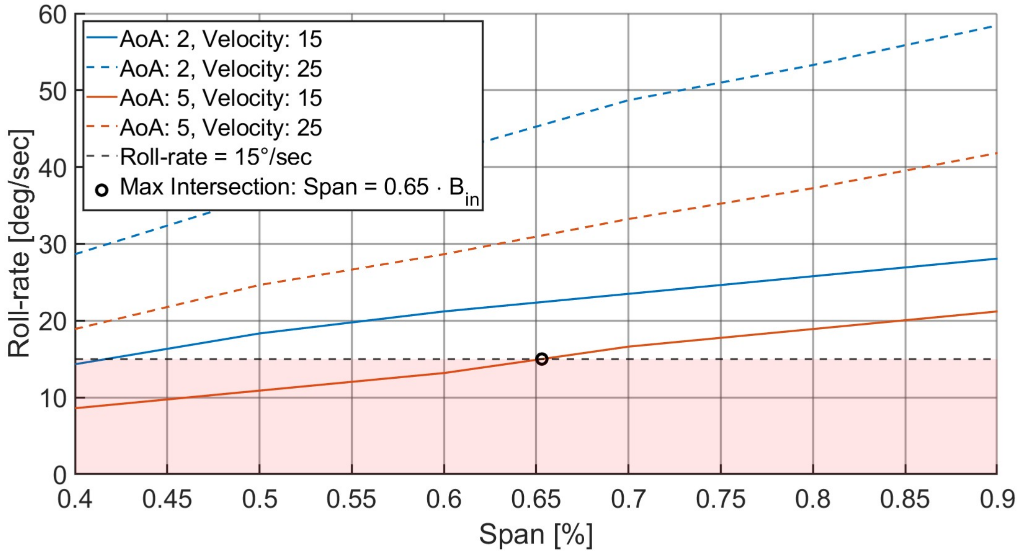

Figure 4.12: Roll rate due to the inboard aileron vs. aileron span

4.1.3. OUTBOARD AILERON: SIZING PROCEDURE AND RESULTS

In an unlocked hinge condition and at a positive angle of attack, the wingtip experiences an upward lift force that causes it to rotate upwards. As shown in Eq. (2.1), the angle of attack of the wingtip decreases as the fold angle decreases. Neglecting the weight of the wingtip, equilibrium is reached when the moment around the hinge line due to lift equals zero.

The outboard aileron is sized to satisfy requirement *Req-2*, ensuring the outboard aileron can return the wingtip to a horizontal position with a maximum deflection of 20 degrees up or down. To minimize the number of conditions requiring analysis, the worst-case scenario is considered. If the aileron is designed for this condition, it will meet the requirement under other conditions as well.

Without aileron deflection, the wingtip reaches an equilibrium position in an upwardly rotated state. When the outboard aileron is deflected upward, the wingtip rotates downward, achieving a new equilibrium position with an increased local angle of attack. As the wingtip approaches the horizontal position, greater aileron deflection or size is required. The worst case is the horizontal position, as rotating the wingtip further down would pass the locked hinge condition, requiring an unnecessarily large aileron. By designing the wing to be tested at positive angles of attack while neglecting the wingtip's weight, a conservative approach is taken, ensuring greater confidence in the aileron's performance.

To compute the moment around the hinge line, first, the lift distribution over the wingtip is computed. For this, the wing is modeled in AVL as described in the beginning of Section 4.1.1 and as visualized in Figure 4.1. As mentioned before, AVL is most suitable for small angles. The large maximum aileron deflection of ±20° can no longer be viewed as small angles. Therefore, a combination of AVL and a 2D correction method to account for viscous effects is applied.

In order to compute the 3D lift distribution with AVL, and use XFOIL for a 2D correction method, an important simplification is made. The viscous effects are simplified to 2D effects. This allows for a method in which the change from 2D theoretical lift to 2D viscous lift can be used as a factor to correct for the 3D analysis. This 2D correction factor is computed by analyzing the expected 2D lift coefficient with a lift curve slope of 2π, and the lift coefficient computed with the viscous analysis in XFOIL. After loading the geometry and flight conditions into AVL, the lift distribution across spanwise strips is computed, providing the initial lift distribution. For each strip, AVL also returns the induced angle of attack α_i.

In Matlab, the lift distribution, the deflection angle of the outboard aileron, and the change in local angle of attack serve as inputs to the 2D correction factor. For each spanwise strip, a check is performed to determine the presence of the aileron using the condition specified in Equation (4.11). Based on this condition, the corresponding lift polar for the given deflection is selected.

$$\delta = \begin{cases} \delta, & \text{if } b_{out}^{start} \leq |y| \leq b_{out}^{end}, \\ 0, & \text{otherwise.} \end{cases} \tag{4.11}$$

First, using the selected polar, the angle of attack at which the lift is zero is computed (α). By combining the angle of attack at which the wing is analyzed and the induced angle of attack (α_i), the theoretical lift coefficient ($C_{l_{theory}}$) is calculated with Equation (4.12).

$$C_{l_{theory}} = 2\pi * (\alpha + \alpha_i) \tag{4.12}$$

Using the local angle of attack ($\alpha + \alpha_i$) and the lift curve from XFOIL, the viscous 2D lift coefficient ($C_{l_{visc}}$) is found. Combing both results in the 2D correction factor ($f_{2D/3D}$) presented in Equation (4.13).

$$f_{2D/3D} = \frac{C_{l_{visc}}}{C_{l_{theory}}} \tag{4.13}$$

Resulting in a corrected 3D lift coefficient for each section by multiplying the lift coefficient from AVL ($C_{L_{AVL}}$) with the 2D correction factor, as stated in Equation (4.14).

$$C_{L_{corr}} = C_{L_{AVL}} \cdot f_{2D/3D} \tag{4.14}$$

Secondly, at each spanwise strip the center of pressure is retrieved from the viscous 2D analysis in XFOIL. The location of the center of pressure will later be used to calculate the wingtip moment contribution of each strip.
To calculate the moment due to the lift distribution on the wingtip, the spanwise strips are first filtered to keep the strips that form the wingtip, i.e. where $b > b_{hinge}$. For each strip, the distance from the center of pressure to the hinge line is computed. This distance is the moment arm for that specific strip. Multiplying the lift of that strip by the moment arm will correspond to the moment contribution of that strip. To compute the moment arm, first, the additional spanwise distance due to the center of pressure location is required (Δy_{cp}) by Equation (4.15).

$$\Delta y_{cp} = x_{cp} \tan(\Lambda) \tag{4.15}$$

In the above equation, x_{cp} is the distance from the center line to the center of pressure and Λ is the flare angle, with the sign convention as indicated in Figure 4.13. In this image, intersection of the hinge line and the center line of the wing is indicated by the blue dot, and the center of pressure location is indicated with a red dot. This image serves as aid to understand the calculations, and is not to scale or does not represent a realistic center of pressure location.

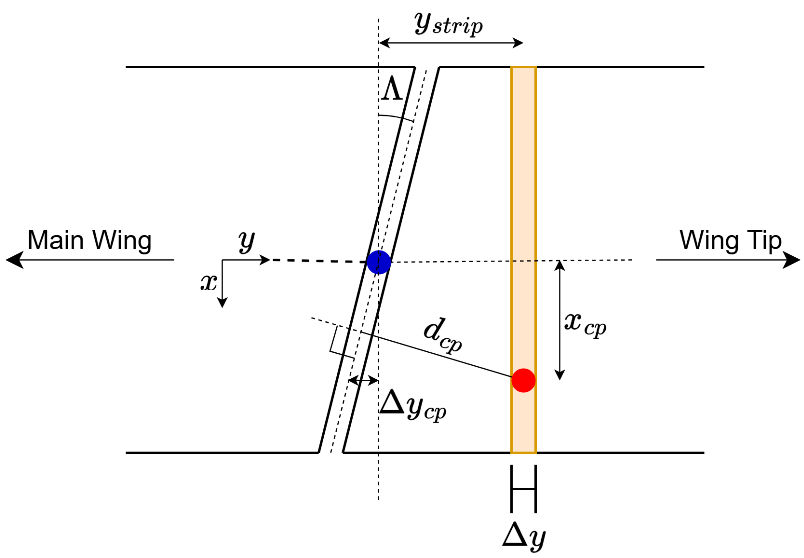

Figure 4.13: Moment arm due to center of pressure location

The distance from the hinge line to the center of pressure, and thus the moment arm of that strip (d_{cp}), can be calculated with Equation (4.16).

$$d_{cp} = (y_{strip} + \Delta y_{cp})\cos(\Lambda) \tag{4.16}$$

By calculating the lift force of each strip, and multiplying this by the distance to the hinge line (d_{cp}), Equation (4.17) is used to find the moment contribution of each strip. In this equation, Δy corresponds to the width of the strip, and C corresponds to the chord length. By performing this operation for all strips on the wingtip, and summing all moment contributions, the total moment is found.

$$M_{strip} = \frac{1}{2}\rho V^2 C_{L_{corr}} \Delta y C \cdot d_{cp} \tag{4.17}$$

By calculating the moment while evaluating the condition in Equation (4.11), the moment for a specific aileron size is calculated. The end location of the aileron (b_{out}^{end}) is fixed at 1520 mm, as shown in Figure 4.1. So, to size the aileron, the start location (b_{out}^{start}) can be varied. Secondly, the aileron hinge location can be varied in chordwise direction, while adhering to Limit 2, shown in Figure 4.2. Similar to the inboard aileron, the span of the outboard aileron is varied between 90% and 40% of the available wingtip span, where 90% of the span corresponds to Limit 2. This means, that for a larger aileron chord, and thus moving the aileron hinge line up, the maximum span of the aileron decreases.

SIZING RESULTS - THE OUTBOARD AILERON

Following the method above and similar to the visualizations of the inboard aileron sizing, the results are presented in graphs illustrating the relationship between the wingtip moment and the outboard aileron deflection angle. These graphs depict variations for different aileron sizes at both V_{min} and V_{max}. The aileron spans in the legend are presented as a fraction of B_{out}, which is shown in Figure 4.1.Figure 4.14 corresponds to the analysis at $\alpha_{n=1}$, and Figure 4.15 correspond to the analysis at $\alpha_{n=2.5}$. The horizontal dashed line is put at a wingtip moment of 0 Nm, and all points below that line will satisfy the requirement for the outboard aileron. The vertical dashed line corresponds to an aileron deflection of $-12.5°$. As explained in Section 4.1.2, the reliability of the viscous correction above this deflection might not be sufficient to size the ailerons. The region indicating infeasibility is marked in red.

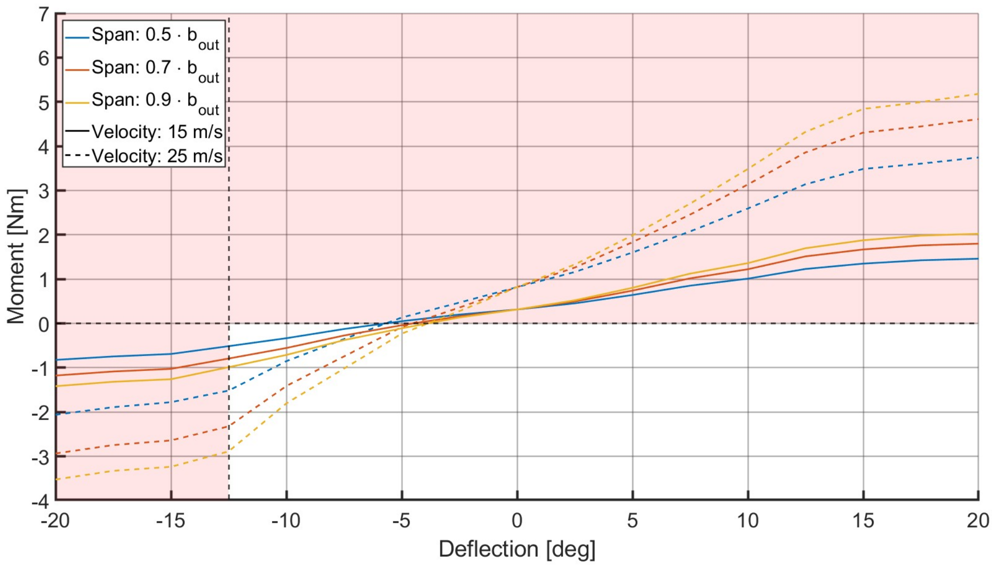

Figure 4.14: wingtip moment vs. deflection angle of the outboard aileron - $\alpha = 2°$

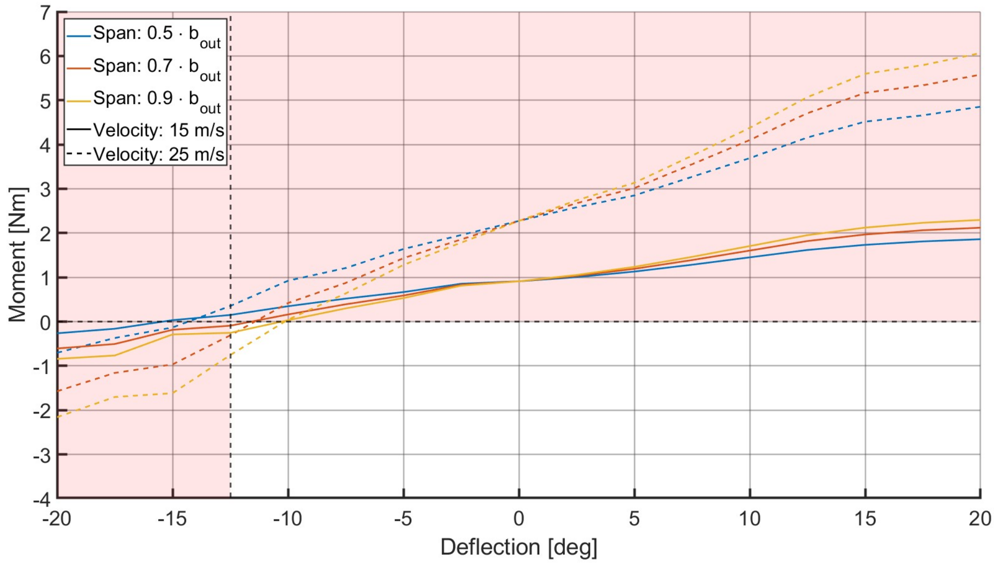

Figure 4.15: wingtip moment vs. deflection angle of the outboard aileron - $\alpha = 5°$

The lines in Figure 4.15 are clearly shifted up with respect to the lines in Figure 4.14. This is a clear consequence of the increased angle of attack, which increases the lift, and thus moment, on the wingtip. As can be seen in Figure 4.14, for V_{max} only 3 lines can barely provide zero or negative moment at an aileron deflection of $-12.5°$ or less.
Although this would satisfy the requirement, the effect of an increase in aileron chord on the wingtip moment is investigated. Figure 4.16 plots the wingtip moment versus the chordwise position of the aileron hinge line (X/C). The deflection is fixed at $-12.5°$ and the span is fixed at 90% of the available span, corresponding to the limit in Figure 4.2. Lowering this number represents moving the aileron hinge line closer to the leading edge. As could also be observed by comparing Figure 4.14 and Figure 4.15, the test conditions at V_{min} and $\alpha_{n=2.5}$ are limiting the design. Against first expectations, the aileron hardly becomes more effective for an increase in chord length. Looking back at the sizing limits in Figure 4.2, it is clear that an increase in chord of the outboard aileron reduces the maximum span of the aileron. The lack of increase in effectiveness when increasing the aileron chord could be explained by the fact that the increase in chord length is canceled by the reduction in span. A sudden increase in aileron effectiveness is observed along the line corresponding to $\alpha_{n=2.5}$ and V_{max}. Since this trend is not reflected in the other data points, it is most likely an outlier caused by a convergence error in XFOIL.
For consistency with the inboard aileron, a hinge location of 75% of the chord length is selected. Although the outboard aileron can only provide little negative moment, and thus the margin is small, the analysis did not take into account the wingtip mass. In horizontal testing at positive angles of attack, the wingtip mass will help the wingtip to reach the neutral position, making the results conservative.

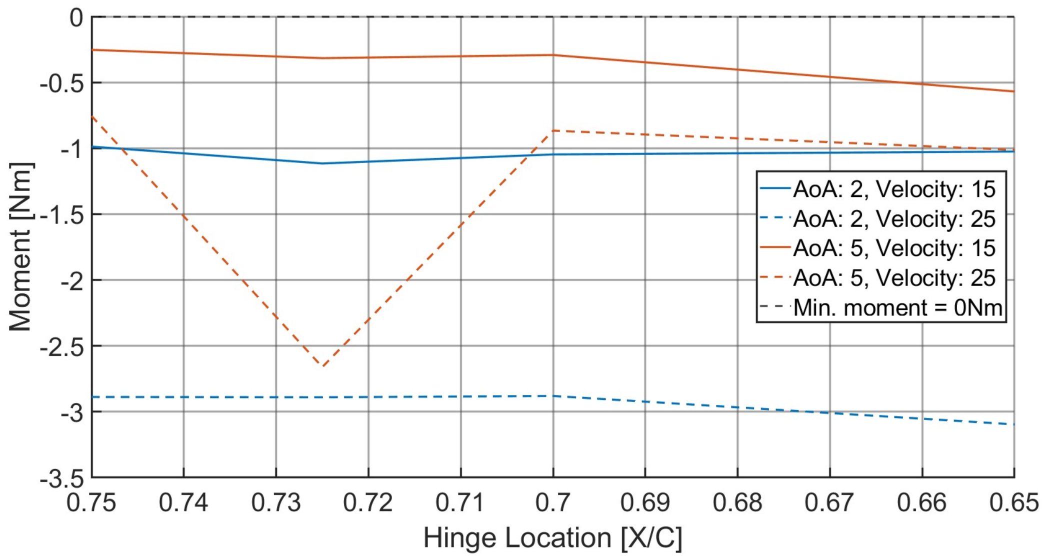

Figure 4.16: Chordwise hinge location of the outboard aileron vs. wingtip moment

The results of the sizing procedure for the inboard aileron (Section 4.1.2) and the outboard aileron (Section 4.1.3) are summarized in Table 4.8.

4.2. SERVO ACTUATOR SIZING

After sizing the inboard and the outboard aileron, their actuation servo must be sized. For both ailerons, requirements *Req-6* and *Req-8* must be satisfied, regarding the required servo actuator rotational speed and torque. For simplicity, a servo actuator that can satisfy the requirements for both ailerons is used for both ailerons. In addition to the servo actuator sizing of both ailerons, a servo actuator sizing of the hinge mechanism is performed. In order to satisfy requirement *Req-7*, the hinge servo actuator must be able to lock the wingtip in horizontal position in all flight conditions. This section will first cover the sizing procedure and results of the aileron servo actuator in Section 4.2.1, after which the sizing procedure and results of the hinge servo actuator are presented in Section 4.2.2. At last, the results of the sizing procedures of the aileron servo actuators are summarized in Section 4.4.

4.2.1. AILERON SERVO ACTUATOR: SIZING PROCEDURE AND RESULTS

Requirements *Req-6* and *Req-8* can be expressed by two numbers: the minimum rotational speed of the servo actuator ω_s, and the minimum torque T_s that the servo actuators must provide. In the servo industry, the rotational speed of servos is most often expressed as [sec / 60°] and the servo torque is most often expressed as [kg · cm]. To allow for an easy servo actuator selection process at the end, these units are used during the sizing procedure.
Requirement *Req-6* states that the aileron shall have a deflection frequency that is equal or higher than the second bending mode of the demonstrator. To satisfy this requirement, the first step is to find the bending modes of the demonstrator. In order to do so, the preliminary CAD model from Section 3.2 is transformed to a FEM model. Key aspect in the FEM model are the modeling of the: Ribs, leading and trailing edge, trailing edge at the aileron, the wing spar (designed as an aluminium plate), the 3D printed structure near the hinge, the Oracover skin, the ailerons, the point masses (accelerometers, hinge servo actuator and aileron servo actuators), the rib - spar connection, and the main wing - wingtip hinge connection.

In this section, the modeling of each item in the list will be addressed shortly, resulting in the FEM model of the preliminary design. In Figure 4.17, the CAD model and the FEM model of the main rib structure is compared. It can be seen that both leading and trailing edge are modeled as a 1D beam elements. Both leading and trailing edges are assigned with their respective cross sectional properties, which are retrieved from the CAD model. Secondly, the front and aft part of the ribs are modeled as 2D shell elements, with a thickness equal to that of the ribs (5 mm). Then, the rib section above and below the plate cut-out are modeled as beam elements, too. Although the preliminary CAD model suggests that this region is almost completely solid, which would be more accurately modeled by a shell element, this will not be the actual case. In the detailed design phase, a large cut-out is made above and below the current plate cut-out. This will allow for room to pass cables through. With this in mind, the 1D modeling of this section is justified. Thirdly, the rib - plate connection is marked in orange. The rib is connected to the plate by 4 RBE2 connections. The RBE2 connection represents a rigid connection with infinite stiffness. In this case, this simulates using insert screws to connect the plate to the ribs.

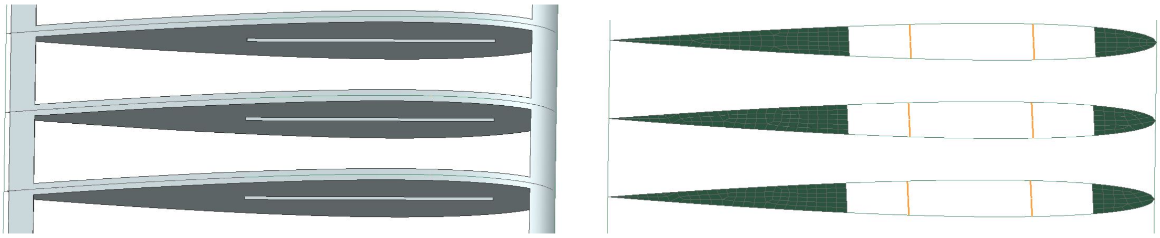

(a) Preliminary CAD of main rib structure

(b) Preliminary FEM of main rib structure

Figure 4.17: Comparison of preliminary CAD and FEM of main rib structure

In Figure 4.18, the CAD model and the FEM model of the rib structure at the inboard aileron is compared. The rib structure in Figure 4.17b and Figure 4.18b essentially has the same set-up. The trailing edge, however, is changed from a beam element to a shell structure with a thickness of 10 mm. This represents the trailing edge spar. Secondly, the aileron in Figure 4.18a is represented by the beam element in Figure 4.18b. In the preliminary design, the aileron is attached to a rib with a CBUSH at both ends, which represents a spring damper connection. At last, one can see a concentrated mass, connected to the aft part of two ribs. This concentrated mass represents the servo actuator weight for the aileron. A similar representation of the aileron servo actuator at the outboard aileron is used in the FEM model. The mass of both aileron servo actuators is put at 8.5 grams, which corresponds to the weight of servo actuators more often used to actuate control surfaces in RC planes.

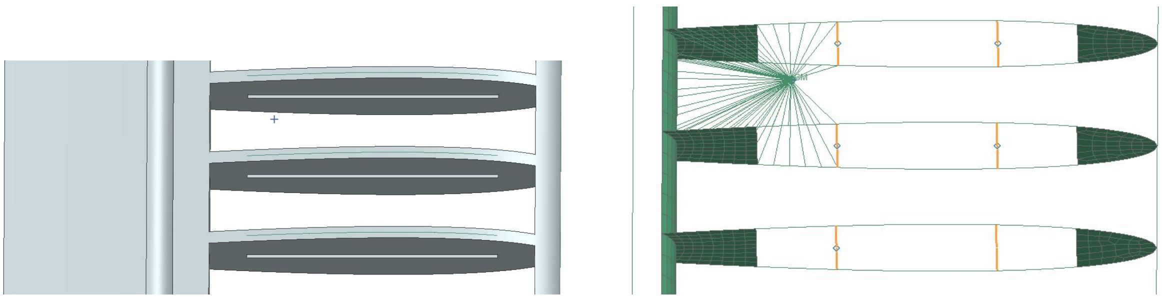

(a) Preliminary CAD of aileron rib structure

(b) Preliminary FEM of aileron rib structure

Figure 4.18: Comparison of preliminary CAD and FEM of aileron rib structure

In Figure 4.19, the CAD model and the FEM model of the 3D printed sections of the Main Section and wingtip are compared. In order to accommodate room for the hinge mechanism, hinge servo actuator, cables, and to reduce weight, the 3D printed part of the Main Section will not be solid. Therefore, this section is modeled as a 2D shell with a thickness of 3 mm. The exact internal structure will depend on the detailed design of these items, but a vertical 2D shell is added to account for more mass in the region of the hinge mechanism and hinge servo actuator. This wall is highlighted in orange in Figure 4.19b. The walls of the main wing and the wingtip are shell elements and have a skin thickness of 3 mm too, based on the previous design[6].

As shown in the top left of Figure 4.19a, the internal structure of the wingtip consists of solid ribs and a spar at the quarter chord. Both have been modeled with 2D elements. The ribs have a thickness of 5 mm, equal to the ribs in the main wing. The wingtip spar has a thickness of 10 mm. Inside of the the 3D printed part of the main wing, two concentrated masses are located. One is used to represent the hinge servo actuator, with an estimated weight of 35 grams. The other is used to represent an accelerometer of 5 grams. A second

accelerometer is put close to the leading edge of the tip of the wingtip.
At the wingtip, the last rib with 10 mm thickness is modeled with 2D elements.

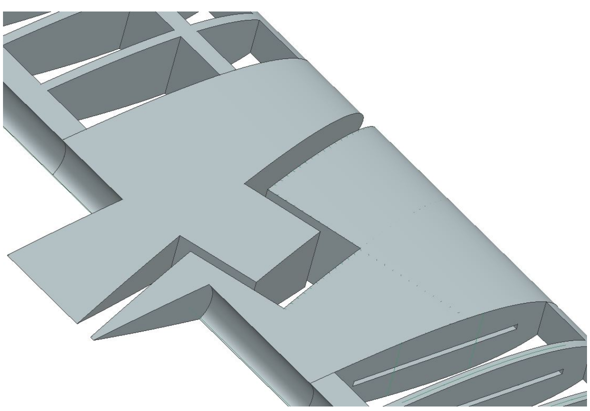

(a) Preliminary CAD of 3D printed Main Section and wingtip

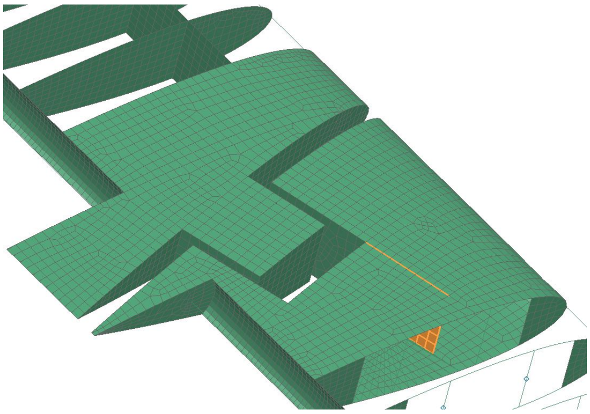

(b) Preliminary FEM of 3D printed Main Section and wingtip

Figure 4.19: Comparison of preliminary CAD and FEM of 3D printed Main Section and wingtip

The FEM representation of the hinge mechanism is compared to the 3D CAD model in Figure 4.20. Figure 4.20b is zoomed in with respect to Figure 4.20a, and the 3D skin of the wingtip is hidden to properly display the hinge connection. Inspired by the work of Carrillo et al. [6], in both the wingtip wall and the main wing wall, a hole is located. This hole represents the actual hole through which the hinge axle will pass. The center of both holes is connected to their respective edge with an RBE2 connection. Secondly, a CBUSH is used to connect the center of both holes to each other, representing a spring-damper system. By setting the rotational stiffness around the axle very low, the FEM analysis will behave as if the hinge is unlocked. And vice versa, by setting the rotational stiffness around the axle relatively high, a locked hinge condition will be simulated. The selection of the hinge stiffness will be further discussed later in this section.

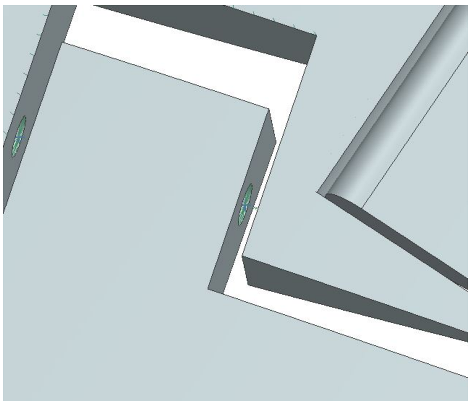

(a) Preliminary CAD of hinge mechanism

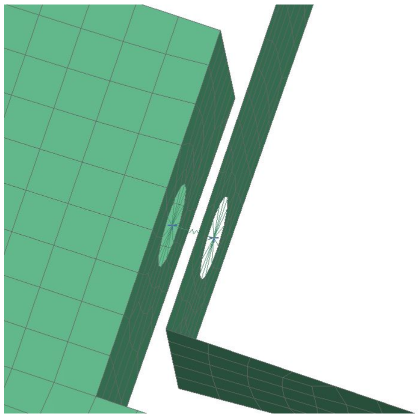

(b) Preliminary FEM of hinge mechanism

Figure 4.20: Comparison of preliminary CAD and FEM of hinge mechanism

In Figure 4.22, the 2D shell elements marked in orange represent the Oracover skin of the wing. The skin has a thickness of 25μm. The density of the Oracover skin is set at 0 [g/cm^3], as it does not have a significant contribution to the overall mass. One can see that a region of the trailing edge of the main wing is not highlighted. In the preliminary design, this region was modeled as a 3D printed skin, instead of continuing the rib structure.

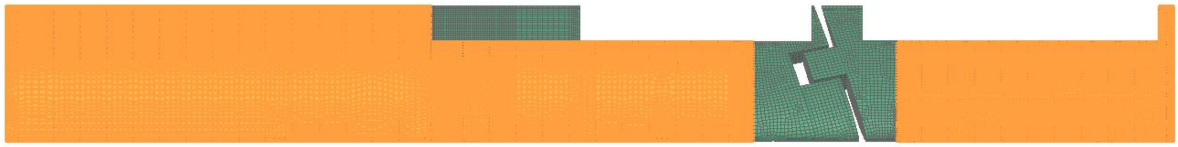

Figure 4.21: 2D FEM elements representing the Oracover skin

The spar, designed as an aluminium plate, is modeled with 2D shell elements, and it's thickness can be varied to achieve the desired stiffness. A more elaborate explanation on the spar sizing is presented in Section 4.3.

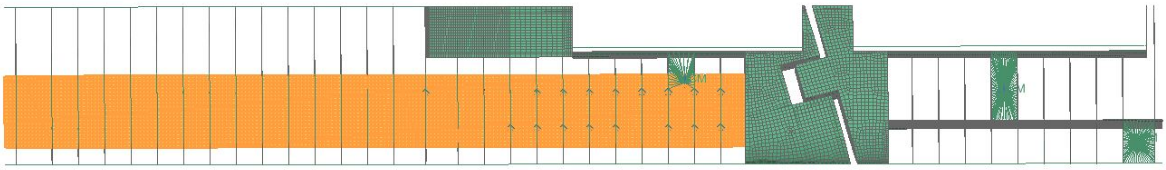

Figure 4.22: 2D FEM elements representing the spar

The material properties used in the FEM model are presented in Table 4.1 below:

Table 4.1: Properties of Selected Materials

Material	**Density [g/cm^3]**	**Young's Modulus [MPa]**
Aluminium 2014	2.794	73119
Nylon PA12	0.93	1700
Oracover	0	4666

This concludes the structural model of the preliminary design. By performing a modal analysis (NX Nastran SOL103) of the FEM model in Siemens Simcenter, the first 10 structural modes of the demonstrator are computed. In requirement *Req-6*, it is stated that the aileron shall have a large enough angular velocity to achieve a deflection frequency that exceeds the wing's second bending mode. The first two bending frequencies are noted as f_1 [Hz] and f_2 [Hz]. In order to have an aileron motion that can, at least, follow the second bending mode, the deflection of the aileron is by a simple sine function in Equation (4.18). With a maximum deflection δ_{max} put at 20°.

$$\delta(t) = \delta_{max} \sin(2\pi f_2 \cdot t) \tag{4.18}$$

By taking the derivative of Equation (4.18), the angular ([deg/sec]) velocity of the aileron is found in Equation (4.19):

$$\omega_{aileron} = 2\pi f_2 \delta_{max} \cos((2\pi f_2 \cdot t) \tag{4.19}$$

By maximizing Equation (4.19), the minimum required angular velocity $\omega^{req}_{aileron}$ [deg/sec] that the servo actuator can provide to the aileron is found in Equation (4.20):

$$\omega^{req}_{aileron} = 2\pi f_2 \delta_{max} \tag{4.20}$$

Before this can be translate to the required rotational speed of the servo actuator, the ratio of arms with which the servo actuator (r_s) and the aileron (r_a) are connected must be taken into account, which are illustrated in Figure 4.23:

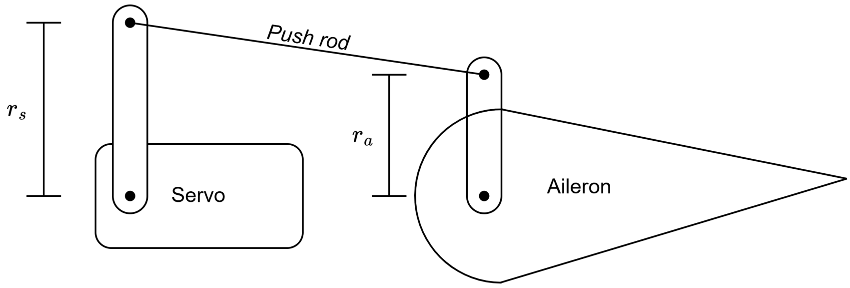

Figure 4.23: Illustration of servo actuator arm and aileron arm

By taking into account the ratio of arms, and converting the unit to [sec/60°], the required servo actuator speed (ω_s) is found in Equation (4.21). Due to the change in unit, ω_s represents the maximum allowable time the servo actuator has to travel 60 degrees.

$$\omega_s = \frac{60}{\omega_{aileron}^{req}} \frac{r_a}{r_s} \tag{4.21}$$

Equation (4.21) is used to evaluate which servo actuators meet Requirement *Req-5*. In order to asses if servo actuators satisfy Requirement *Req-8*, the required torque delivered by the servo actuator must be computed. Three main components are identified and drawn in Figure 4.24. The first component is the aerodynamic hinge moment, M_{aero}. This moment will have an opposite direction to that of the aileron deflection, δ. Secondly, the servo actuator exert a moment on the aileron, denoted as M_{servo}. At last, the moment due to inertia, denoted by the product of the aileron moment of inertia I_a and the aileron angular acceleration $\dot{\omega}_{aileron}$, is displayed.

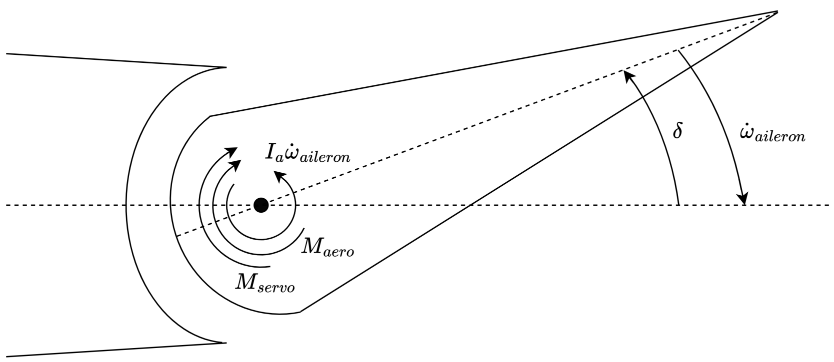

Figure 4.24: Moment contributions on aileron in motion

To asses the required torque of the servo actuator, the maximum torque on the aileron must be analyzed. However, due to the design of the aileron, the inertia of the aileron is assumed to be relatively small. Therefore, to asses the most critical case, the static case with a fully deflected aileron ($\pm\delta_{max}$) is used to find the required aileron torque. Secondly, the loading on the aileron is highest at the highest angle of attack $\alpha_{n=2.5}$. Figure 4.25 represents the critical condition at which requirement *Req-8* is assessed. It must be noted that both Figure 4.24 and Figure 4.25 merely serve as a system illustration, and do not represent the actual design of the aileron mechanism.

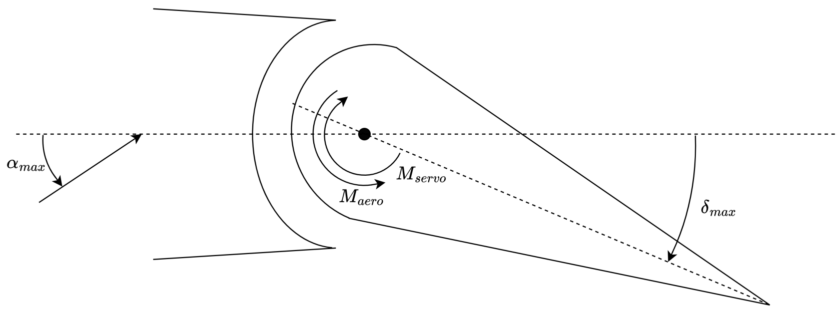

Figure 4.25: Moment contributions on aileron in static condition

In order to analyze the loading on the aileron, the hinge moment coefficient is retrieved from AVL. Although using AVL to estimate performance can lead to an over prediction, using AVL to estimate the loads can lead to a conservative approach. Since the aim is not to size the aileron servo actuator to be at its maximum performance at the critical sizing condition, an overestimation of the loads provides an additional safety margin in the servo actuator sizing. Once the hinge moment coefficients (C_m) are retrieved for both ailerons, this is transformed to the aerodynamic hinge moment in Equation (4.22) , which equals the required servo actuator torque M^{Nm}_{servo} in [Nm].

$$M^{Nm}_{servo} = \frac{1}{2}\rho V^2 S_{ref} C_{ref} C_m \tag{4.22}$$

As mentioned earlier, the common unit to express servo actuator torque is [kg · cm]. Secondly, the ratio between r_s and r_a must be taken into account. Equation (4.23) converts the units from [Nm] to [kg · cm] and takes into account the ratio of servo actuator and aileron arm:

$$M^{kgcm}_{servo} = M^{Nm}_{servo}\frac{100}{9.81}\frac{r_s}{r_a} \tag{4.23}$$

This concludes the servo actuator sizing procedure of the ailerons. A servo actuator than can satisfy both the required rotational speed ω_s and the required torque $M_{servo_{kgcm}}$ is selected for the actuation of the ailerons. If, for example, the servo actuator speed appears to be for more critical than the servo actuator torque, the ratio between r_s and r_a can be varied accordingly.

Sizing Results Aileron Servo Actuator

In order to select a proper hinge stiffness, a sensitivity analysis on the bending modes with respect to the hinge stiffness is performed. On the horizontal axis o fFigure 4.26, a logarithmic scale is used to increase the hinge stiffness. On the vertical axis, the bending frequency is shown. At a relatively low hinge stiffness, it can be observed that the bending frequencies start relatively low at 0.73 Hz and 2.1 Hz, and increases for an increase in hinge stiffness. Then, above a hinge stiffness of 10^6 N/mm, the bending frequency becomes constant (0.82 Hz and 5.87 Hz) for an increase in bending frequency until the hinge stiffness reaches a value of $10^1 1$ N/mm. After this point, both bending frequencies jump to a higher level. This indicates a numerical instability of the model, due to which the bending frequencies would be heavily over-predicted. The middle region of the graph, at which the bending modes are constant, represents the locked hinge condition.

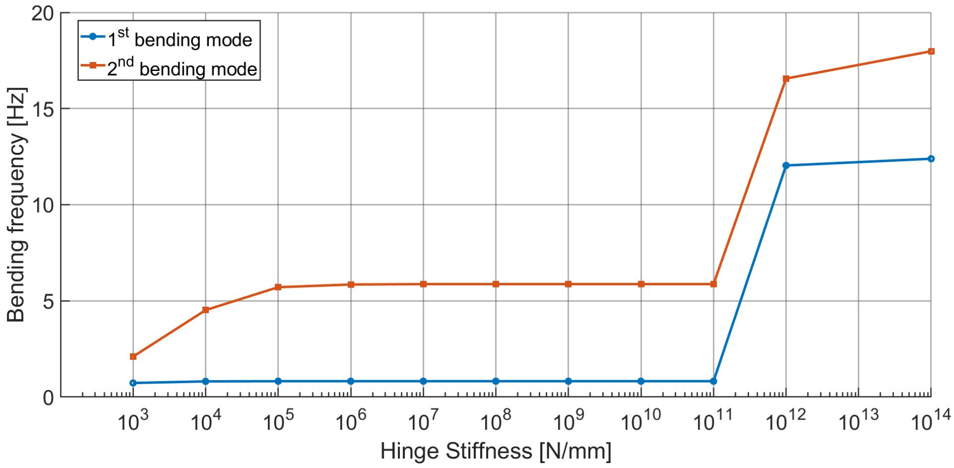

Figure 4.26: Sensitivity analysis of bending mode frequencies vs. hinge stiffness

Using the results of Figure 4.26, a hinge stiffness of 10^8 N/mm is chosen for the locked hinge condition. A modal analysis has been performed for an aluminium plate with a width of 100 mm. A sweep has been performed for a range of plate thicknesses between 1 mm and 5 mm.

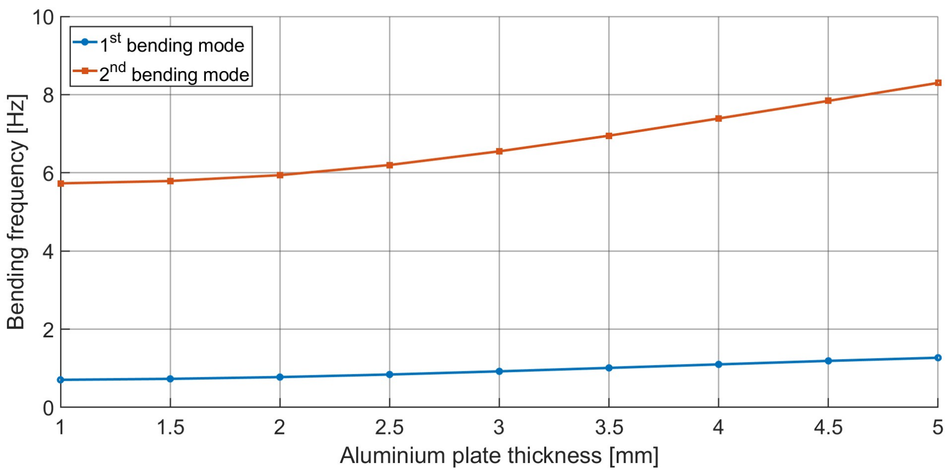

Figure 4.27: The effect of plate thickness on the 1^{st} and 2^{nd} bending mode

To allow the wing spar to have a plate thickness in the range described above, and to be able to control the wing for this range, the results in Figure 4.27 show that the required deflection frequency of the aileron is 8.3 Hz. By applying Equation (4.20) and Equation (4.21), this translate to a maximum required angular servo actuator speed of 0.058 sec/60° for a ratio $\frac{r_a}{r_s} = \frac{1}{1}$.
Secondly, the hinge moment coefficients are computed. By applying Equation (4.22) and Equation (4.23), the resulting aerodynamic moment on the aileron hinge line is found for both the inboard aileron and the outboard aileron. For both ailerons, the moments are computed for a ±20° deflection and the results listed in Table 4.2. For a ratio of $\frac{r_a}{r_s} = \frac{1}{1}$, this corresponds to the required servo actuator torque.

Aileron Deflection	**Inboard Aileron Hinge Moment [kg · cm]**	**Outboard Aileron Hinge Moment [kg · cm]**
20°	-1.24	-1.27
-20°	0.891	1.01

Table 4.2: Hinge moments for varying aileron deflections

This provides both the required angular velocity and the required torque that the servo actuator should provide for a ratio of $\frac{r_a}{r_s} = \frac{1}{1}$. However, a change in this ratio could result in a smaller required servo actuator. After a wide review, the Blue Bird BMS-A10V[1] and BMS-A12V[2] are compared. In Table 4.3, the specifications of both servo actuators is shown.

Table 4.3: Torque and speed for different servo actuators at varying voltages.

Servo Actuator Model	Voltage	Torque [kg · cm]	Speed [sec/60°]
BMS-A10V	3.7V	1.6	0.15
	6.0V	2.4	0.1
	8.4V	3.2	0.07
BMS-A12V	3.7V	2.3	0.19
	6.0V	3.7	0.12
	8.4V	4.6	0.09

As can be seen in Equation (4.21) and Equation (4.23), decreasing the ratio of $\frac{r_a}{r_s} = \frac{1}{1}$ has a negative on the torque delivered to the aileron, but a positive impact to the delivered rotational speed. By comparing the minimum required speed of 0.058sec/60° and the minimum required torque of 1.27 kg · cm with the performance listed in Table 4.3, it can be observed that the servo actuator speed is dominating the servo actuator sizing. Although both servo actuators are not capable of delivering sufficient torque to the ailerons, the ratio $\frac{r_a}{r_s}$ can be reduced. This will increase the rotational speed of the aileron, but will decrease the torque provided to the aileron. In Table 4.4 (BMS-A10V) and Table 4.5 (BMS-A12V), $\frac{r_a}{r_s}$ is reduced while checking the torque and speed provided to the aileron for different voltages. Cells marked in green correspond to a satisfied the requirement, while cells marked in red do not meet the requirement.

Table 4.4: BMS-A10V Servo Actuator - Aileron torque and speed for varying $\frac{r_a}{r_s}$ at different voltages.

	$\frac{r_a}{r_s}$	**1**	**0.95**	**0.9**	**0.85**	**0.8**	**0.75**	**0.7**	**0.65**	**0.6**	**0.55**	**0.5**
3.7V	**Torque**	1.6	1.52	1.44	1.36	1.28	1.2	1.12	1.04	0.96	0.88	0.8
	Speed	0.15	0.143	0.135	0.128	0.12	0.113	0.105	0.098	0.09	0.083	0.075
6V	**Torque**	2.4	2.28	2.16	2.04	1.92	1.8	1.68	1.56	1.44	1.32	1.2
	Speed	0.1	0.095	0.09	0.085	0.08	0.075	0.07	0.065	0.06	0.055	0.05
8.4V	**Torque**	3.2	3.04	2.88	2.72	2.56	2.4	2.24	2.08	1.92	1.76	1.6
	Speed	0.07	0.067	0.063	0.06	0.056	0.053	0.049	0.046	0.042	0.039	0.035

Table 4.5: BMS-A12V Servo Actuator - aileron torque and speed for varying $\frac{r_a}{r_s}$ at different voltages.

	$\frac{r_a}{r_s}$	**1**	**0.95**	**0.9**	**0.85**	**0.8**	**0.75**	**0.7**	**0.65**	**0.6**	**0.55**	**0.5**
3.7V	**Torque**	2.3	2.19	2.07	1.96	1.84	1.73	1.61	1.50	1.38	1.27	1.15
	Speed	0.19	0.181	0.171	0.162	0.152	0.143	0.133	0.124	0.114	0.105	0.095
6V	**Torque**	3.7	3.52	3.33	3.15	2.96	2.78	2.59	2.41	2.22	2.04	1.85
	Speed	0.12	0.114	0.108	0.102	0.096	0.09	0.084	0.078	0.072	0.066	0.06
8.4V	**Torque**	4.6	4.37	4.14	3.91	3.68	3.45	3.22	2.99	2.76	2.53	2.3
	Speed	0.09	0.086	0.081	0.077	0.072	0.068	0.063	0.059	0.054	0.050	0.045

It shows that, although the BMS-A12V servo actuator has higher torque performance, it underperforms on the speed requirement, compared to the BMS-A10V. Table 4.4 and Table 4.5 show that the BMS-A10V requires less reduction in $\frac{r_a}{r_s}$ to satisfy both requirements. Since the reduction in aileron arm is limited by the thickness of the aileron at the hinge line, and the servo actuator arm has a certain maximum length, keeping $\frac{r_a}{r_s}$ as large as possible is desired. Therefore, the Blue Bird BMS-A10V is selected with $\frac{r_a}{r_s} = 0.8$. Blue Bird offers the same servo actuators, but with different orientations of the flanges, as can be seen in Figure 4.28. The BMS-A10V is

[1] See "Micro," Blue Bird, https://www.blue-bird-model.com/products_detail/74.htm.
[2] See "Micro," Blue Bird, https://www.blue-bird-model.com/products_detail/539.htm.

selected for it's flanges that are parallel with the mid-plane of the wing, which allows for fastening the servo to the structure with screws.

(a) BMS-A10H (b) BMS-A10S (c) BMS-A10V

Figure 4.28: Comparison of Blue Bird servo actuator models: BMS-A10H, BMS-A10S, and BMS-A10V.

The result of the aileron servo actuator sizing procedure are summarized in Table 4.9.

4.2.2. HINGE SERVO ACTUATOR: SIZING PROCEDURE AND RESULTS

This section will explain the methodology behind the hinge servo actuator sizing. The purpose of the hinge servo actuator is to be able to lock the hinge in all flight conditions, as stated in *Req-7*. Secondly, the hinge should be able to quickly release the hinge. In order to perform the hinge servo actuator sizing, first, the hinge locking mechanism is explained.

The main hinge mechanism consists of six parts, displayed and annotated in the assembly in Figure 4.29. To create a clear overview, the main wing and other parts not related to the hinge mechanism are hidden.

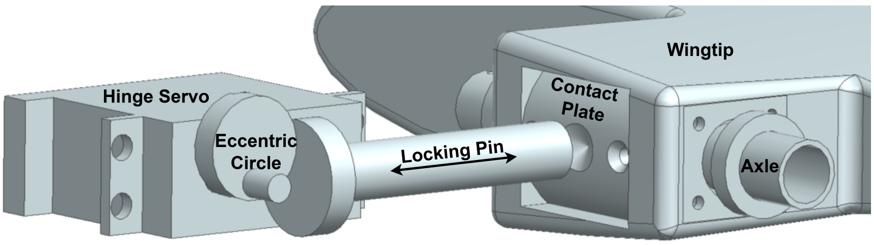

Figure 4.29: CAD assembly of the hinge mechanism and wingtip

To select the appropriate servo actuator, it is necessary to estimate the required torque, which involves two primary steps: first, calculating the normal force at the pin required to lock the hinge, and second, translating this normal force into the corresponding torque on the servo actuator. As shown in Figure 4.29, a hole is drilled at the contact point between the pin and the contact plate. Experience shows that while reducing the hole angle can decrease the required torque for the hinge servo actuator, it also increases the risk of jamming the locking pin and delays the release time. An overview of the forces and moments acting on the hinge mechanism is provided in Figure 4.30. Since the contact plate and pin are symmetrical around the horizontal plane, only the top half is illustrated for clarity.

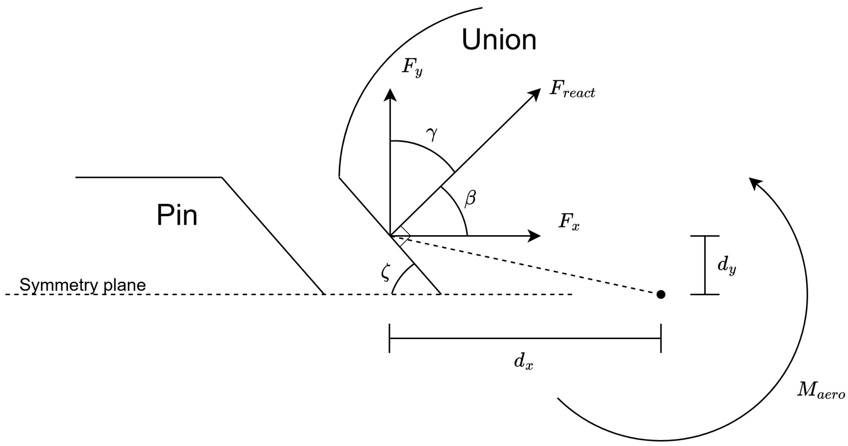

Figure 4.30: Locking forces in pin - contact plate mechanism

The reaction force that would keep the wingtip in horizontal position is drawn. On the other hand, the same force in opposite direction acts on the pin. By computing the value of F_{react} at which the wingtip is in equilibrium, the normal force in the pin can be found, equal to F_x. Some important simplifications are made in this analysis. First, the weight of the wingtip is neglected. Since the weight will relieve the aerodynamic moment M_{aero}, this simplification will make the results more conservative. However, this approach considers a static analysis. A dynamic analysis could result in a more heavily loaded pin. Thirdly, only the normal contact force between the pin and the contact plate is considered, neglecting friction. Friction could help locking the mechanism, and thus reduce F_{react}, making the approach more conservative. At last, the reaction force is modeled as a point force, and not a distributed force.

In order to find the reaction force, the moment equilibrium in Figure 4.30 must be found. Three aspects must be known in order to compute this equilibrium: The aerodynamic moment of the wingtip acting on the hinge (M_{aero}), secondly, the reaction force is decomposed into it's vertical and horizontal component, F_y and F_x, respectively. To compute these components, the angles γ and β must be known. The angles can be found by the geometric relation between them, and the angle of the hole in the contact plate (2ζ). To prevent jamming the hinge mechanish and delaying the release time, a hole depth of 3 mm and a hole angle of $\zeta = 60°$ are selected. Since F_{react} acts perpendicular to the side of the hole, β and γ are found in Equation (4.24):

$$\beta = 90 - \zeta \qquad\qquad \gamma = 90 - \beta = \zeta \tag{4.24}$$

Resulting in the components:

$$F_x = F_{react}\sin(\zeta) \qquad\qquad F_y = F_{react}\cos(\zeta) \tag{4.25}$$

Since F_x, is the component of interest, since this will be opposed by the normal force in the pin, Equation (4.25) can be rewritten to Equation (4.26)

$$F_{react} = \frac{F_x}{\sin(\zeta)} \qquad\qquad F_y = \frac{F_x}{\tan(\zeta)} \tag{4.26}$$

By knowing the outer radius of the contact plate is 15 mm, the hole depth is 3 mm, and the hole angle is 120°, the moment arm of the vertical and horizontal components can easily be found in Equation (4.27):

$$d_x = 15 - \frac{3}{2} \qquad\qquad d_y = \frac{3}{2}\tan(\zeta) \tag{4.27}$$

Combining Equation (4.24) and Equation (4.25) allows for a moment calculation around the center of rotation, as shown in Equation (4.28):

$$\sum M : F_y d_x + F_x d_y - M_{aero} = 0 \tag{4.28}$$

By using Equation (4.26), the moment equation can be used to find F_x:

$$F_x = \frac{M_{aero}}{\left(\frac{d_x}{\tan(\zeta)} + d_y\right)} \tag{4.29}$$

Now that the normal force in the pin can be calculated, this must be transformed to a required torque of the servo actuator. As can be seen in Figure 4.29, the servo actuator is connected to a eccentric circle (2). In Figure 4.31a, the two shapes that have been considered during the design of the eccentric circle are shown: a perfect circle (solid line) and an ellipse (dashed line). The center of rotation is indicated by the solid dot. For the eccentric circle, the difference between r_2 and r_1 is equal to the maximum pin displacement. In the hinge mechanism, 12 mm of pin displacement is required to achieve full clearance between the pin and the rotating wingtip. Due to the dimensions of the servo actuator axle, r_2 has a minimum value of 3 mm. To achieve the minimum pin displacement, r_1 is set at 15 mm. As can be seen in Figure 4.31b, the horizontal distance c_x from the center of rotation of the eccentric circle to the point of contact between the pin and the eccentric circle determines the horizontal position of the pin. The vertical distance c_y between the center of rotation and the point of contact is the moment arm at which F_x acts. The angle of rotation of the eccentric circle and ellipse are noted as η. In theory, F_x would only act on the pin if the pin is in it's furthers position and has contact with the contact plate. However, since the locking mechanism is a crucial part of the design, a conservative approach is used to asses the required torque of the servo actuator.

The conservative approach assumes that F_x, calculated in Equation (4.29), constantly acts on the eccentric circle and ellipse, throughout a range of $0° \leq \eta \leq 180°$. Since the point of contact is changing throughout the range of η, finding it's position is not trivial. Therefore, a geometric study using the CAD model is performed to find the relation between η, c_y, and c_x for both shapes. For each point, the vertical distance c_y is multiplied with F_x to find the torque acting on the servo actuator. The peak torque value found in this analysis corresponds to the sizing torque of the servo actuator. The results of the hinge servo actuator sizing procedure is discussed in Section 4.2.2.

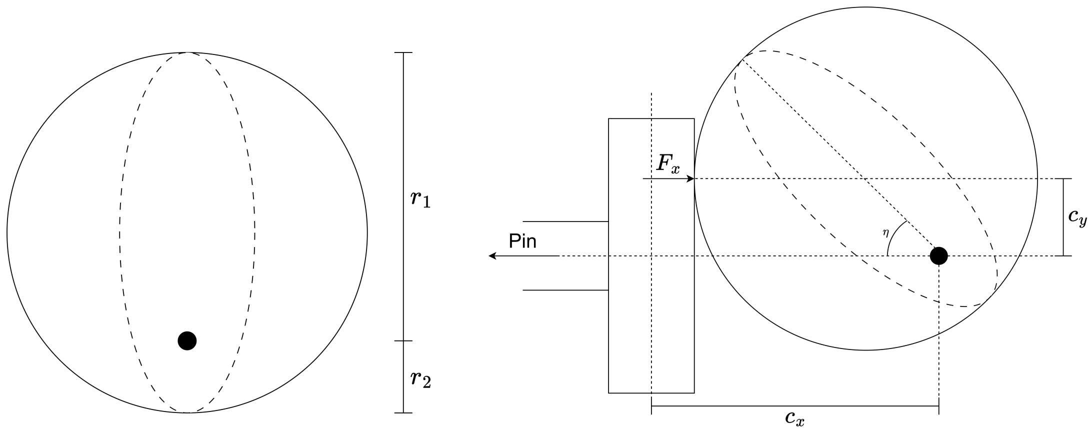

(a) Eccentric circle sizing

(b) Eccentric circle - pin contact

Figure 4.31: Comparison of eccentric circle and ellipse and the point of contact with the hinge locking pin

SIZING RESULTS HINGE SERVO ACTUATOR

This section presents the results of the sizing procedure of the hinge servo actuator, as described in Section 4.2.2. In order to size the servo actuator, the torque on the servo actuator must be computed. In AVL, the lift distribution over the wingtip is integrated to find a conservative aerodynamic moment (M_{aero}). By having an aerodynamic wingtip moment around the hinge of $M_{aero} = 6.07$ Nm, and having a hole angle $2\zeta = 120°$, the resulting normal force in the pin is found with Equation (4.29): $F_x = 587$ N.

After performing a geometric study for $0° \leq \eta \leq 180°$ using the CAD model of the locking pin and the eccentric circle or ellipse with $r_1 = 15$ mm and $r_2 = 3$ mm, the normal force is multiplied by the vertical distance from the point of contact with the locking pin and the rotational axis of the servo actuator (c_y) to find the required servo actuator torque.

Figure 4.32 compares how the required servo torque varies with the horizontal pin displacement for both an eccentric circle and an ellipse. At a horizontal pin displacement of 0 mm, the pin is fully locked. In this case, the point of contact is perfectly in line with the servo actuator shaft, and thus requires no torque.

In Figure 4.33, the required aileron torque for a rotation angle η is shown. By comparing Figure 4.32 and Figure 4.33, a couple of observations can be made: First, the ellipse causes the required torque to increase more rapidly after unlocking the hinge than that an eccentric circle does. Secondly, the peak torque required is lowest for the eccentric circle. Since both the more gradual increase in torque, and the lower peak torque required are favorable in the design, the eccentric circle is chosen to transfer the locking pin loads to the servo actuator.
The peak torque required to lock the hinge is with an eccentric circle is 33 kg · cm. For consistency, servo actuators from Blue Bird are considered in the selection process. Between the servo actuator candidates that could satisfy the requirement, availability of the servo actuators had to be taken into account. Taking both the torque requirement and availability into account, the Blue Bird BLS-73A[3] was selected (Figure 4.34). This servo actuator can provide a torque of 43.2 kg · cm at 8.4 V. Since the hinge locking mechanism is an essential part of the design, the excessive torque could allow for some post-manufacturing adjustments if the mechanism would turn out not to behave as predicted.

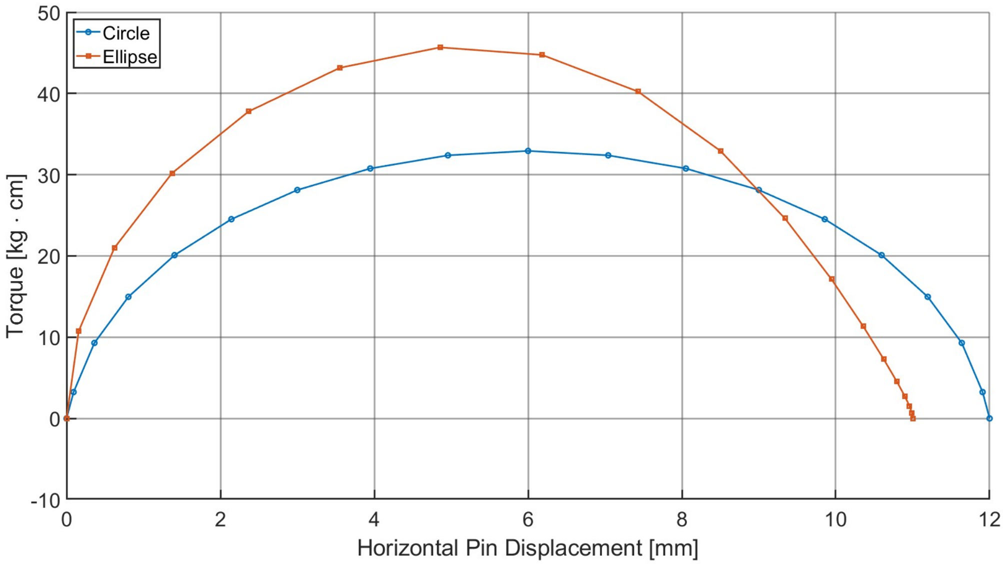

Figure 4.32: Comparison of eccentric circle and ellipse - Servo actuator torque required vs. horizontal pin displacement

[3]See "AIRPLANE Series," Blue Bird, https://www.blue-bird-model.com/products_detail/398.htm.

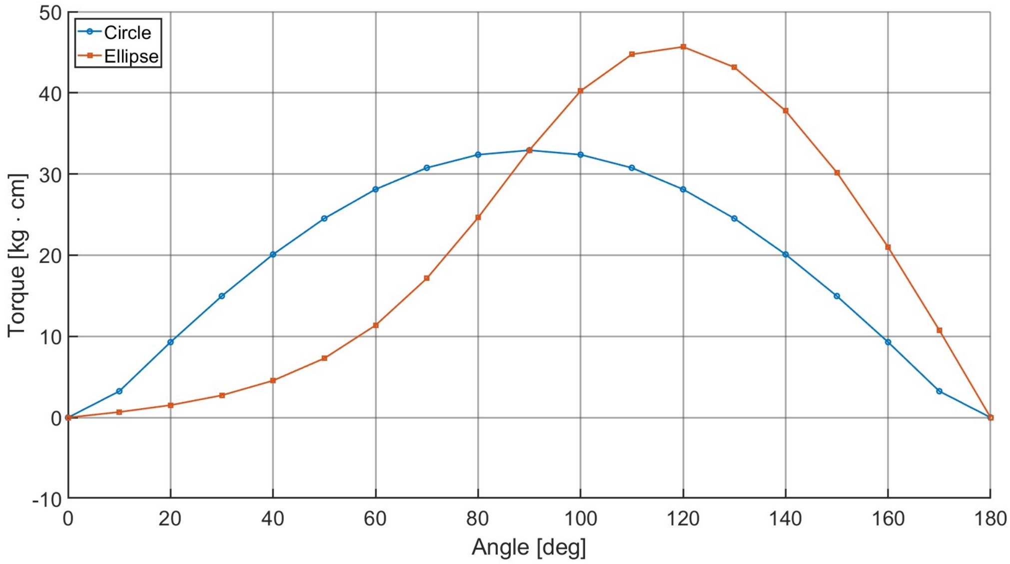

Figure 4.33: Comparison of eccentric circle and ellipse - Servo actuator torque required vs. rotation angle

Figure 4.34: Hinge mechanism servo actuator - Blue Bird BLS-73A

The result of the hinge servo actuator sizing procedure are summarized in table Table 4.10.

4.3. WING SPAR SIZING

In the demonstrator design, the shape is provided by the 3D printed parts, while structural properties of the wing will be determined by the wing spar sizing. The wing spar is designed as an aluminium plate at the center of the wing. By leaving a large cutout of 120 mm x 6 mm in all ribs of the main wing, the aluminium plate and the CAD model of the wing can be performed separately. During assembly, the aluminium plate will slide into the ribs, and lie on the bottom of the cut-out. From the top of the ribs, insert screws are used to provide a proper load transfer between the ribs and the plate for all plate thicknesses. The aim of the plate sizing is to satisfy requirements *Req-3*, *Req-4*, and *Req-5*, which cover the flutter speed, wingtip deflection, and divergence speed requirements.
Section 4.3.1 covers the procedure regarding updating the FEM model after the detailed CAD design, after which Section 4.3.2 will continue by introducing the sizing procedure of the wing spar sizing, after which the results of the sizing procedure are presented.

4.3.1. FEM FOR WING SPAR SIZING

In order to achieve the most accurate FEM model for the aeroelastic simulations, the plate sizing is performed after the detailed design was finished. Since transitioning from the preliminary design to the detailed design involved many iterations, a new FEM model was created for the detailed design, instead of updating the FEM model of the preliminary design. Although the detailed design will be discussed in Chapter 5, the most significant updates from the preliminary FEM model will be shown below.

By comparing the detailed rib structure of Figure 4.35a with the preliminary structure in Figure 4.17a, some significant changes have been made.The aft part of the rib has been hollowed, with the aim of reducing weight and manufacturing cost. This slender rib structure can be modeled more efficiently with a 1D beam element, than the 2D shell elements in the preliminary design. Similarly for the region of the rib near the leading edge, since the rib cut-out has been enlarged in the detailed design, the front section of the rib is also modeled as a 1D beam element. By going from the preliminary design to the detailed design, the FEM model of the main rib structure changed from consisting of mainly 2D shell elements (Figure 4.17b), to only consisting of 1D beam elements (Figure 4.35b).

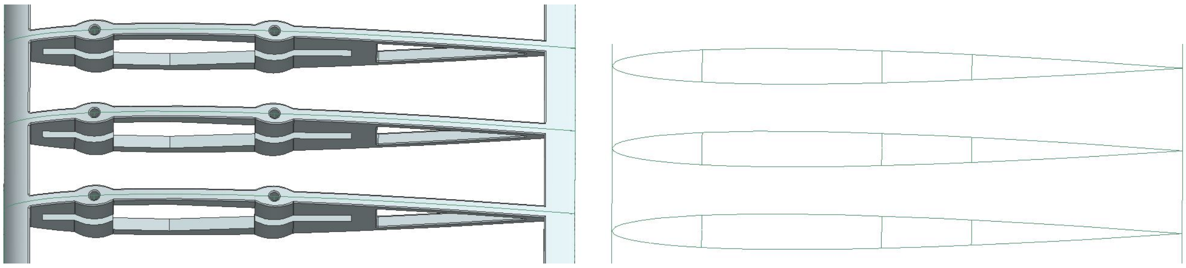

(a) Detailed CAD of main rib structure

(b) Updated FEM of main rib structure

Figure 4.35: Comparison of detailed CAD and FEM of main rib structure

In Figure 4.36, the rib structure at the aileron is compared. The rib structure of Figure 4.36b is very similar to that of Figure 4.35b, except for the rear spar that is introduced in the aileron cut-out. In the detailed design phase, the aileron is connected to two supports, equally spaced over the rear spar. The support is modeled with 2D shell elements. The aileron is connected to the aileron support with a RBE2 connection. In Figure 4.36a, the support of the aileron servo actuator can be seen between two ribs. The servo actuator support including the aileron servo actuator is modeled as a point mass, and is attached to the connecting ribs.

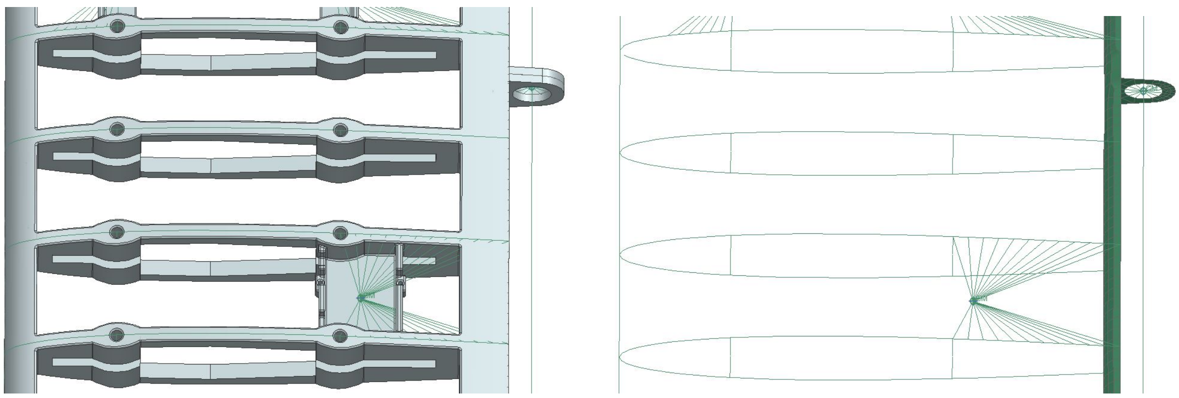

(a) Detailed CAD of aileron rib structure

(b) Updated FEM of aileron rib structure

Figure 4.36: Comparison of detailed CAD and FEM of aileron rib structure

In Figure 4.37, the 3D printed part of the main wing and wingtip are compared to the FEM model. The 3D printed part is modeled as 2D shell elements, similarly to the preliminary FEM model. In the detailed design, the exact locations of components are known, and are represented by point masses in the FEM model. The mass of the FEM elements is compared to the predicted mass of the CAD model of that specific area. The thickness of the 2D shell elements is adjusted such that the mass is matched to the 3D CAD model.

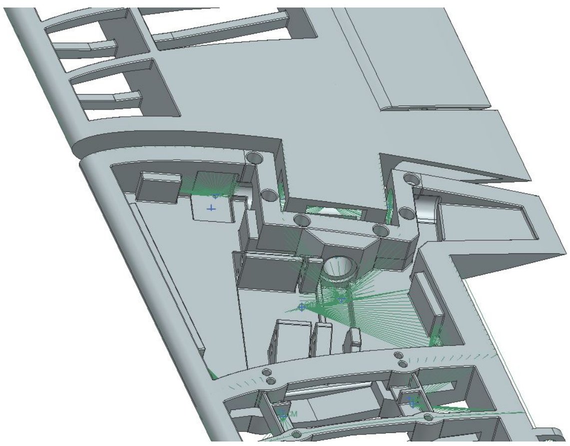

(a) Detailed CAD of 3D printed Main Section and wingtip

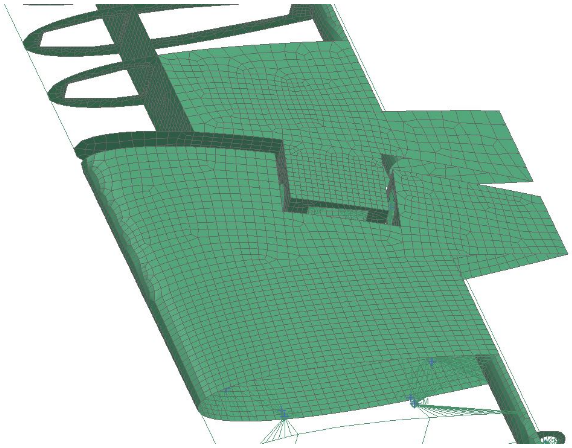

(b) Updated FEM of 3D printed Main Section and wingtip

Figure 4.37: Comparison of Detailed CAD and FEM of 3D printed Main Section and wingtip

The FEM representation of the hinge mechanism is compared to the 3D CAD model in Figure 4.38. Figure 4.38b is zoomed in with respect to Figure 4.38a, Although the geometry of the hinge mechanism changed significantly with respect to the preliminary design, the FEM representation of the hinge in the detailed design is copied from the preliminary design.

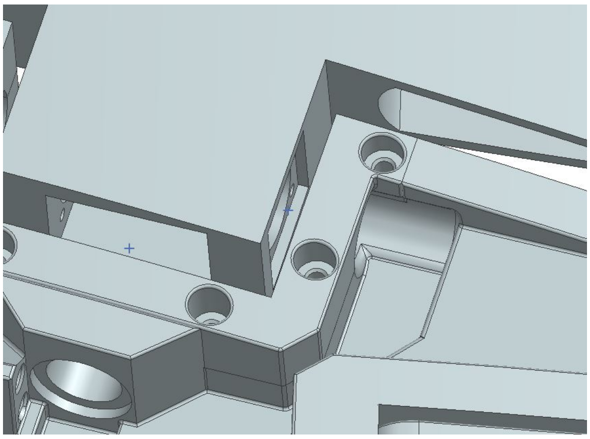

(a) Detailed CAD of hinge mechanism

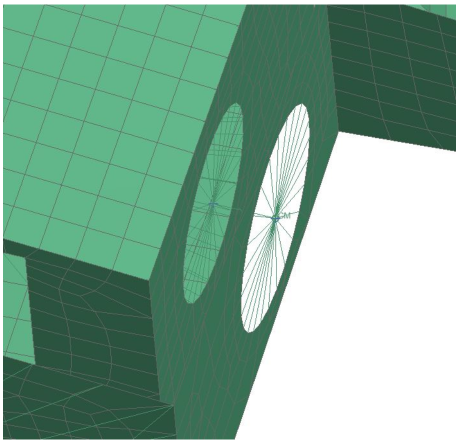

(b) Updated FEM of hinge mechanism

Figure 4.38: Comparison of Detailed CAD and FEM of hinge mechanism

In Figure 4.39, the detailed design of the wingtip is compared to the updated FEM model. Similarly to Figure 4.36b, the aileron is connected to the trailing edge spar at two equally distributed points. The main spar of the wingtip is the same at the spar in the preliminary design, and is modeled as 2D elements. A major difference between the preliminary design and the detailed design is the rib structure. In the preliminary design, the ribs were solid. However, for weight savings and to allow cables to pass through, the ribs have been hollowed. This change has been implemented later on in the design phase, before which the ribs were modeled as 2D elements. Although the rib elements are quite slender, and could easily be modeled as 1D beams, the 2D modeling is kept for simplicity. Within the wingtip, the aileron servo actuator mount and two accelerometer mounts at the tip are located. These are represented by point masses and are connected to the nearest ribs.

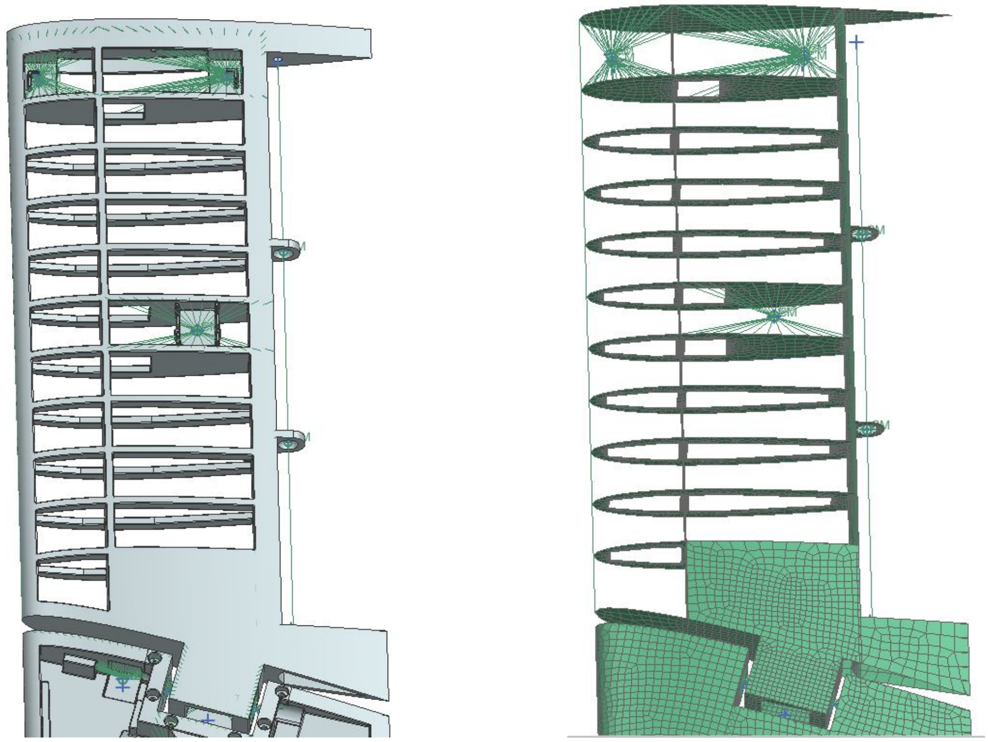

(a) Detailed CAD of 3D wingtip structure

(b) Updated FEM of 3D wingtip structure

Figure 4.39: Comparison of Detailed CAD and FEM of 3D printed Main Section and wingtip

4.3.2. SIZING PROCEDURE AND RESULTS OF WING SPAR SIZING

Three degrees of freedom exist in the plate sizing: the thickness, width and chordwise position of the plate. If the width of the plate is less than the 120 mm cut-out, the position of the plate in chordwise direction can be varied within the cut-out. The length of the plate is fixed at 995 mm, which is the length from the root until the cutout in the main wing where the hinge mechanism is located. The maximum thickness of the plate is limited by the cutout in the ribs, which is set at 6 mm. The maximum width is 120 mm, corresponding to the width of the cutout in the ribs. The plate is laid on the bottom of the cutout, and insert screws from the top of the rib will ensure a proper and even load transfer from the plate to the ribs. Using insert screws also allow for possible future modifications to the plate, which make the demonstrator more versatile and more suitable for future research.

Flutter analysis can be conducted under both locked hinge and free hinge conditions. Previous research indicates that flutter occurs at significantly lower speeds in free hinge conditions compared to locked hinge conditions. To ensure that free hinge flutter behavior can be studied within the wind tunnel's operating range, the free hinge condition is used as the primary sizing requirement.

From the aeroelastic simulations, frequency and damping plots are analyzed to identify flutter behavior. In the damping plot, flutter occurs at the velocity where the damping of a mode transitions from negative to positive. The frequency plot provides insight into which modes interact in this flutter mechanism. As velocity increases, two modes move closer together and begin interacting. At the flutter speed, the damping of one of these modes reaches zero. Beyond this point, further velocity increases lead to positive damping, causing the wing to extract energy from the airflow, resulting in growing oscillations. By determining the flutter speed and understanding the underlying mechanism, appropriate plate sizing can be performed to mitigate flutter risks.

Secondly, the static wingtip deflection is computed. Modern wings tend to get increasingly flexible, introducing larger tip deflections in flight. One of the results of larger deflections is a system that behaves in a more non-linear way. In order to mimic this behavior, the aim of the demonstrator is to have a relatively high tip deflection between 15% – 20% of the demonstrator span. The wingtip deflection is computed in a locked hinge conditions, since this represent the normal flight condition. The wingtip deflection in static free hinge condition would always result in a relatively high deflection, and thus does not represent the flexibility of the wing. Depending on the results of the flutter analysis, an attempt is made to satisfy the flutter requirement and having high tip deflections. At last, caution is paid to the occurrence of divergence. Since divergence would be catastrophic, this cannot occur anywhere near the test range.

The results of the plate sizing procedure are presented below. Two different simulations are performed in order to size the plate. A flutter analysis is performed to find the flutter speed for given plate dimensions and at free hinge condition. Secondly, a static wingtip deflection is computed in locked hinge conditions. The static deflection analysis is performed at the maximum velocity (V_{max}) and at the maximum angle of attack ($\alpha_{n=2.5}$).

FLUTTER ANALYSIS

The flutter analysis is performed for plate thicknesses of 3.2 mm, 5 mm and 6 mm, these plates are standard aluminium plate thicknesses and are available in-house. First, the frequency and damping plots for the first 10 modes are computed.
To properly understand the flutter mechanisms, the mode shapes are presented in Figure 4.40. All modes correspond to the free hinge condition. The blocks inside the wing correspond to concentrated masses. In Figure 4.40c and Figure 4.40d, some unexpectedly large deflections are observed on the wing surface. These correspond to highly localized modes and do not significantly impact the overall wing behavior, so they are not considered in the analysis. As can be seen in Figure 4.40a, mode 2 corresponds to a rigid-body mode, and will be called the flapping mode. Mode 2 could be compared to the first bending mode of the wing in combination with a flapping motion, and mode 3 could be compared to the second bending mode. Mode 4 corresponds to the first torsional mode.
Now that the first four modes are identified, the flutter analysis can proceed. From initial simulations, it became evident that aluminium plate required a large thickness to satisfy the flutter speed requirement. Therefore, the maximum width of the plate is utilized. In order to have some margin between the 120 mm wide cut-out in the 3D printed ribs and the aluminium plate, the width of the plate is set at 119 mm for all future simulations. Figure 4.41 presents the frequency plot of the first four modes with a plate thickness of 3.2 mm.

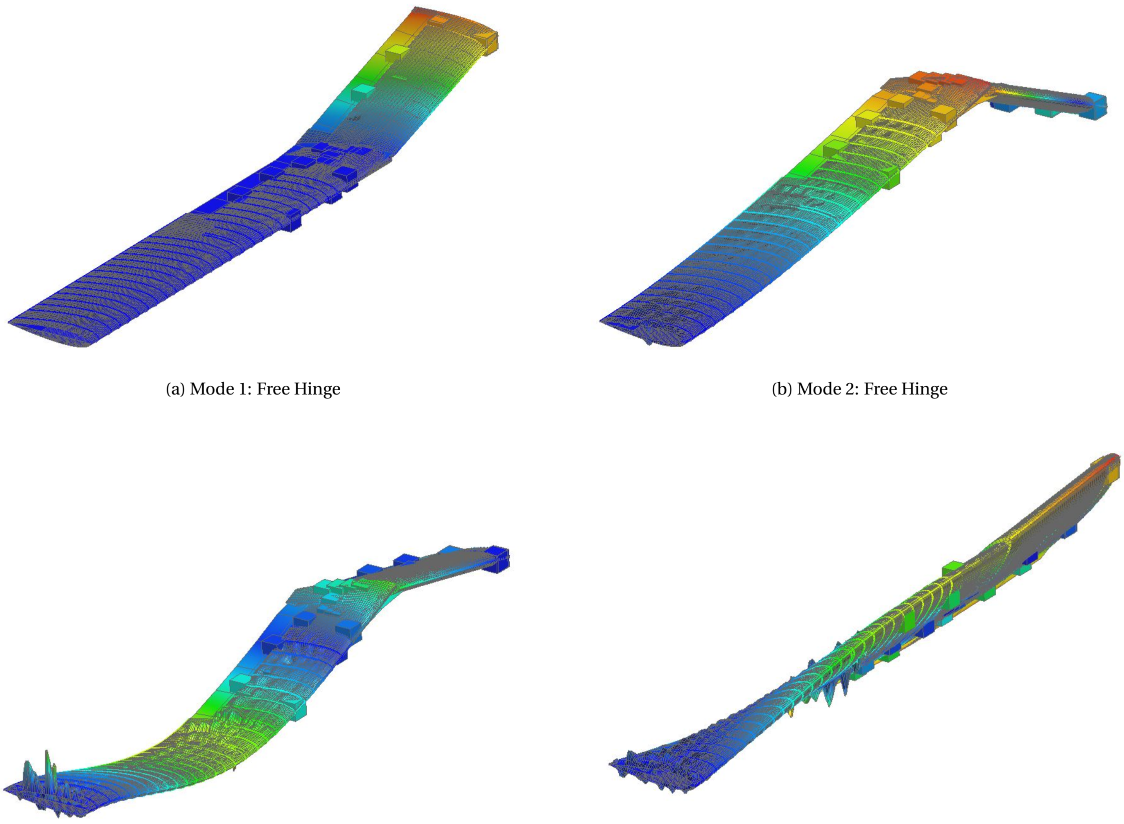

(a) Mode 1: Free Hinge

(b) Mode 2: Free Hinge

(c) Mode 3: Free Hinge

(d) Mode 4: Free Hinge

Figure 4.40: Visualization of Modes 1 to 4 with Free Hinge Configuration

As can be observed in Figure 4.41, mode 1 and mode 2 interact at relatively low velocities, and mode 3 and mode 4 interact at velocities closer to 30 m/s. In order to more accurately predict the flutter velocity, the damping plot of these modes is used.

Figure 4.42 shows the damping plot for the first 4 modes. The velocity at which the damping of a mode switches from negative to positive corresponds to the flutter velocity. For the first flutter mechanism (a combination of mode 1 and mode 2), fluter occurs at 12 m/s. The second flutter mechanism occurs at 31 m/s. Since requirement *Req-3* states that the flutter speed must be close to, but not exceed, 25 m/s, a plate thickness of 3.2 mm does not come close to satisfying the requirement.

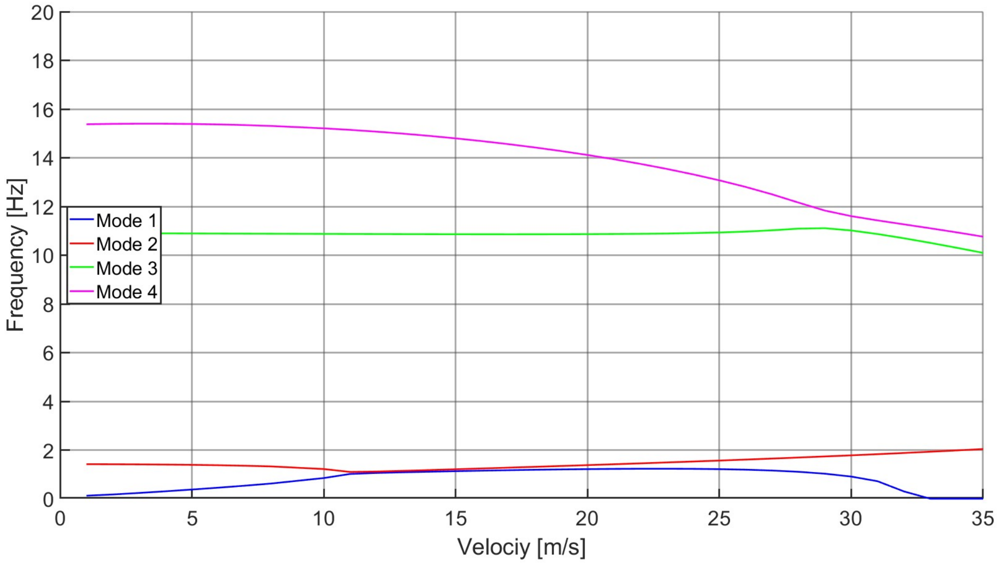

Figure 4.41: Frequency plot of first 4 modes with a plate thickness of 3.2 mm

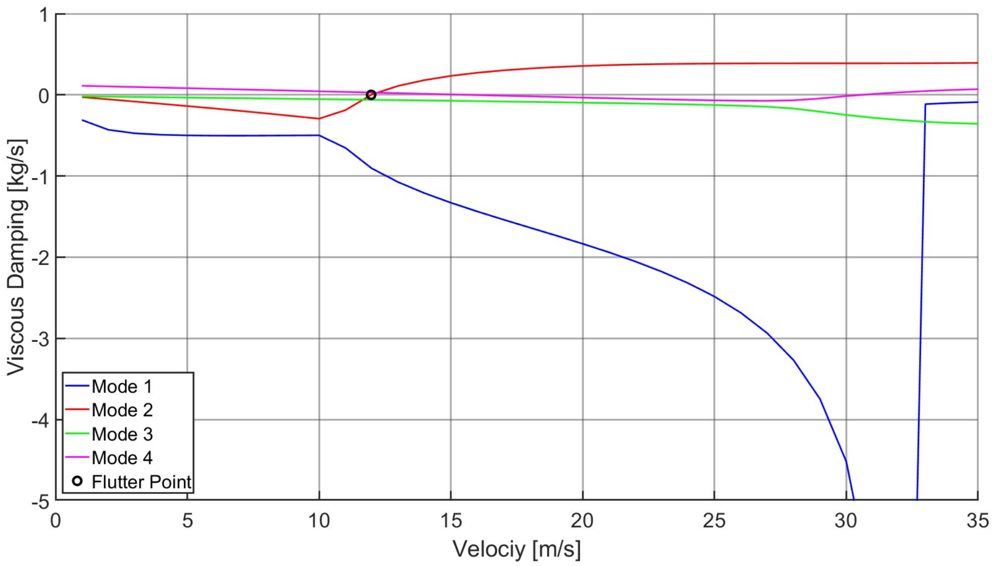

Figure 4.42: Damping plot of first 4 modes with a plate thickness of 3.2 mm

The plate thickness is increased to 5 mm, resulting in the frequency and damping plots shown in Figure 4.44 and Figure 4.45. By increasing the plate thickness, and thus increasing the bending and torsional frequencies, the torsional mode as displayed in Figure 4.40d is replaced by the lead-lag mode of the wingtip, making mode 4 a lead-lag mode, and mode 5 the torsional mode. The lead-lag mode is displayed in Figure 4.43:

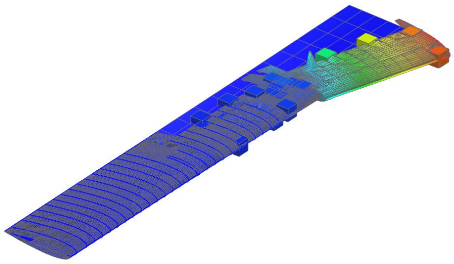

Figure 4.43: The lead-lag mode shape

Therefore, the frequency plot (Figure 4.44) of the wing with a 5 mm thick plate includes the first 5 modes. As can be observed, the frequency of mode 3 and mode 5 no longer interact in this velocity range. Flutter in this velocity range will only occur as an interaction of mode 1 and mode 2. The damping plot is presented in Figure 4.45, showing only the first two modes.
The damping plot shows that by increasing the plate thickness to 5 mm, the flutter speed has increased to 20 m/s. The requirement specifies that the flutter speed must be close to 25 m/s, but not higher. Next, a plate thickness of 6 mm is simulated. This is the maximum allowable thickness, as it equals the dimension of the cut-out in the ribs.

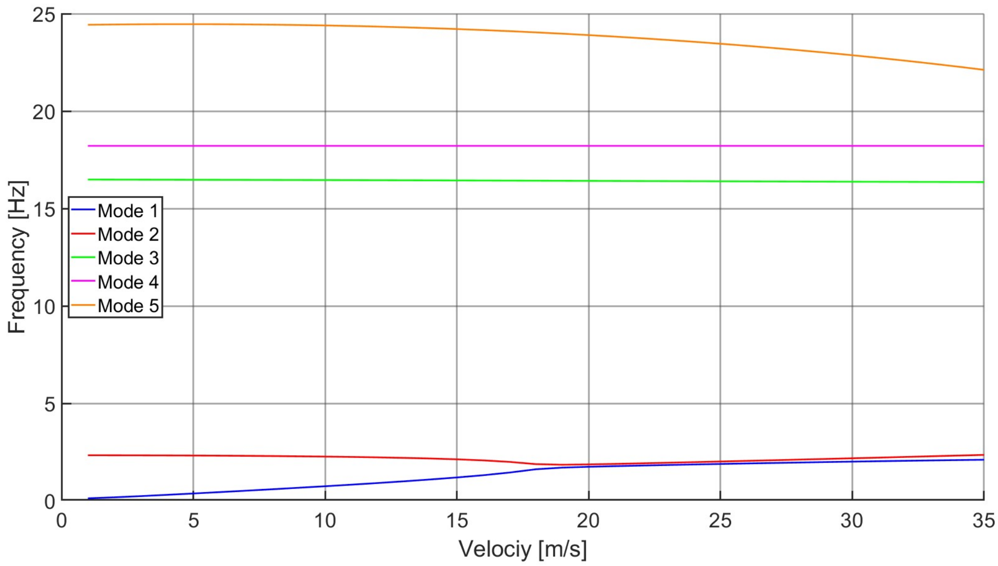

Figure 4.44: Frequency plot of first 5 modes with a plate thickness of 5 mm

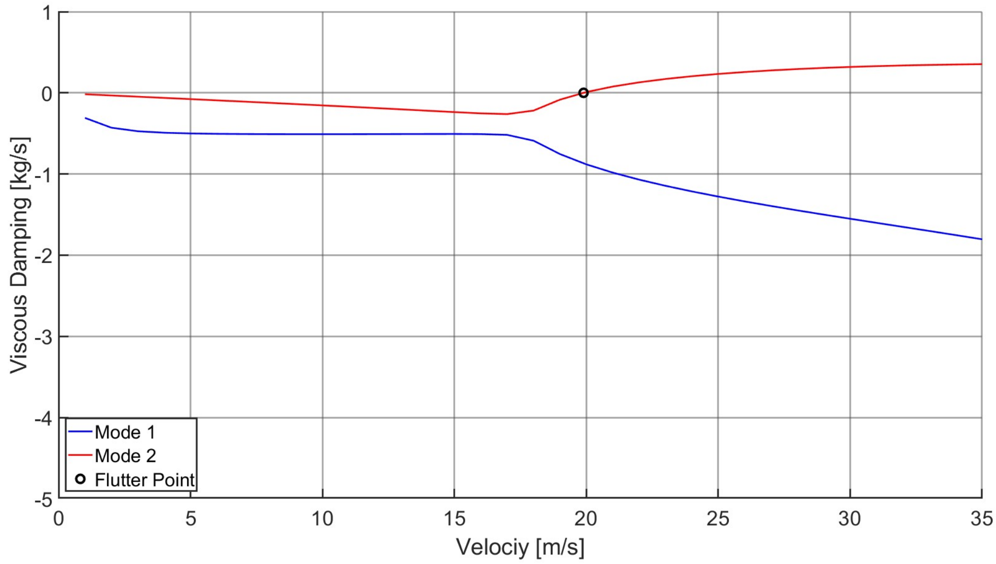

Figure 4.45: Damping plot of first 2 modes with a plate thickness of 5 mm

The frequency and damping plot corresponding to a plate thickness of 6 mm are shown in Figure 4.46 and Figure 4.47, respectively. Again, only mode 1 and mode 2 seem to interact within the velocity range. Therefore, the damping plot only shows the first two modes. Increasing the plate thickness to 6 mm has increased the flutter velocity to 25 m/s, which is exactly maximum flutter speed stated in the requirement. Now that the flutter speeds for different plate thicknesses are analyzed, the wingtip deflection for these thicknesses can be computed.

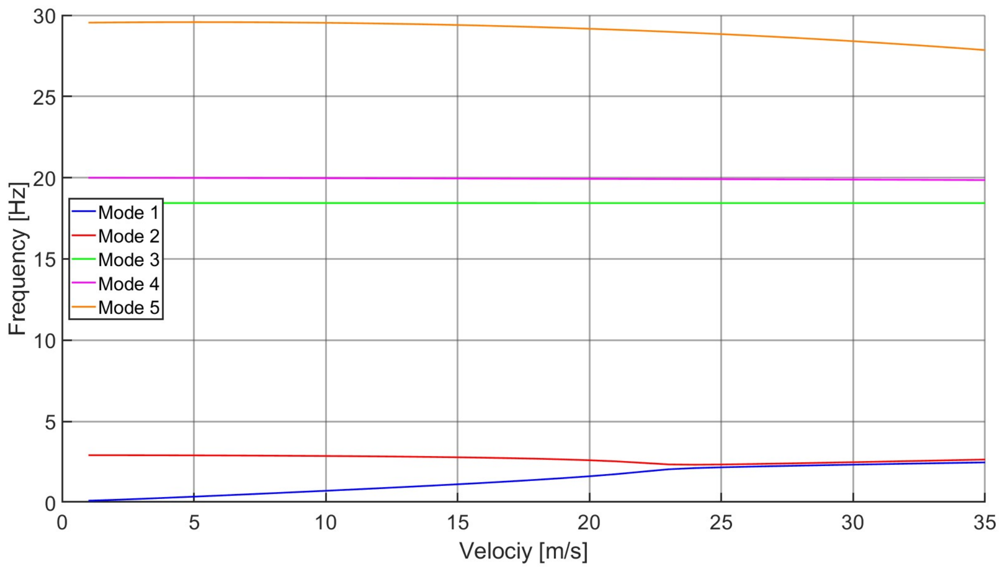

Figure 4.46: Frequency plot of first 5 modes with a plate thickness of 6 mm

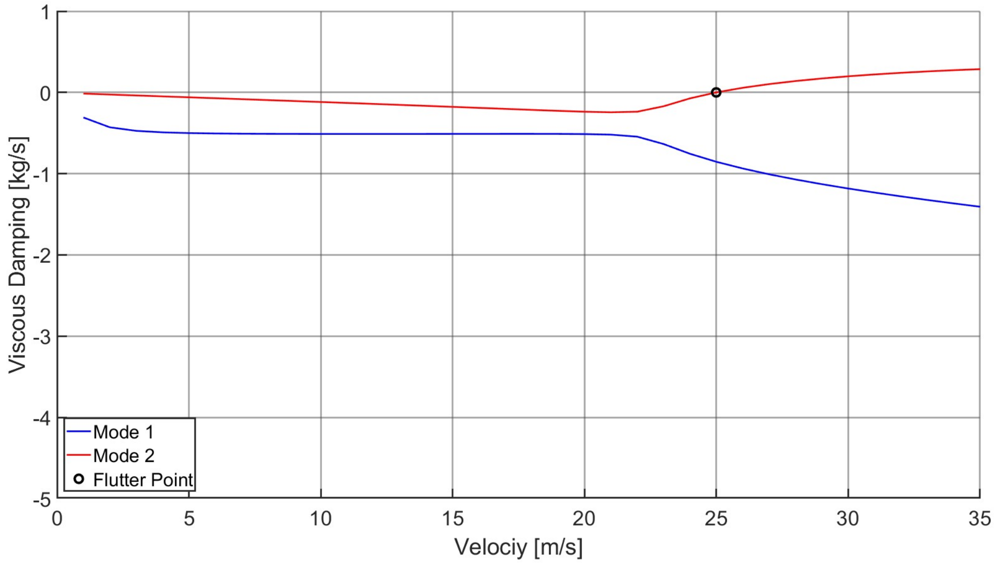

Figure 4.47: Damping plot of first 2 modes with a plate thickness of 6 mm

WINGTIP DEFLECTION ANALYSIS

To assess the deflection, the hinge stiffness is increased to simulate the locked hinge condition. Since the wing is designed to test horizontally in the wind tunnel, gravity is taken into account during the simulation. The wingtip deflection is computed at $\alpha_{n=2.5} = 5°$ and at $V_{max} = 25$ m/s as mentioned in *Req-4*. The requirement specifies a 15%-20% tip deflection to have a highly flexible wing. To explore the possibilities of testing at higher angles of attack, an angle of attack of 10° is also simulated. The results of $\alpha = 5°$ are displayed in Table 4.6, and the results of $\alpha = 10°$ are displayed in Table 4.7.

Table 4.6: wingtip deflection results - $\alpha = 5°$

Plate thickness	wingtip deflection [mm]	wingtip deflection [%]
3.2 mm	291.7 mm	18.9%
5.0 mm	86.8 mm	5.64%
6.0 mm	49.2 mm	3.19%

Table 4.7: wingtip deflection results - $\alpha = 10°$

Plate thickness	wingtip deflection [mm]	wingtip deflection [%]
3.2 mm	982.0 mm	63.8%
5.0 mm	321.0 mm	20.8%
6.0 mm	192.6 mm	12.5%

Looking at Table 4.6, it is observed that only the plate of 3.2 mm thickness satisfies the wingtip deflection requirement. However, this would result in a flutter speed of 12 m/s. Since a low flutter speed heavily limits the velocity range of the wind tunnel experiments, and would reduce the Reynolds number to very low numbers, a plate thickness of 3.2 mm is not feasible. However, increasing the thickness of the plate results in not satisfying the wingtip deflection requirement. It appears that the flutter speed requirement and the wingtip deflection requirement are conflicting. By conducting a sensitivity analysis on mass tuning the wing, the goal is to maintain the wingtip deflection while increasing the flutter speed of a 3.2 mm plate.

SENSITIVITY ANALYSIS

In an attempt to increase the flutter speed without increasing the plate thickness, a sensitivity analysis with mass tuning is performed. In the FEM model, four concentrated masses are independently varied in mass, and the flutter, after which the flutter speed is computed. Two concentrated masses are located at the leading and trailing edge of the wingtip. The other two masses are located at leading and trailing edge of the mid-span of the demonstrator. The location of the concentrated masses are marked in orange in Figure 4.48:

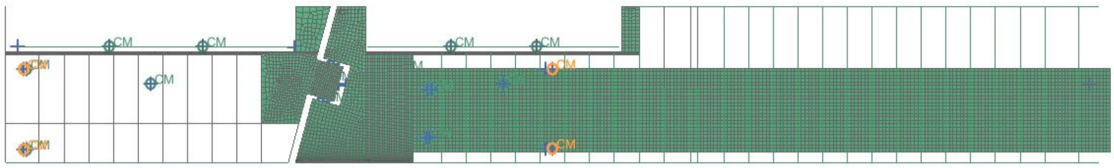

Figure 4.48: Concentrated masses (marked in orange) to perform mass tuning

The mass at each point is increased from 0 grams to 320 grams. The results are plotted in Figure 4.49. It can be observed that adding mass to either one of the mid-span locations decreases the flutter speed. On the other hand, adding mass to the wingtip locations slightly increases the flutter speed. These results can be explained by looking at the frequency plot in Figure 4.41; since the flutter speed is the point at which the frequency of mode 1 and mode 2 move close together, one must separate these modes to increase the flutter speed. Since mode 1 considers the flapping motion of the wingtip, adding mass to the wingtip will lower the frequency of mode 1. This will delay the interaction between mode 1 and mode 2, and will increase the flutter speed. Mode 2 corresponds to the first bending mode of the wing. By adding masses to the main wing, the frequency of mode 2 will be lowered, bringing mode 1 and mode 2 closer together and decreasing the flutter speed.

If mass tuning would be used to have sufficient wingtip deflection while satisfying the flutter speed requirement, mass should be added to the wingtip. However, adding as much as 320 gram to the trailing edge of the wingtip only increases the flutter speed from 12 m/s to 14 m/s. This flutter speed is far too low, while adding more mass is unrealistic.

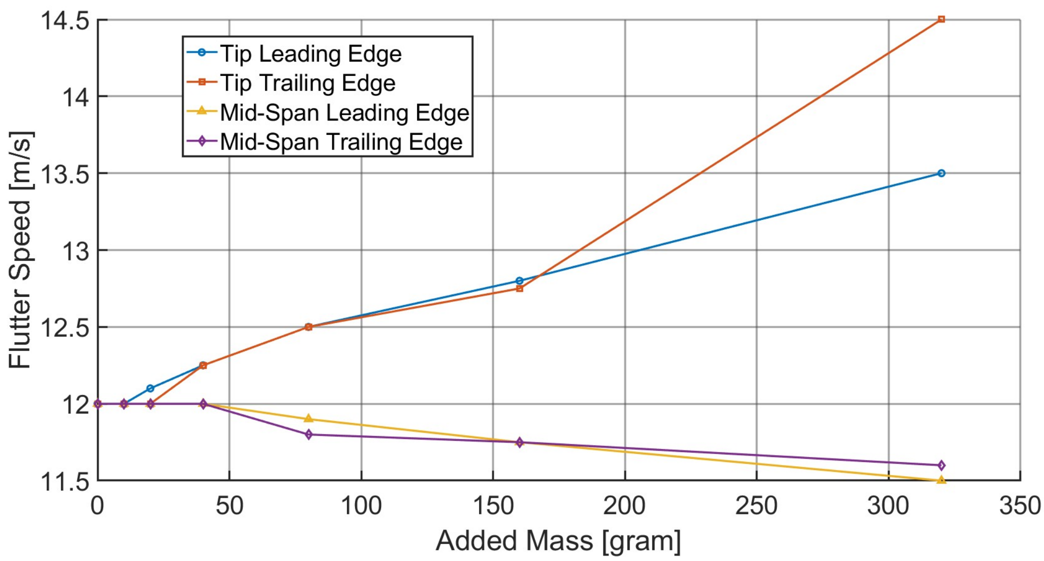

Figure 4.49: Effect of mass tuning on flutter speed with a plate thickness of 3.2 mm

It must be concluded that the flutter speed requirement and the wingtip deflection requirement for this wing are conflicting too much, and cannot be satisfied both. To achieve sufficiently high Reynold numbers, the plate thickness of 5.0 mm with a flutter speed of 20 m/s and a wingtip deflection of 5.64% is selected, satisfying *Req-3* at the cost of *Req-4*.
If, in future experiments, a larger wingtip deflection is desired, several options are available to achieve this. Some examples are: Testing the wing vertically. This will remove most of the effect gravity has on the wing,

which will significantly increase the wingtip deflection. Another alternative would be to test the wing at negative angles of attack. Since the wing is symmetric, the aerodynamics would behave similar to that of testing at positive angles of attack, while gravity is assisting the wingtip deflection. Nevertheless, changing the orientation of the wing would change the dynamics of the system, and might make the testing less representative of a real wing.

After the final sizing is performed, the structural modes of the wing are computed and compared to those computed for the sizing of the aileron servo actuators. With the updated FEM, and a plate thickness of 5 mm, the first two bending mode frequencies are 0.992 Hz and 7.34 Hz in locked hinge condition. In free hinge conditions, the first two bending mode frequencies are 1.42 Hz and 10.91 Hz. The objective of the aileron servo actuator was to be able to operate within the first two bending modes in locked hinge condition. With the preliminary FEM model, the first two bending mode frequencies were 1.27 Hz and 8.30 Hz in locked hinge condition. It appears that the bending modes have slightly decreased in frequency in the updated FEM model. This could be explained by the increase in size, and thus mass, of the 3D printed sections near the hinge on both the main wing and the wingtip. This increase in mass has decreased the first two bending frequencies, which assures that the aileron servo actuator sizing with the preliminary FEM model has been conservative.

The results of the plate sizing procedure are summarized in Table 4.11.

4.4. SIZING SUMMARY

This section presents an overview of the sizing results as discussed in the sections above.

For the aileron sizing, the results are presented in Table 4.8:

Table 4.8: Result summary of aileron sizing

Aileron	Span	X/C
Inboard aileron	0.7	0.75
Outboard aileron	0.9	0.75

The results of the aileron and hinge servo actuator sizing are presented in Table 4.9 and Table 4.10, respectively.

Table 4.9: Aileron servo actuator sizing results summary

Specification	Result
Required torque	$1.27\ \mathrm{kg \cdot cm}$
Required speed	0.058 sec/60°
$\frac{r_a}{r_s}$	0.8
Selected Servo Actuator	Blue Bird BMS-A10V

Table 4.10: Hinge servo actuator sizing results summary

Specification	Result
Required torque	$33\ \mathrm{kg \cdot cm}$
Selected shape	Eccentric circle
Selected Servo Actuator	Blue Bird BLS-73A

At last, the results of the plate sizing are summarized below:

Table 4.11: Summary of plate sizing results

Parameter	Value
Plate thickness	5 mm
Flutter speed	20 m/s
wingtip deflection	5.64%

5

Detailed Design

The detailed design stage marks the final step before manufacturing. This phase involves implementing the sizing results and ensuring a feasible design, which requires careful consideration of manufacturing processes, assembly procedures, and the availability of necessary components.
Section 5.1 explains the key aspects of the aileron mechanism design. In Section 5.2, the important details of the hinge mechanism design are highlighted. Section 5.3 focuses on the detailed design of the 3D printed frame, which include the accelerometer supports, rib structures and root connection. Finally, the sensor distribution is presented in Section 5.4. Additional details can be found in Appendix A.

5.1. Aileron Mechanism Design

The inboard and outboard aileron have a similar functional design, though their spans is defined by the results of the aileron sizing Section 4.1. Figure 5.1 provides an isolated view of the aileron.

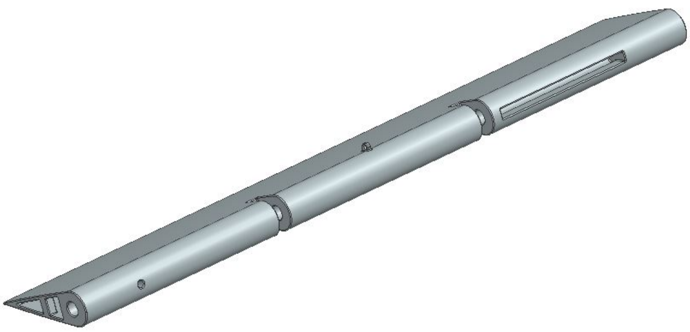

Figure 5.1: Detailed design of an aileron

The leading edge of the aileron and the aft part of the trailing edge spars of the demonstrator are both curved, with their centers aligned with the aileron's hinge line. This design ensures a smooth leading edge for the aileron while maintaining a minimal gap between the aileron and the wing. Additionally, the aileron is designed to be lightweight, requiring a hollow structure. However, in SLS printing, a layer of powder is sintered into a solid only at specific locations. A fully hollow structure would trap powder within the aileron. To prevent this, the sides of the aileron are left open, as shown in Figure 5.1, and reinforced to support the skin. This approach allows for a mainly hollow design while ensuring that the powder can be easily removed during post-processing
The leading edge of the aileron is kept solid to accommodate an axle. A hole is created on the left side of the aileron, with a corresponding aligned hole in the wing, allowing the axle to pass through the aileron and its supports. The hole ends at the far right of the leading-edge cutout. This cutout enables the axle to be pushed back for easy disassembly of the aileron from the wing. To secure the aileron axle in place, a set screw is inserted into the hole on the left side of the leading edge. Since both the cutout and the hole are located at the leading edge, they do not impact the aerodynamic performance of the design.

Two primary cutouts in the aileron align with the aileron supports on the wing's trailing edge. Bearings are used to ensure smooth rotation of the axle within the aileron. Due to potential misalignments caused by manufacturing tolerances or wing bending, simple bearings may not rotate freely. To address this, joint bearings are installed in the aileron supports, as they can both rotate and align with the axle. Simple bushings are placed inside the aileron to transfer loads effectively from the aileron to the axle.
Finally, a small flange is added to the top of the aileron, designed to connect with a push rod. The position of the hole in the flange corresponds to the selected $\frac{r_a}{r_s}$.

Figure 5.4 illustrates how an aileron servo actuator is integrated into the 3D-printed structure. A support is printed between two adjacent ribs, featuring cutouts to accommodate the servo actuator flanges and wires (Figure 5.2a). Since the wing will be covered with Oracover, a hole is necessary to connect the servo actuator to the aileron. However, heating the Oracover during attachment and stretching can cause this hole to tear. To prevent tearing, a cover is placed over the servo actuator, providing a surface for attaching the Oracover (Figure 5.2b). This ensures the Oracover remains intact while allowing the aileron horn to extend through the cover.

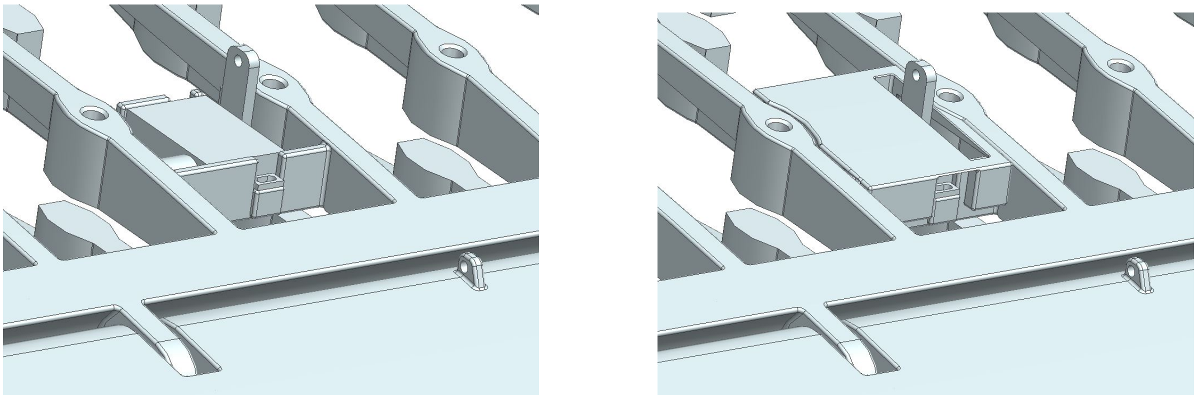

(a) Aileron servo actuator without cover

(b) Aileron servo actuator with cover

Figure 5.2: Comparison of aileron servo actuator with and without cover

5.2. HINGE MECHANISM

The main purpose of the hinge mechanism is to lock the wingtip in neutral position under all testing conditions. Secondly, the hinge is designed to let wires pass through, such that they will not disrupt the airflow. To ensure the hinge mechanism can be locked under all conditions, the hinge servo actuator and the eccentric circle are sized in Section 4.2.2. After evaluating the maximum required torque on the hinge servo actuator, the Blue Bird BLS-73A servo actuator is selected. In order to provide a quick release of the hinge, a spring is pushing back the pin once the servo actuator unlocks the hinge, as can be seen in Figure 5.3.

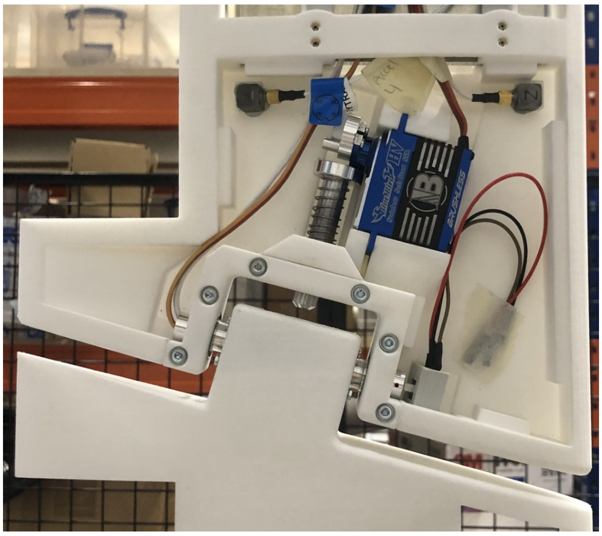

Figure 5.3: Picture of hinge mechanism

The hinge mechanism is secured by six M3 bolts. Removing these bolts allows the cap to be detached, enabling the hinge axle and wingtip to be separated from the main wing. This design facilitates partial disassembly of the wingtip and main wing, which is essential for accommodating the wires that run through the hinge. Inside the wingtip, an aileron servo actuator and two accelerometers are installed. To minimize interference with the airflow around the wing, the hinge axle features a hollow design that allows the wires to pass seamlessly through the axle. To transfer loads from the wingtip to the locking pin, an aluminum cap, referred to as the contact plate, is mounted at the front of the axle.
Figure 5.4a illustrates the primary components surrounding the hinge axle. On each side of the axle, a square plate and a ball bearing are positioned. The square plates secure the axle to the wingtip using M2 screws, while the ball bearings fit into the main wing to allow free rotation of the wingtip. A small increase in thickness near the ends of both sides of the axle minimizes play in the hinge along the chordwise direction. The contact plate is secured to the axle with two M3 screws from the front and two M2 screws through the rectangular plates on both sides.
Figure 5.4b depicts the connection between the axle and its surrounding parts to the wingtip.

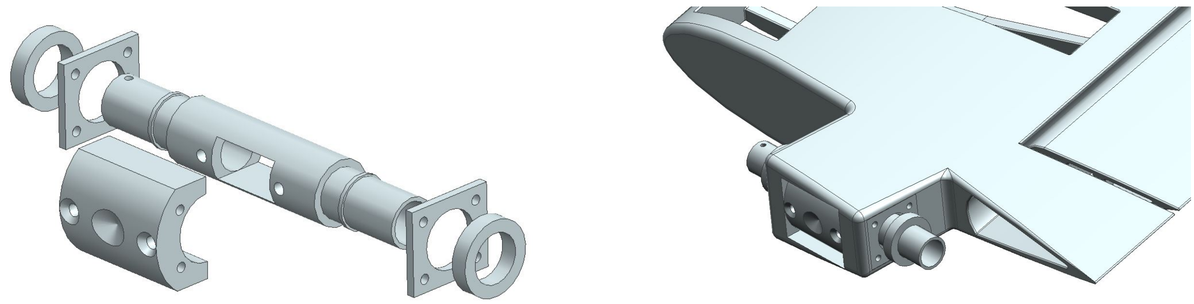

(a) Exploded view of hinge axle

(b) CAD representation of wingtip - axle combination

Figure 5.4: Comparison of aileron servo actuator with and without cover

Finally, Figure 5.5 demonstrates how the wingtip, along with its axle, is assembled into the main wing. The assembly process begins by placing the assembled wingtip into the main wing. This step ensures automatic alignment, as the ball bearings fit into their designated cutouts. To complete the hinge mechanism, the cap shown at the top of Figure 5.5 is secured using six M3 bolts. The holes are designed to ensure that both the bolt heads and the ends of the threads remain flush with the wing surface, minimizing any potential impact on the surrounding airflow.

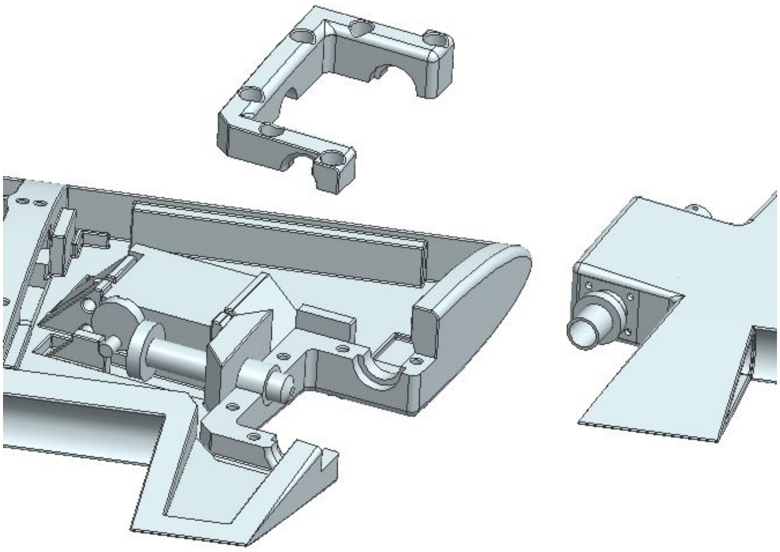

Figure 5.5: Exploded view of wingtip - main wing connection

In Figure 5.6, the removed contact plate, positioned on the on the right side of the image, reveals the cut-out in the hinge axle. This design helps guide the wires smoothly around the corner as they pass through the hinge. Once the wires are properly routed, the contact plate is secured as shown in Figure 5.4a.

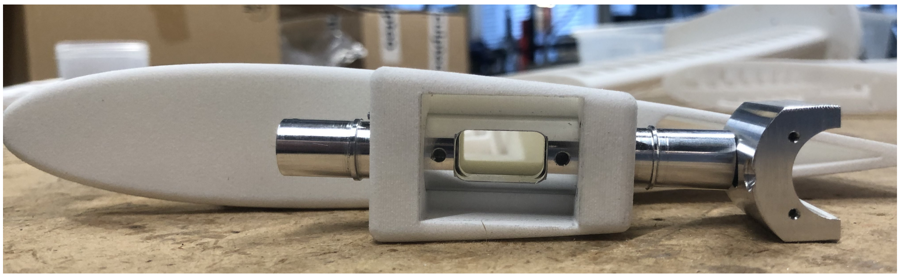

Figure 5.6: Picture of axle, contact plate and wingtip

At the left side of the axle in Figure 5.3, the wires enter the main wing. At the right side, the diameter of the hole in the axle is much smaller, and sized to fit the shaft of a potentiometer. Connecting a potentiometer to the shaft enables measuring the fold angle of the wingtip.

5.3. 3D PRINTED FRAME

The shape of the wing is defined by the 3D-printed components, including main section 1, main section 2, and the wingtip, collectively referred to as the main frame. Figure 5.7 illustrates the key features of this frame, with different colors highlighting specific details. The locations of the accelerometers are indicated in yellow. The rib structure in the wingtip is marked in blue, while the rib structures of main section 1 and main section 2, along with the connecting ribs, are highlighted in red. The root connection is highlighted in green. Finally, some additional details of the frame are discussed. Each of these elements is described in detail in the following paragraphs.

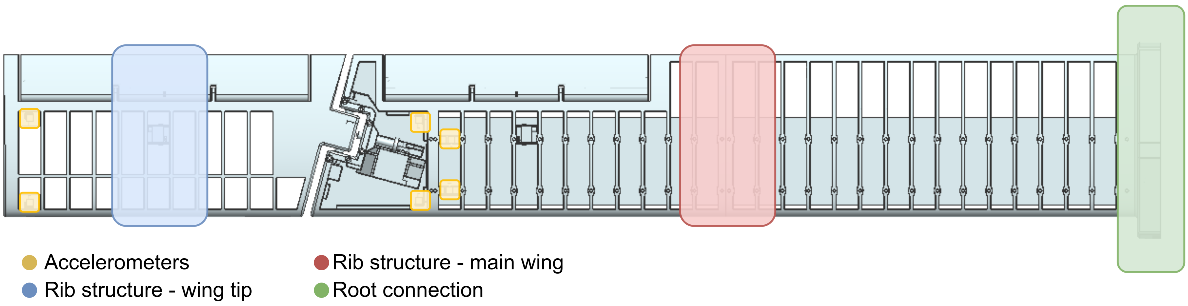

Figure 5.7: Highlighted details of 3D printed frame

Accelerometer Support (Yellow)

In Figure 5.8, the accelerometer support structure located at the leading edge of the wingtip is displayed. Each accelerometer location is supported by two walls that secure its position, ensuring precise placement for accurate signal post-processing. Section 5.4 will elaborate more on the location of each accelerometer.

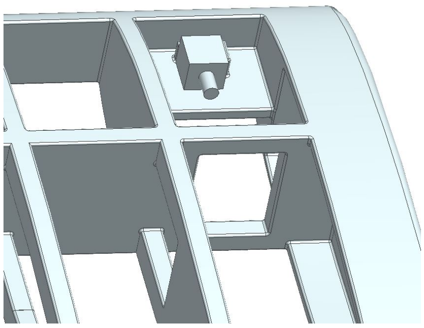

Figure 5.8: Accelerometer support detail

wingtip rib structure (Blue)

The rib structure in the wingtip is shown in Figure 5.9. The main ribs are primarily hollow to reduce weight. However, the ribs adjacent to the aileron servo actuator are partially solid to facilitate a connection with the 3D-printed servo actuator support. Holes at the front of these two ribs are included to allow the passage of cables for the accelerometers and servo actuator.

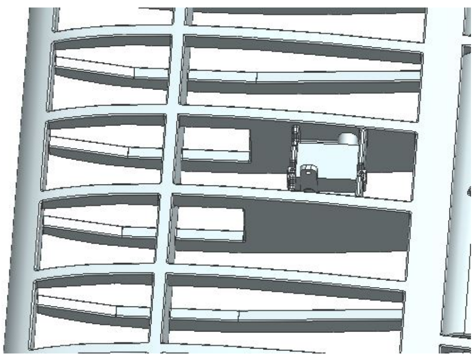

Figure 5.9: wingtip rib structure detail

Main wing rib structure (Red)

In Figure 5.10, the three different rib structures of the main wing are shown. All ribs, from the root up to and including the bottom rib in the image, have their trailing edge sections hollowed out to reduce weight. The ribs connecting Main Section 1 and Main Section 2 are thickened by 5 mm each. These sections are joined using five M3 bolts, with the holes positioned to ensure that the washers do not interfere with either the

aluminum plate or the Oracover skin. At the aileron, the rib is shortened and connected to the trailing edge spar.
In all ribs of the main wing, a cut-out is made above and below the aluminum plate to allow the wires and their connectors to pass through. The holes at the top of the ribs are designed to accommodate threaded inserts for M2 set screws. These set screws provide load transfer between the ribs and the aluminum plate. The holes are slightly smaller in diameter than the threaded inserts, ensuring a tight fit. By pressing the threaded inserts into place with a heated soldering iron, a strong connection is formed between the inserts and the 3D-printed structure.

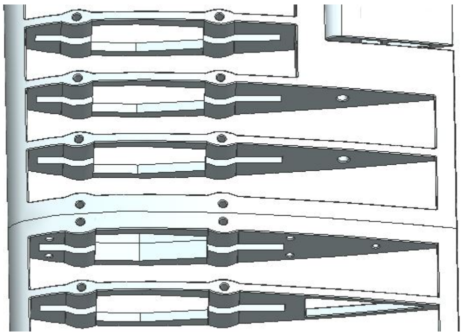

Figure 5.10: Main wing rib structure detail

ROOT CONNECTION (GREEN)

Eventually, the wing must be mounted to a structure during the experiments. A base plate is designed at the root to transfer the wing's loads to the structure. Figure 5.11 illustrates the base plate from both the wing side and the root side.

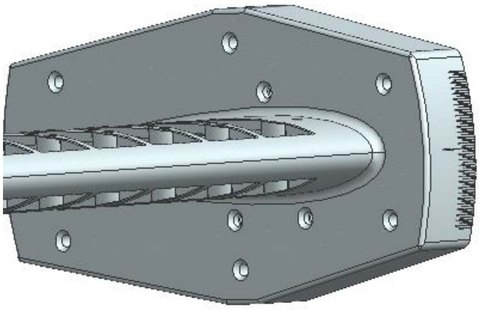

(a) Detailed design of base plate - wing side

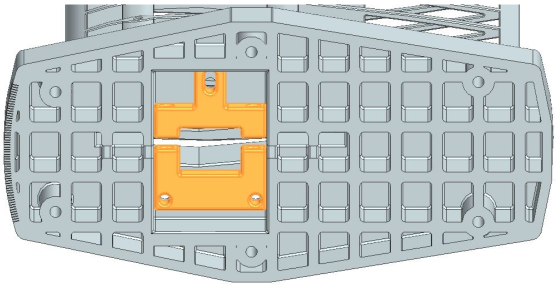

(b) Detailed design of base plate - root side

Figure 5.11: Base plate seen from both sides

In Figure 5.11a, markings on the leading edge can be observed. These lines serve as visual indicators for the angle of attack of the wing. Additionally, nine holes are located in the plate. The outer six holes are used to attach the plate to an adapter for the structure, while the inner three holes, near the wing, are used to connect the two aluminum brackets highlighted in Figure 5.11b. These brackets transfer the loads from the aluminum plate to the 3D-printed structure at the root.
In Figure 5.12, an exploded view of the connection between the aluminum plate, brackets, and base is shown. First, the brackets are bolted to the aluminum plate, ensuring a secure connection. Then, the plate and brackets are fully pressed into the wing, after which the aluminum brackets are bolted to the base structure. The hollow pattern in the base plate significantly reduces weight and material, thus lowering production costs.

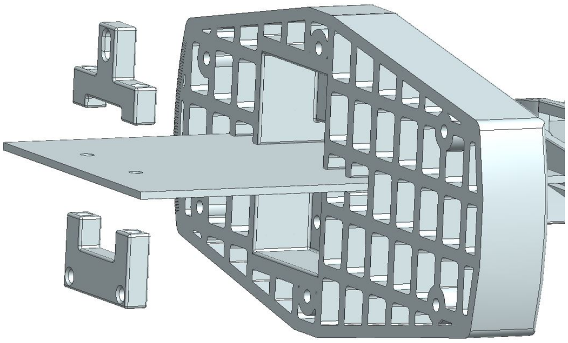

Figure 5.12: Exploded view of connection between aluminium plate, brackets and base

ADDITIONAL DETAILS

Some details do not fall into the categories mentioned above, but are still crucial to the design.
Similar to the aileron servo actuators, a 3D-printed cover is placed over the hinge mechanism to maintain the proper airfoil shape. Figure 5.13 compares the 3D-printed part with and without the cover.

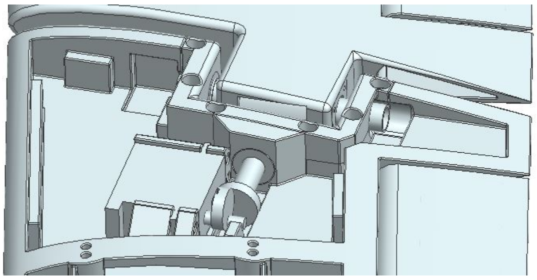

(a) Hinge mechanism without cover

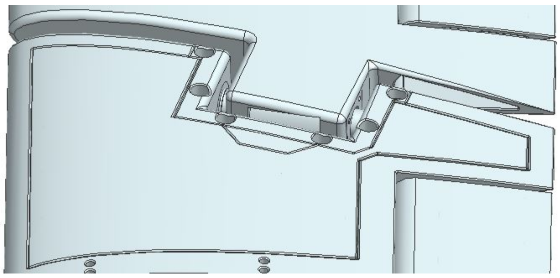

(b) Hinge mechanism without cover

Figure 5.13: Comparison of Hinge mechanism with and without cover

In the last rib of the wingtip (Figure 5.14), four holes for M3 bolts are made. These holes allow for the addition of external masses or sensors to the wingtip, which could be useful in future work. The far-left hole in the image accommodates the axle of the aileron, as described in Section 5.1.

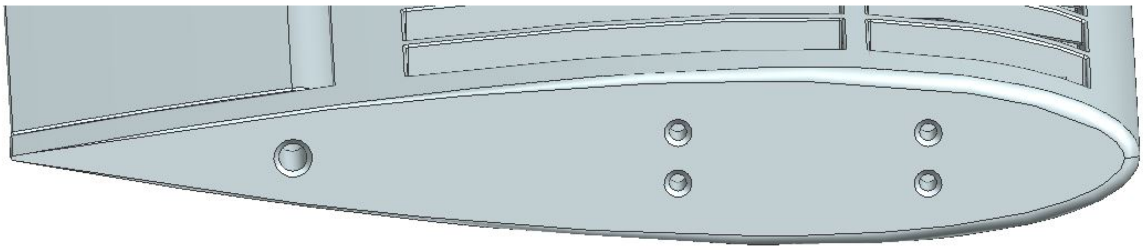

Figure 5.14: wingtip rib

5.4. SENSOR DISTRIBUTION

Three types of sensors are used in the wing: accelerometers to measure the acceleration at different locations on the wing, a potentiometer connected to the axle of the hinge to measure the fold angle of the wingtip, and strain gauges to obtain the root bending moment. Figure 5.15 dislpays the location of all sensors on the wing.

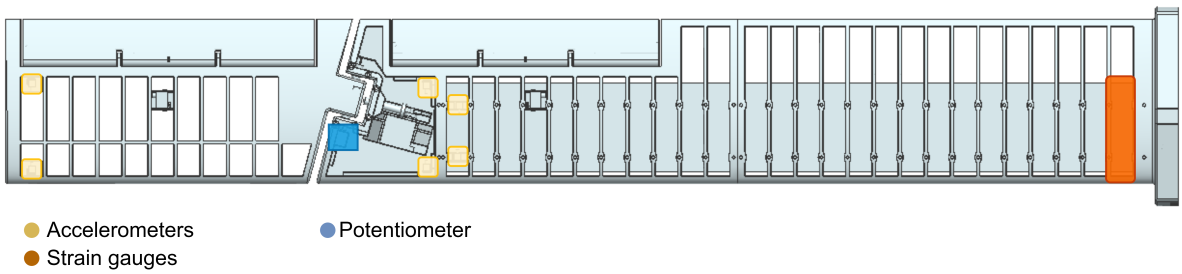

Figure 5.15: Sensor distribution on 3D assembly

ACCELEROMETERS

A total of six accelerometers are installed in the wing: two at the wingtip, two in the cut-out section for the hinge mechanism, and two on the opposite side of the rib. Their locations are indicated in yellow in Figure 5.7. Positioning two accelerometers at the same spanwise location but at different chordwise locations enables the measurement of torsional motion. While two accelerometers in the hinge mechanism cut-out would suffice, the additional accelerometers on the opposite side of the rib help assess noise introduced by the hinge mechanism (which was a problem in the previous design) and determine whether measurements from the opposite side improve signal quality.

STRAIN GAUGE LOCATION (ORANGE)

A simple method for measuring the Root Bending Moment is to apply strain gauges to the aluminum plate. While a balance capable of accurately measuring forces and moments in three directions will be available in the future, the strain gauges provide added value by offering redundancy. They serve as an effective backup, ensuring that measurements can still be obtained if the primary balance system encounters any issues. Since the strain gauges mainly function as a backup, the type selected was based on the ones available in the workshop

POTENTIOMETER

At last, the shaft of a potentiometer is fitted to the axle of the wingtip hinge. By fixing the potentiometer to the main wing, but letting the shaft rotate with the axle, the change in voltage during the flapping motion of the wing can be transformed to the fold angle.

6
Testing

After completing the detailed design, manufacturing, and assembly of the wing, the accuracy of the structural model must be assessed. This is done through a Ground Vibration Test (GVT), where the modal properties of the physical wing are measured. Comparing the GVT results to the FEM modal analysis of the structural model provides insight into its accuracy.
Section 6.1 describes the GVT procedure, followed by Section 6.2, which presents the test results and their comparison with the structural simulations.

6.1. Ground Vibration Test Procedure

A Ground Vibration Test (GVT) is conducted to determine the modal properties. This thesis focuses solely on comparing the structural frequencies between simulations and GVT results, without addressing mode shapes or updating the model.
The eigenfrequencies of the physical wing are determined by exciting the wing with a manual impact hammer (Model 086C02[1]), and measuring the response with accelerometers installed on the wing. While a single accelerometer would suffice for capturing bending modes in the locked hinge condition, and an additional accelerometer placed at the same spanwise position but a different chordwise location would enable the detection of torsional modes, six accelerometers are used to obtain a more comprehensive dataset.
This additional set of accelerometers allows for a more complete characterization of the wing's behavior. A pair of accelerometers at the wingtip and another pair on the main wing enable analysis in both the locked and free hinge conditions. Additionally, two accelerometers are positioned near the hinge mechanism on opposite sides of the last rib, facilitating potential future analysis of the noise introduced by the hinge mechanism. The positioning of the accelerometers is described in Section 5.4.
To capture the response, the GVT is conducted using the workflow in Siemens Testlab alongside the SCADAS[2] data acquisition system. This section follows this workflow to illustrate the GVT setup.

The first step is the channel setup. Since the accelerometers on the wing are tri-axial, each accelerometer provides separate inputs for each acceleration direction. For this GVT, only the out-of-plane direction (Z-axis) is selected as the input to analyze the eigenfrequencies. The impact hammer input is chosen as the reference channel, and force is selected as the measurement quantity.
The sensitivity of each accelerometer can be retrieved automatically. However, for the impact hammer, the sensitivity is manually set to 11.2 mV/N, as specified by the manufacturer.
After completing the channel setup, the impact setup is performed. Within the impact setup, there are four different worksheets. First, the trigger level of the impact hammer is determined by striking the wing several times while recording the signal from the hammer. The software uses the trigger level to start the measurement and to determine whether the impact was sufficient.
Second, the bandwidth of the measurement is determined. After striking the structure several times, the Power Spectral Density (PSD) of the last impact and the average PSD are plotted. The PSD provides insight

[1] See "Impact Hammers," PCB Piezotronics, https://www.pcb.com/products?m=086c02.
[2] See "Simcenter SCADAS Mobile," Siemens, https://plm.sw.siemens.com/en-US/simcenter/physical-testing/scadas/mobile/?srsltid=AfmBOorqNsWTUo006pftW7KgJ2CVSTOolWE7pj6JCzPmBNrQ3HwTFLbF.

into how the power delivered by the hammer is distributed across the frequency range of interest. Ideally, the PSD would display a horizontal line, indicating that the power delivered to all frequencies is constant. However, this is not realistic, so the goal is to make the PSD line as horizontal as possible. This can be achieved by selecting the appropriate hammer tip. Depending on the material the hammer is striking, the material and hardness of the hammer tip can be adjusted to optimize the PSD. Since the wing has relatively low eigenfrequencies, the bandwidth is set to 204.80 Hz. With an acquisition time of 10 seconds and 2048 spectral lines, the resolution becomes 0.10 Hz.
Finally, after selecting the appropriate trigger level and hammer tip, signal windowing can be considered for relatively long acquisition times and noisy signals, since the signal-to-noise ratio may decrease significantly. However, in this case, minimal measurement noise was observed during the windowing process, eliminating the need for additional signal windowing. With this, the GVT setup is complete, allowing the test to be conducted successfully.

During the GVT, the Frequency Response Function (FRF) is averaged over ten measurements. The FRF represents the accelerometer response after the wing is struck with the impact hammer. To ensure accurate results, Testlab automatically discards instances of double impacts. Additionally, impacts below the trigger level threshold are excluded from the measurement, as specified in the impact setup.
Peaks in the FRF are used to estimate the eigenfrequencies of the wing. The GVT is performed under both the locked hinge and free hinge conditions. To maintain the highest measurement accuracy, the GVT setup is adjusted when switching between the locked and free hinge configurations. In Appendix B, the FRFs can be found for both the locked and free hinge conditions.
The following section presents the GVT results for both hinge conditions and compares them with the FEM modal analysis outcomes.

6.2. GROUND VIBRATION TEST RESULTS

This section compares the results of the GVT with those from the FEM modal analysis. Due to a manufacturing error in the outboard aileron and extended production times, completing the final wing assembly in time for the GVT was not feasible. Consequently, the test was conducted with both ailerons removed. Additionally, since the Oracover could only be applied after the full assembly, the wing remained uncovered during testing. The aileron servo actuator covers were also omitted, as they are designed to adhere to the Oracover and would have detached during the experiment.
To facilitate a meaningful comparison, the Finite Element Method (FEM) model was modified to reflect the altered test setup, enabling a direct comparison between the GVT results and the structural simulations.
While the assembly tested during the initial GVT differs from the final wing configuration, valuable insights can still be obtained by conducting a second GVT along with a FEM modal analysis of the final assembly. This approach will enable an assessment of the impact of adding the ailerons and Oracover on the eigenfrequencies, as well as an evaluation of the accuracy of the FEM modal analysis.
Table 6.1 and Table 6.2 present a comparison of the first five eigenfrequencies obtained from the GVT and the structural simulation. The relative error between the structural simulation results and the GVT results is calculated using Equation (6.1). In this equation, f_{GVT} and f_{FEM} represent the eigenfrequencies from the GVT and the structural FEM simulations, respectively.

$$\text{Error}[\%] = \frac{f_{GVT} - f_{FEM}}{f_{GVT}} \cdot 100 \tag{6.1}$$

Several conclusions can be drawn from the results. First, a Lead-Lag mode is observed in both tables, despite acceleration being measured only in the out-of-plane direction. Since the accelerometers are attached to the structure with a layer of wax, the Z-axis is not perfectly orthogonal to the X-Y plane. As a result, the Lead-Lag mode appears in the FRF measurements.
Secondly, for the locked hinge configuration, the predicted frequencies of mode 1 and mode 3 deviate only slightly from the GVT results, while the predicted frequencies of mode 2, mode 4, and mode 5 are not well represented by the structural simulation. However, in the free hinge configuration, accurate predictions of mode 2, mode 3, mode 4, and mode 5 are observed. The discrepancy between the predicted frequency of mode 1 (flapping mode) and the measured frequency can be attributed to the modeling approach. In the FEM model, the free hinge is represented as a torsional spring with very low stiffness. However, during the GVT, the wing was mounted vertically with the wingtip pointing toward the floor, causing gravity to act on

the wingtip as an additional restoring force. This introduced an effective stiffness, preventing the wingtip from exhibiting purely free hinge motion. The added stiffness would increase the eigenfrequency, which is consistent with the results from the GVT. Although the rigid body motion of the flapping mode is not properly captured, the other modes in Table 6.2 show that the structural behavior is well represented.
By establishing that the rigid hinge is properly modeled through a hinge stiffness sensitivity analysis (Figure 4.26), and confirming that the wing's structural behavior is adequately captured in Table 6.2, it becomes clear that the discrepancies in Table 6.1 likely arise from another source. During the GVT, unexpected deformations were observed in the 3D-printed structure surrounding the hinge mechanism when locking the hinge, which may not be accurately captured by the rigid hinge assumption in the FEM model.
As observed in Figure 4.26, a reduction in hinge stiffness would lower the frequencies predicted by the structural analysis, potentially aligning them more closely with the GVT results. However, a more detailed analysis is needed to pinpoint the exact cause of the discrepancy. This could involve using the Modal Assurance Criterion (MAC) to refine the FEM model, improving its ability to accurately predict the demonstrator's mode shapes.
Despite the large discrepancies, the Lead-Lag mode is accurately predicted in the locked hinge configuration. Due to the relatively large moment of inertia around the Z-axis (out-of-plane), the flexibility of the hinge structure has less influence on the Lead-Lag mode compared to the bending modes. This further supports the idea that, while the FEM model effectively captures the structural design, the assumption of a rigid hinge is not valid.

Table 6.1: Comparison of GVT and FEM Results for Locked Hinge with Mode Shapes

Locked Hinge	**GVT**	**FEM**	**Error [%]**	**Mode Shape**
Mode 1 [Hz]	1.7	1.75	-2.94%	1^{st} Bending
Mode 2 [Hz]	8.3	10.72	-29.16%	2^{nd} Bending
Mode 3 [Hz]	19.5	19.04	2.36%	Lead-Lag
Mode 4 [Hz]	20.3	26.49	-30.49%	1^{st} Torsion-Bending
Mode 5 [Hz]	24.9	28.33	-13.78%	2^{nd} Torsion-Bending

Table 6.2: Comparison of GVT and FEM Results for Free Hinge

Free Hinge	**GVT**	**FEM**	**Error [%]**	**Mode Shape**
Mode 1 [Hz]	0.9	0.12	86.67%	Flapping
Mode 2 [Hz]	2.3	2.34	-1.74%	1^{st} Bending-Flapping
Mode 3 [Hz]	15.1	15.90	-5.30%	2^{nd} Bending-Flapping
Mode 4 [Hz]	17.4	19.01	-9.26%	Lead-Lag
Mode 5 [Hz]	24.4	27.39	-12.25%	1^{st} Torsion

7

Conclusions and Recommendations

This chapter provides a conclusion on the design, manufacturing, and testing processes of a highly flexible wing featuring a Flared Folding Wingtip (FFWT) with ailerons on both the fixed wing and the wingtip. Section Section 7.1 presents the key conclusions drawn from the obtained results, while Section 7.2 provides recommendations for conducting similar design and analysis procedures and offers recommendations for future research.

7.1. Conclusions

A review of the state of the art on FFWT reveals significant interest in the effect of control surfaces on both load alleviation performance and the handling qualities of FFWT implementations in highly flexible wings. To contribute to this research, a new aeroelastic wind tunnel demonstrator featuring an active FFWT and trailing-edge control surfaces has been developed and tested during this thesis.

This thesis presents the preliminary design, sizing, detailed design, and testing of the demonstrator using a Ground Vibration Test (GVT). In the preliminary design phase, the design requirements, constraints, and testing conditions were defined, followed by the determination of planform dimensions and the creation of a preliminary CAD model.

The sizing of the demonstrator involved three aspects: aileron sizing, servo actuator sizing for both the ailerons and hinge mechanism, and wing spar sizing. The inboard aileron is designed to achieve similar roll performance as that of a CS-25 certified aircraft. Its effectiveness is evaluated by computing the hypothetical damped roll rate, incorporating spanwise lift distribution corrections for boundary layer and separation effects. These aerodynamic corrections significantly reduce the predicted roll rate compared to a linear analysis. Additionally, increasing the angle of attack and reducing velocity both decrease the damped roll rate. To ensure effectiveness in worst-case conditions, the span of the inboard aileron was set to 70% of the trailing edge with a aileron hinge line at 75% of the chord length.

The outboard aileron was sized to ensure sufficient effectiveness to return the free wingtip to the neutral position under all operating conditions. A corrected linear lift distribution confirms that at a 5° angle of attack, the outboard aileron can provide the minimum required effectiveness to achieve this, though only marginally. Further analysis indicates that increasing the aileron chord has minimal impact on effectiveness due to the corresponding reduction in span, resulting in an outboard aileron span covering 90% of the trailing edge at the wingtip, with the outboard aileron hinge line positioned at 75% of the chord length. Although results indicate that the outboard aileron generates only a slight wingtip-down moment, the conservative nature of the analysis (neglecting wingtip weight) supports confidence that it can return the wingtip to a neutral position under all testing conditions.

Two factors were considered in sizing the aileron actuation servo actuators: required rotational speed and torque. To account for future control applications, the bandwidth of the aileron servo actuator must cover a frequency range up to the frequency of the second bending mode of the wing. Additionally, it must provide sufficient torque for operation under all testing conditions.

The hinge mechanism servo actuator is sized to provide sufficient torque to lock the hinge under all testing conditions. Based on the resultant force on the locking pin and selecting an eccentric circle to transfer the load to the servo actuator, a hinge mechanism servo actuator is selected.

The wing spar is designed as an aluminium plate running through the center of the wing, aiming to demonstrate flutter at the top of the velocity range while maintaining a highly flexible structure. However, the results revealed a conflict between these objectives. To achieve a sufficient testing range without flutter, the flutter requirement became the primary driver of the wing spar design.

Finally, the objective of this thesis included the validation of the Finite Element Method (FEM) model using Ground Vibration Testing (GVT). The FEM modal analysis of the free hinge condition showed good agreement with the GVT results, confirming that the structural model accurately represents the physical demonstrator. However, the FEM analysis significantly overestimated the eigenfrequencies under locked hinge conditions, indicating that the rigid hinge assumption could be invalid. Reducing the hinge stiffness could lower the eigenfrequencies, potentially improving the correlation between the FEM analysis and the GVT results. Additionally, elastic deformations were observed in the 3D-printed parts as the hinge servo actuator locked the hinge, further suggesting that the rigid hinge assumption is not appropriate.

7.2. RECOMMENDATIONS AND FUTURE WORK

Based on the findings and experiences from this thesis, recommendations for a similar project (Section 7.2.1) and suggestions for future work (Section 7.2.2) are provided.

7.2.1. RECOMMENDATIONS

The first recommendation concerns the aerodynamic analysis used for aileron sizing. Since the methodology described in this thesis, combining 2D and 3D effects, has not been applied elsewhere, introducing a validation method would increase confidence in the results and potentially allow for a less conservative design. A possible validation method could involve comparing the results of modeling a similar scale RC plane with available experimental data and assessing the accuracy of the aerodynamic analysis.

After sizing the wing spar, a conflict arose between the requirements for flutter speed and wingtip deflection. Since the 3D-printed components contribute minimally to the overall stiffness compared to the aluminum plate, reducing their weight could improve wingtip deflection while still meeting the flutter speed requirement.

Alternatively, changing the test setup could be a solution to achieve a larger wingtip deflection. This could include testing at a higher angle of attack, testing at a negative angle of attack to leverage weight in assisting wingtip deflection, or conducting tests with the demonstrator in a vertical orientation.

Additionally, a revised sizing of the wing spar could be considered. Instead of increasing the aluminum plate thickness, alternative methods to enhance stiffness could be explored. For instance, incorporating a hollow rib structure would allow for the inclusion of a thin aluminum plate with stringers, which could reduce the weight of the wing spar while maintaining its stiffness. This approach could increase wingtip deflection while still meeting the flutter speed requirement.

7.2.2. FUTURE WORK

Several suggestions for future work are presented for the near future. First, the current structural model, excluding the ailerons and the Oracover, should be updated to more accurately predict the GVT results presented in this thesis. Second, the assembly should be finalized, followed by a second GVT and an update to the model.

The comparison between the GVT results in the locked and free hinge conditions suggests that the rigid hinge assumption is not valid in the locked hinge condition. In future work, the physical demonstrator can be used to assess the stiffness of the hinge mechanism and update the FEM model using The Modal Assurance Criterion (MAC) to compare the predicted mode shapes to experimental results.

The above suggestions for future work focus on improving the FEM model. Additionally, a wind tunnel campaign will be used to validate the aileron and servo actuator sizing procedure. The campaign can also provide measurements on the initial behavior of the demonstrator in the wind tunnel.

Nonlinear methods should be applied to better predict the aeroelastic behavior of the demonstrator, with the wind tunnel campaign serving as a validation.

Finally, a control strategy for both the ailerons and the hinge mechanism should be developed to test the

Gust Load Alleviation (GLA) capabilities of the demonstrator. The ailerons incorporated in this design allow for comparison of the GLA capabilities of the FFWT with a fixed hinge condition using only ailerons. This can provide valuable insights into the effectiveness of the FFWT as a GLA device.

From a future perspective, this thesis demonstrates that accurately modeling the locked hinge condition is essential for creating a representative structural model. The effect of the flexible hinge was less pronounced in the previously designed FFWT demonstrator, on which the current demonstrator is based. Given that the demonstrator is approximately twice the size of the previous design, scaling could be a significant factor in modeling the hinge stiffness. For future large-scale implementations of Flared Folding Wingtips, precise modeling of the hinge stiffness will likely be critical for accurately predicting the wing's aeroelastic behavior.

A

Demonstrator Details

In this appendix, pictures of additional details of the demonstrator are presented.
In Figure A.1, a rear view of the connection between the main wing and the wingtip is shown. In order to hit the wing at the same location as accurately as possible during the GVT, a green cross was put on near the hinge.

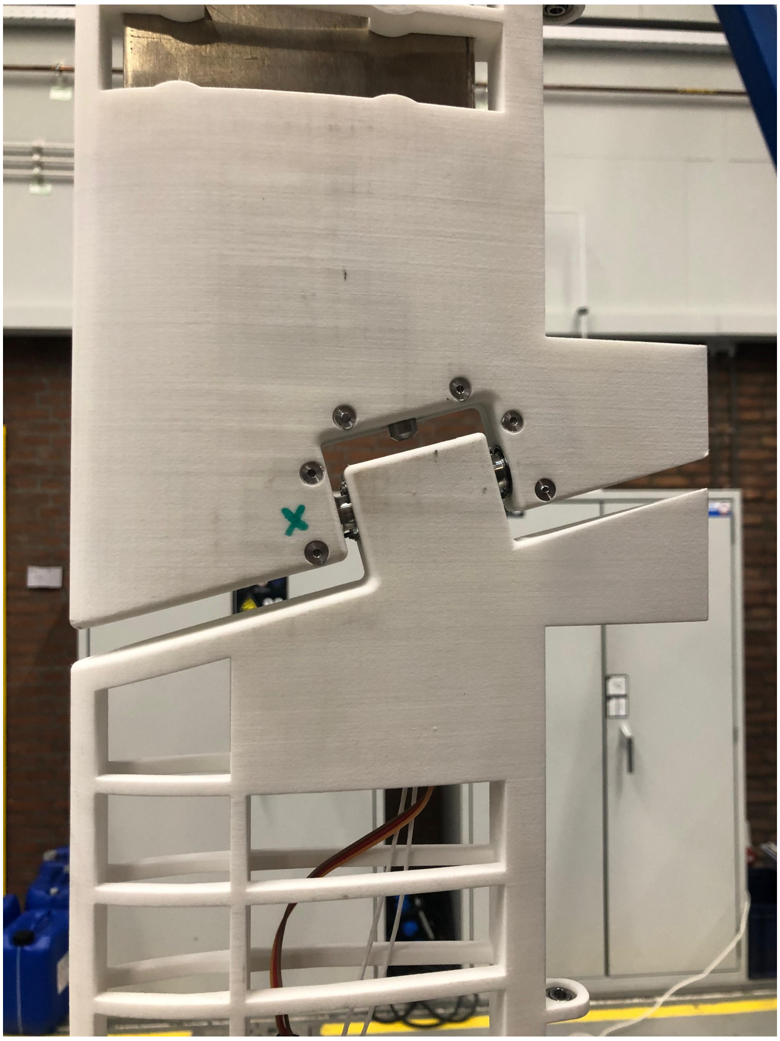

Figure A.1: Rear view of main wing - wingtip connection

Figure A.2 presents a bottom view of the demonstrator in the GVT configuration. At the top of the image, a wooden adapter plate can be seen, connecting the root of the demonstrator to the steel structure around it.

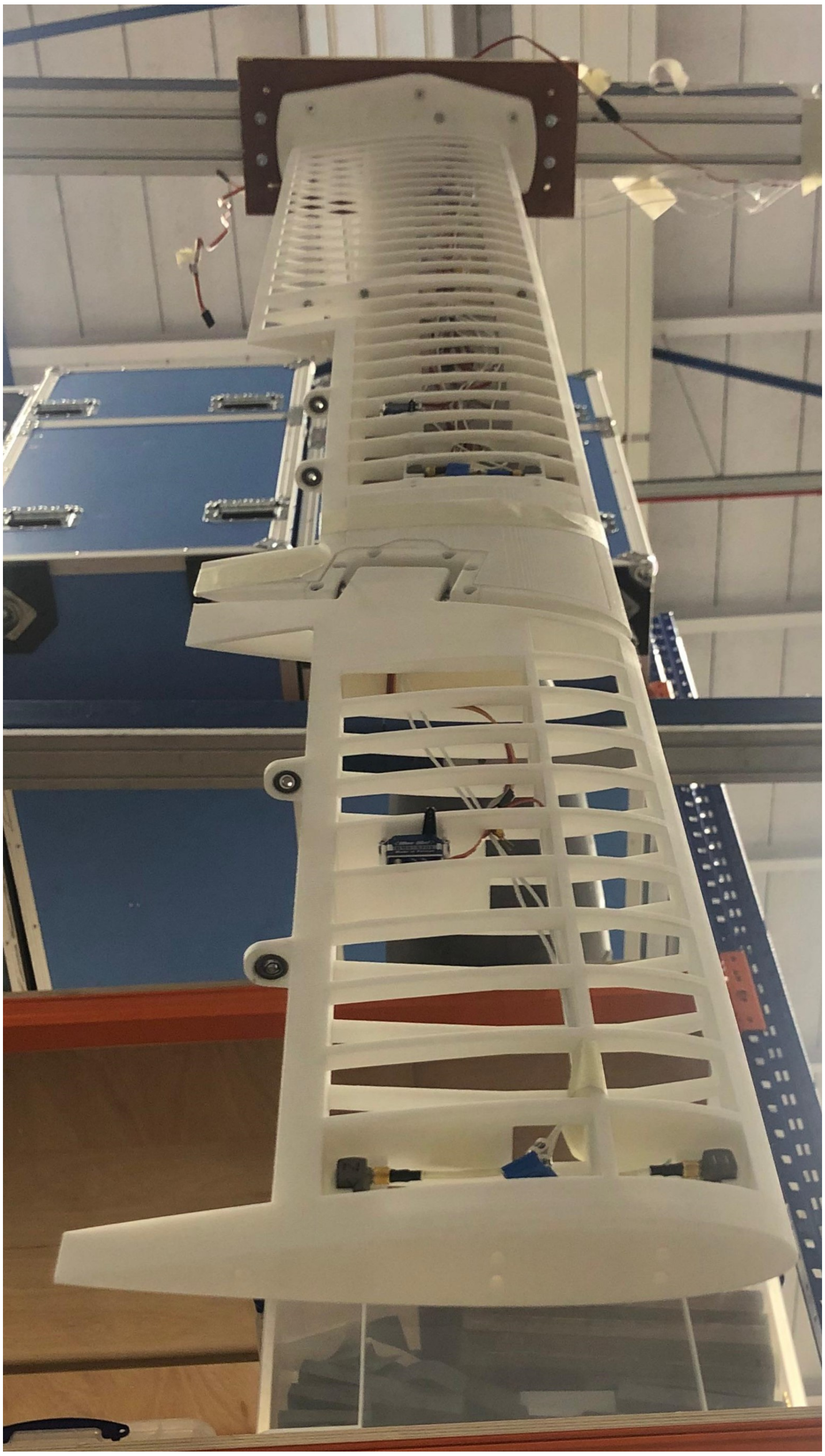

Figure A.2: Bottom view of wing in GVT configuration

In Figure A.3, the location of the four accelerometers inside the main wing can be seen.

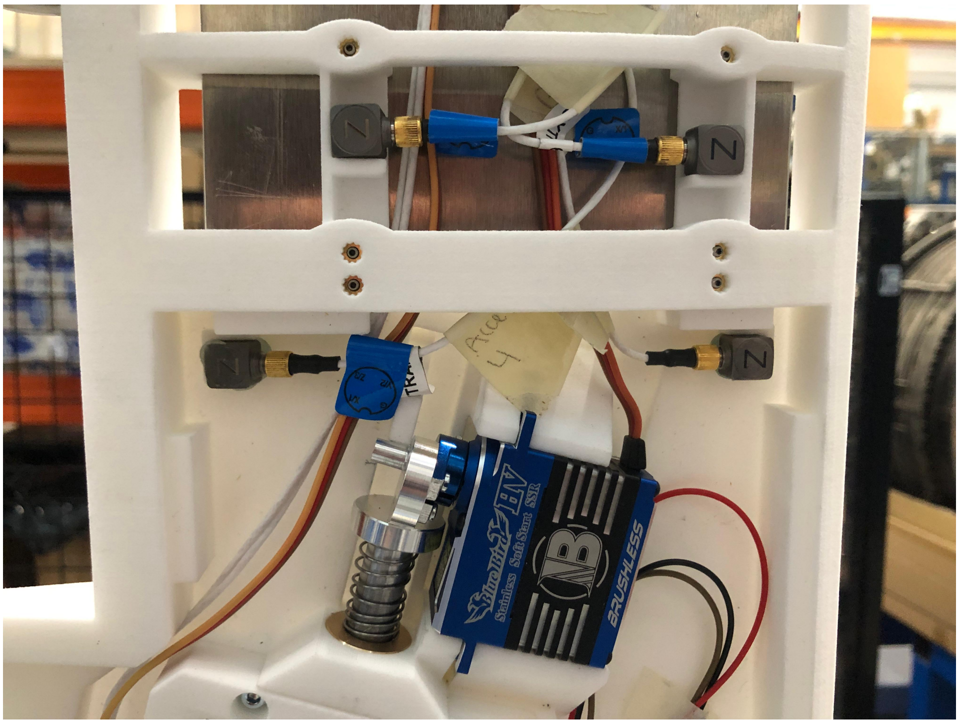

Figure A.3: Detailed picture with location of accelerometers in main wing

Figure A.4 shows the bolted connection between Main section 1 and Main section 2, together with the insert screws used to fasten the wing spar.

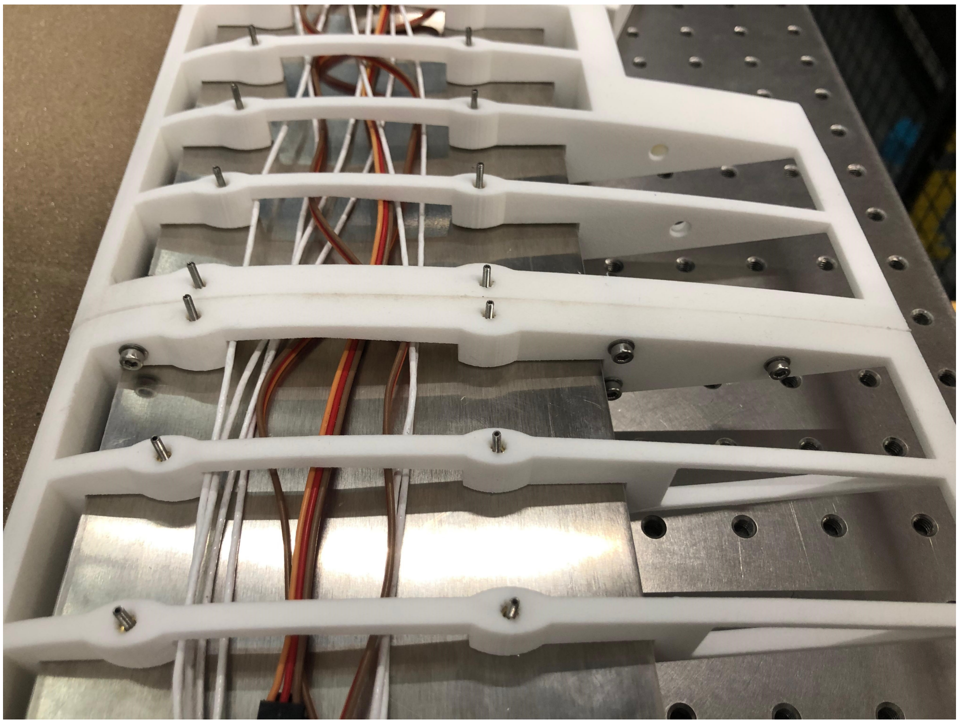

Figure A.4: Detailed view of Main section 1 - Main section 2 connection and insert screws for fastening the wing spar

In Figure A.5, a side by side view of the outboard aileron servo actuator connection is presented, with and without cover. The nylon cover is used to prevent the Oracover from tearing, while allowing for a large range of motion of the servo actuator arm.

(a) Outboard aileron servo actuator connection without cover

(b) Outboard aileron servo actuator connection with cover

Figure A.5: Outboard aileron servo actuator connection with and without cover

Figure A.6 presents one of the manufactured ailerons. At the mid-span of the aileron, a metallic connector is located to connect to the push rod of the aileron servo actuator.

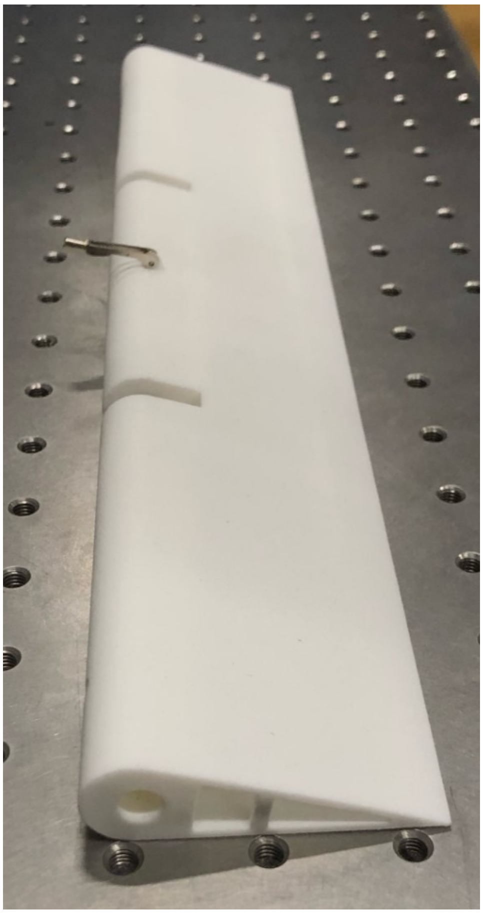

Figure A.6: Detailed view of aileron design

B

GVT RESULTS

In the graphs on the next two pages, the FRFs of both the locked hinge GVT (Figure B.1) and free hinge (Figure B.2) are displayed.

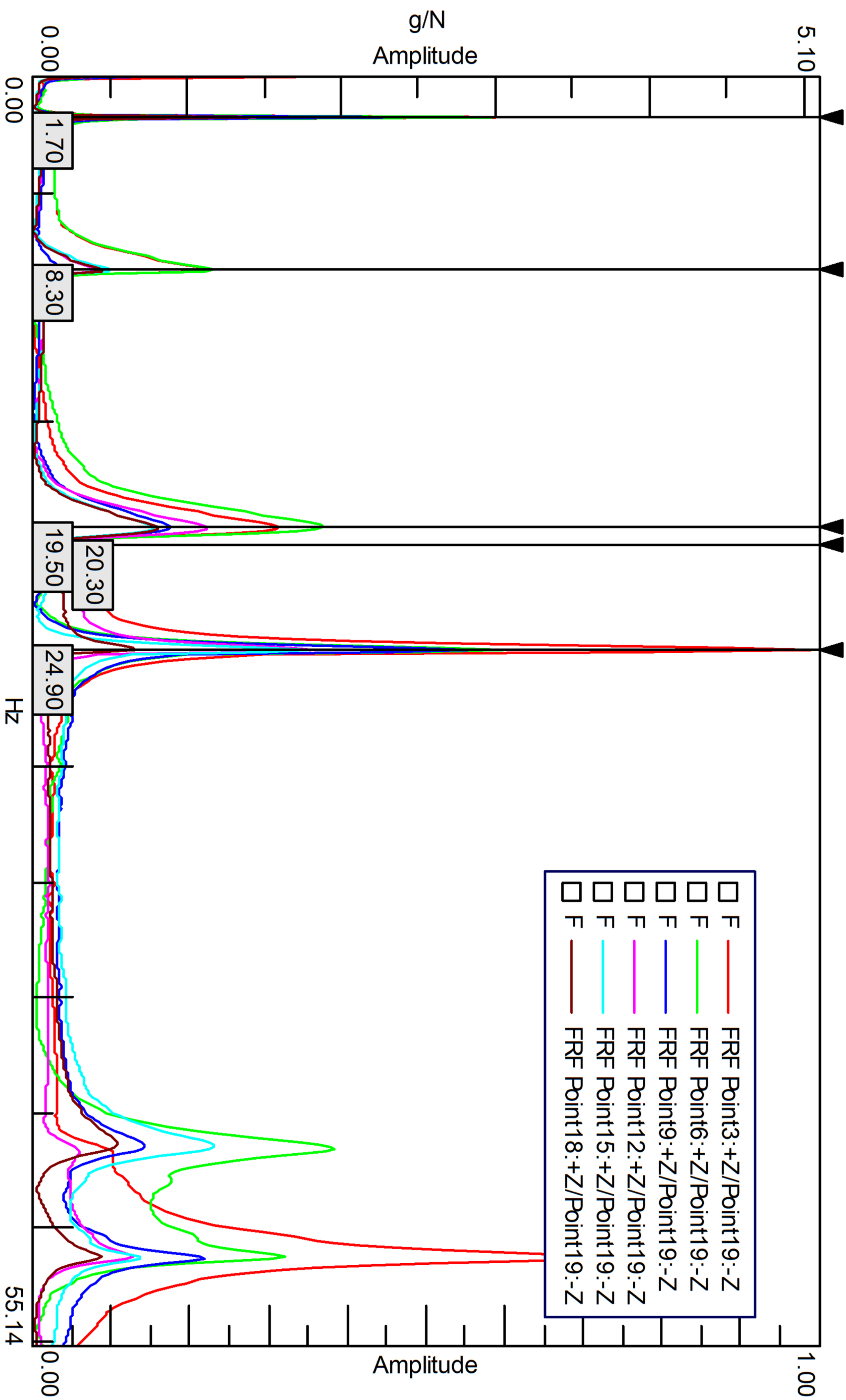

Figure B.1: FRF of locked hinge GVT with markers on the first 5 modes

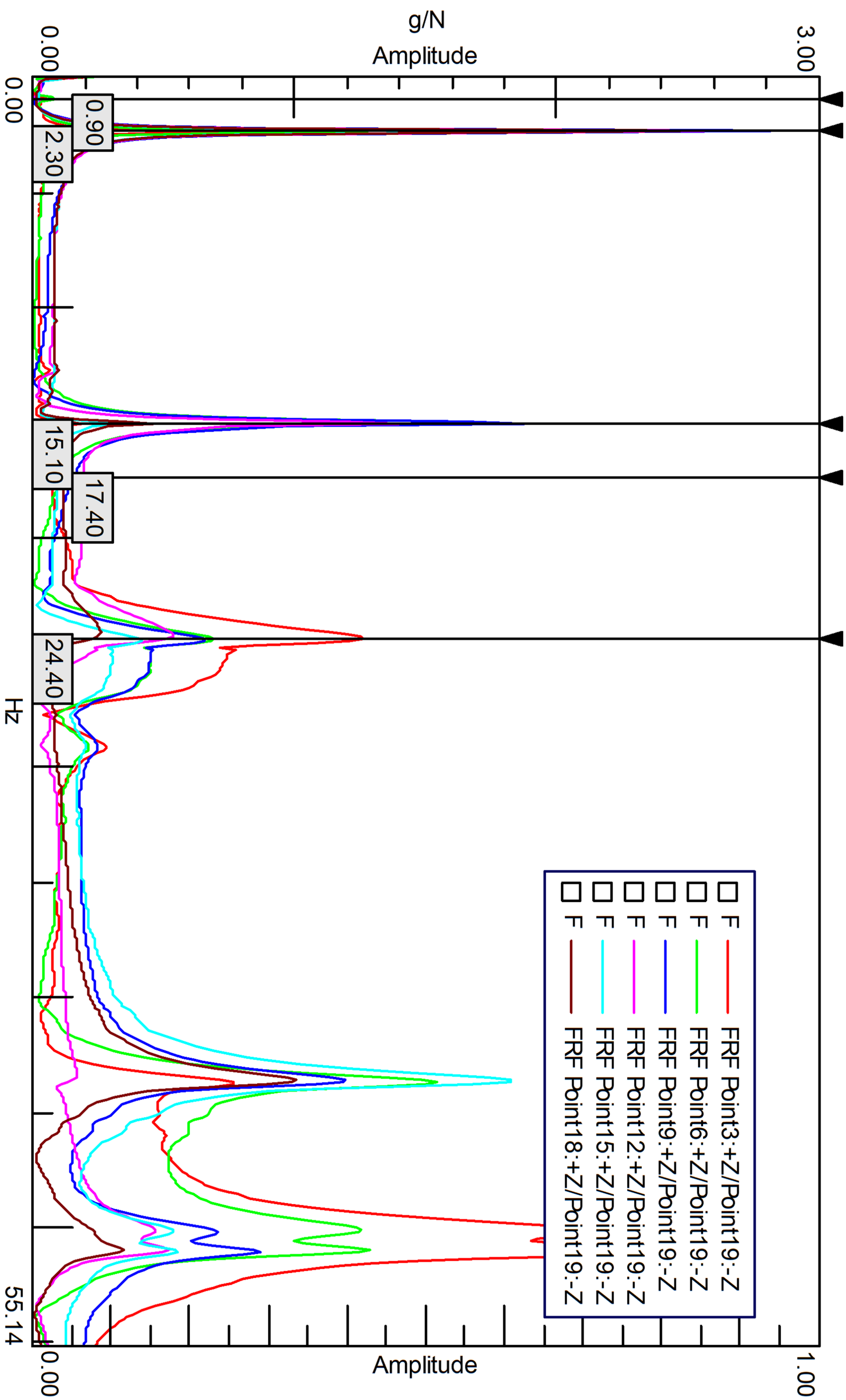

Figure B.2: FRF of free hinge GVT with markers on the first 5 modes

Bibliography

[1] C. A. Horowitz, *Paris agreement,* International Legal Materials **55** (2016), 10.1017/s0020782900004253.

[2] M. Cames, J. Graichen, A. Siemons, and V. Cook, *Emission Reduction Targets for International Aviation and Shipping* (The European Commission, 2015).

[3] F. Afonso, M. Sohst, C. M. Diogo, S. S. Rodrigues, A. Ferreira, I. Ribeiro, R. Marques, F. F. Rego, A. Sohouli, J. Portugal-Pereira, H. Policarpo, B. Soares, B. Ferreira, E. C. Fernandes, F. Lau, and A. Suleman, *Strategies towards a more sustainable aviation: A systematic review,* Progress in Aerospace Sciences **137**, 100878 (2023).

[4] F. Yin and A. G. Rao, *Off-design performance of an interstage turbine burner turbofan engine,* Journal of Engineering for Gas Turbines and Power **139** (2017), 10.1115/1.4035821.

[5] Boeing, *777x by design,* https://www.boeing.com/commercial/777x/by-design, accessed: 2025-02-19.

[6] X. Carrillo Córcoles, C. Mertens, A. Sciacchitano, B. W. van Oudheusden, R. De Breuker, and J. Sodja, *Effect of wing stiffness and folding wingtip release threshold on gust loads,* Journal of Aircraft , 1–20 (2023).

[7] A. Abbas, J. de Vicente, and E. Valero, *Aerodynamic technologies to improve aircraft performance,* Aerospace Science and Technology **28**, 100–132 (2013).

[8] E. Hirschel, K. Fujii, W. Haase, B. Leer, M. Leschziner, M. Pandolfi, A. Rizzi, B. Roux, and G. Dulikravich, *Notes on Numerical Fluid Mechanics (NNFM)* (1999).

[9] A. R. Collar, *The expanding domain of aeroelasticity,* The Journal of the Royal Aeronautical Society **50**, 613–636 (1946).

[10] N. Paletta, *Maneuver load controls, analysis and design for flexible aircraft,* (2011).

[11] Z. Wu, Y. Cao, and M. Ismail, *Gust loads on aircraft,* The Aeronautical Journal **123**, 1216–1274 (2019).

[12] Easa, *Easy access rules for large aeroplanes (cs-25) (initial issue),* .

[13] H. Khodaparast, S. Coggon, M. Friswell, and J. Cooper, *The effects of structural nonlinearity on the dynamic response to aeroelastic gust models,* (2016).

[14] A. Mancini, M. Roelofs, and R. Vos, *The effect of maneuver load alleviation strategies on aircraft performance indicators,* (American Institute of Aeronautics and Astronautics Inc, AIAA, 2019) pp. 1–17.

[15] O. Stodieck, J. E. Cooper, and P. M. Weaver, *Interpretation of bending/torsion coupling for swept, nonhomogenous wings,* Journal of Aircraft **53**, 892 (2016).

[16] H. Söker, *Loads on wind turbine blades,* (Elsevier Inc., 2013) pp. 29–58.

[17] S. Guo, J. E. D. L. Monteros, and Y. Liu, *Gust alleviation of a large aircraft with a passive twist wingtip,* Aerospace **2**, 135 (2015).

[18] S. Guo, Z. W. Jing, H. Li, W. T. Lei, and Y. Y. He, *Gust response and body freedom flutter of a flying-wing aircraft with a passive gust alleviation device,* Aerospace Science and Technology **70**, 277 (2017).

[19] Y. Li and N. Qin, *A review of flow control for gust load alleviation,* (2022).

[20] AGARD, *Special course on aerodynamic characteristics of controls,* (1983).

[21] H. Consigny, A. Gravelle, and R. Molinaro, *Aiaa-83-1809 aerodynamic characteristics of a two-dimensional moving spoiler in subsonic and transonic flow,* (1983).

[22] R. D. Breuker, M. Abdalla, and P. Marzocca, *Aeroelastic control and load alleviation using optimally distributed synthetic jet actuators,* (2007).

[23] A. Castrichini, V. H. Siddaramaiah, D. E. Calderon, J. E. Cooper, T. Wilson, and Y. Lemmens, *Preliminary investigation of use of flexible folding wing tips for static and dynamic load alleviation,* Aeronautical Journal **121**, 73 (2017).

[24] E. ALBANO and W. P. RODDEN, *A doublet-lattice method for calculating lift distributions on oscillating surfaces in subsonic flows.* AIAA Journal **7**, 279 (1969), https://doi.org/10.2514/3.5086 .

[25] A. Castrichini, V. H. Siddaramaiah, D. E. Calderon, J. E. Cooper, T. Wilson, and Y. Lemmens, *Nonlinear folding wing tips for gust loads alleviation,* (American Institute of Aeronautics and Astronautics Inc., 2016) pp. 1391–1399.

[26] A. Castrichini, J. E. Cooper, T. Wilson, A. Carrella, and Y. Lemmens, *Nonlinear negative stiffness wingtip spring device for gust loads alleviation,* (American Institute of Aeronautics and Astronautics Inc., 2017) pp. 627–641.

[27] G. Dussart, S. Yusuf, and M. Lone, *Identification of in-flight wingtip folding effects on the roll characteristics of a flexible aircraft,* Aerospace **6**, 63 (2019).

[28] R. C. Cheung, D. Rezgui, J. E. Cooper, and T. Wilson, *Testing of a hinged wingtip device for gust loads alleviation,* (American Institute of Aeronautics and Astronautics Inc., 2018) pp. 2050–2067.

[29] R. C. Cheung, D. Rezgui, J. E. Cooper, and T. Wilson, *Testing of folding wingtip for gust load alleviation of flexible high-aspect-ratio wing,* Journal of Aircraft **57**, 876 (2020).

[30] F. Healy, R. Cheung, T. Neofet, M. Lowenberg, D. Rezgui, J. Cooper, A. Castrichini, and T. Wilson, *Folding wingtips for improved roll performance,* (American Institute of Aeronautics and Astronautics Inc, AIAA, 2021) pp. 1–24.

[31] D. Sanghi, C. E. Cesnik, and C. Riso, *Roll maneuvers of very flexible aircraft with flared folding wingtips,* in *AIAA SciTech Forum and Exposition, 2023* (American Institute of Aeronautics and Astronautics Inc, AIAA, 2023).

[32] X. C. Córcoles, C. Mertens, A. Sciacchitano, B. W. van Oudheusden, R. D. Breuker, and J. Sodja, *Effect of wing stiffness and folding wingtip release threshold on gust loads,* Journal of Aircraft **60**, 1917 (2023).

[33] X. C. Córcoles, R. D. Breuker, and J. Sodja, *Nonlinear low-fidelity numerical model of the flared folding wingtip,* in *AIAA SciTech Forum and Exposition, 2023* (American Institute of Aeronautics and Astronautics Inc, AIAA, 2023).

[34] T. Wilson, J. Kirk, J. Hobday, and A. Castrichini, *Small scale flying demonstration of semi aeroelastic hinged wing tips,* (2019).

[35] Airbus, *extra performance wing demonstrator takes off,* (2023).

[36] M. Pusch, A. Knoblach, and T. Kier, *Integrated optimization of control surface layout for gust load alleviation,* CEAS Aeronautical Journal **10**, 1059 (2019).

[37] C. Mertens, J. Sodja, A. Sciacchitano, and B. W. van Oudheusden, *Experimental aeroelastic characterization of a very flexible wing in steady and unsteady inflow,* in *AIAA Science and Technology Forum and Exposition, AIAA SciTech Forum 2022* (American Institute of Aeronautics and Astronautics Inc, AIAA, 2022).

[38] M. Drela and H. Youngren, *MIT AVL User Primer*, MIT.